The First Samples from Almahata Sitta Showing Contacts Between Ureilitic and Chondritic Lithologies: Implications for the Structure and Composition of Asteroid 2008 TC_3

Cyrena Anne Goodrich[1],

Michael E. Zolensky[2], Anna Maria Fioretti[3], Muawia H. Shaddad[4],

Hilary Downes[5], Takahiro Hiroi[6], Issaku Kohl[7], Edward D. Young[7], Noriko T. Kita[8],

Victoria E. Hamilton[9], My E.I. Riebe[10,11], Henner Busemann[11],

Robert J. Macke[12], M. Fries[2], D. Kent Ross[13], Petrus Jenniskens[14]

[1]Lunar and Planetary Institute, Universities Space Research Association, 3600 Bay Area Blvd, Houston, TX 77058 USA goodrich@lpi.usra.edu

[2]Astromaterials Research and Exploration Science, NASA-Johnson Space Center Houston, TX 77058 USA

[3]CNR – Istituto di Geoscienze e Georisorse, I-35131 Padova, Italy

[4]Physics Department, University of Khartoum, Khartoum 11115 Sudan

[5]Department of Earth and Planetary Sciences, Birkbeck, University of London, Malet Street, Bloomsbury, London WC1E 7HX UK

[6]Department of Geological Sciences, Brown University, Providence, RI 02912, USA

[7]Department of Earth and Planetary Sciences, University of California at Los Angeles, 595 Charles Young Drive East, Los Angeles, CA 90095 USA

[8]Wisc-SIMS Laboratory, Department of Geoscience, University of Wisconsin-Madison, 1215 West Dayton Street, Madison, WI 53706 USA

[9]Department of Space Studies, Southwest Research Institute, 1050 Walnut St., Suite 300, Boulder Colorado 80302 USA

[10]Department of Terrestrial Magnetism, Carnegie Institution for Science, 5241 Broad Branch Rd NW, Washington, DC 20015, USA

[11]Institute for Geochemistry and Petrology, ETH Zürich, Clausiusstrasse 25, CH-8092 Zürich, Switzerland

[12]Specola Vaticana, V-00120 Vatican City State

[13]Jacobs-JETS, University of Texas at El Paso, at NASA-JSC, Houston, TX 77058 USA

[14]SETI Institute, 189 Bernardo Ave, Mountain View CA 94043 USA

ABSTRACT

Almahata Sitta (AhS), an anomalous polymict ureilite, is the first meteorite observed to originate from a spectrally classified asteroid (2008 TC_3). However, correlating properties of the meteorite with those of the asteroid is not straightforward because the AhS stones are diverse types. Of those studied prior to this work, 70-80% are ureilites (achondrites) and 20-30% are various types of chondrites. Asteroid 2008 TC_3 was a heterogeneous breccia that disintegrated in the atmosphere, with its clasts landing on Earth as individual stones and most of its mass lost. We describe AhS 91A and AhS 671, which are the first AhS stones to show contacts between ureilitic and chondritic materials and provide direct information about the structure and composition of asteroid 2008 TC_3.

AhS 91A and AhS 671 are friable breccias, consisting of a C1 lithology that encloses rounded to angular clasts (<10 μm to 3 mm) of olivine, pyroxenes, plagioclase, graphite, and metal-sulfide, as well as chondrules (~130-600 μm) and chondrule fragments. The C1 material consists of fine-grained phyllosilicates (serpentine and saponite) and amorphous material, magnetite, breunnerite, dolomite, fayalitic olivine (Fo 28-42), an unidentified Ca-rich silicate phase, Fe,Ni sulfides, and minor Ca-phosphate and ilmenite. It has similarities to CI1 but shows evidence of heterogeneous thermal metamorphism. Its bulk oxygen isotope composition ($\delta^{18}O$ = 13.53‰, $\delta^{17}O$ = 8.93‰) is unlike that of any known chondrite, but similar to compositions of several CC-like clasts in typical polymict ureilites. Its Cr isotope composition is unlike that of any known meteorite. The enclosed clasts and chondrules do not belong to the C1 lithology. The olivine (Fo 75-88), pyroxenes (pigeonite of Wo ~10 and orthopyroxene of Wo ~4.6), plagioclase, graphite, and some metal-sulfide are ureilitic, based on mineral compositions, textures, and oxygen isotope compositions, and represent at least six distinct ureilitic lithologies. The chondrules are probably derived from type 3 OC and/or CC, based on mineral and oxygen isotope compositions. Some of the metal-sulfide clasts are derived from EC.

AhS 91A and AhS 671 are plausible representatives of the bulk of the asteroid that was lost. Reflectance spectra of AhS 91A are dark (reflectance ~0.04-0.05) and relatively featureless in VNIR, and have an ~2.7 μm absorption band due to OH^- in phyllosilicates. Spectral modeling, using mixtures of laboratory VNIR reflectance spectra of AhS stones to fit the F-type spectrum of the asteroid, suggests that 2008 TC_3 consisted mainly of ureilitic and AhS 91A-like materials, with as much as 40-70% of the latter, and <10% of OC, EC and other meteorite types. The bulk density of AhS 91A (2.35 ± 0.05 g/cm^3) is lower than bulk densities of other AhS stones, and closer to estimates for the asteroid (~1.7-2.2 g/cm^3). Its porosity (36%) is near the low end of estimates for the asteroid (33-50%), suggesting significant macroporosity.

The textures of AhS 91A and AhS 671 (finely comminuted clasts of disparate materials intimately mixed) support formation of 2008 TC_3 in a regolith environment. AhS 91A and AhS 671 could represent a volume of regolith formed when a CC-like body impacted into already well-gardened ureilitic + impactor-derived debris. AhS 91A bulk samples do not show a solar wind (SW) component, so they represent sub-surface layers. AhS 91A has a lower cosmic ray exposure (CRE) age (~5-9 Ma) than previously studied AhS stones (11-22 Ma). The spread in CRE ages argues for irradiation in a regolith environment. AhS 91A and AhS 671 show that ureilitic asteroids could have detectable ~2.7 μm absorption bands.

INTRODUCTION

Asteroid 2008 TC_3 was the first near-Earth object (NEO) to be detected before it hit the Earth (Kowalski et al. 2008; Yeomans 2008; Chesley et al. 2008). It was discovered on October 6 2008, and then tracked and studied for ~20 hours before it impacted in northern Sudan (Jenniskens et al. 2009; Scheirich et al. 2010; Kozubal et al. 2011). Organized search campaigns in the predicted fall area resulted in recovery of more than 700 stones, ~0.2-400 g in mass, which were collectively named the Almahata Sitta (AhS) meteorite (Shaddad et al. 2010). Almahata Sitta is the first meteorite observed to originate from a spectrally classified asteroid, and provides an unprecedented opportunity to correlate spectral, compositional, and physical properties of a meteorite with those of the asteroid from which it was derived.

Almahata Sitta is also remarkable because, unlike any previous known meteorite fall, its stones are not all the same meteorite type. The main collection of AhS is curated at the University of Khartoum (UoK), documented with find coordinates for each stone in the strewn field (Fig. 1). Eighty-five of these stones have been studied so far, as well as ~100 AhS stones from unknown find locations that were distributed by private meteorite dealers. Based on these studies, approximately 70-80% of the stones are ureilites (carbon-rich ultramafic achondrites that represent the residual mantle of a differentiated asteroid), whereas 20-30% are various types of chondrites (Zolensky et al. 2010; Horstmann and Bischoff 2014; Bischoff et al. 2015a, 2016; Fioretti et al. 2017; Goodrich et al. 2018). The ureilites span the entire range of petrologic types seen among main group ureilites, and the chondrites include all major classes (enstatite, ordinary, carbonaceous, and Rumuruti-type chondrites) and numerous groups and subgroups (Horstmann and Bischoff 2014; Goodrich et al. 2015a). AhS is classified as an anomalous polymict ureilite (Jenniskens et al. 2009). This classification implies that it is analogous (though not necessarily identical) to typical polymict ureilites, which are breccias dominated by ureilitic material but also containing chondritic and other xenolithic clasts (Prinz et al. 1986, 1987; Goodrich et al. 2004; Downes et al. 2008). However, unlike typical polymict ureilites, AhS has been disaggregated. It can be inferred that 2008 TC_3 was a heterogeneous asteroidal breccia in which the clasts were so loosely bound that they separated in the atmosphere and landed on Earth as individual stones.

Pre-impact observations of 2008 TC_3 support this inference. The average diameter of the asteroid was ~4 m, based on the light curve and F-type reflectance spectrum (Jenniskens et al. 2009; Scheirich et al. 2010). Its bulk density was ~1.7 g/cm^3, based on its size and abundances of

cosmogenic nuclides in some of the stones (Welten et al. 2010). This value is significantly lower than densities of the studied stones, particularly the typical ureilites (~3.3 g/cm^3), which implies ~25-50% porosity in the asteroid (Jenniskens et al. 2009; Welten et al. 2010). This suggests that the asteroid was loosely consolidated, which explains why it shattered at such a high altitude (Borovička and Charvát 2009; Jenniskens et al. 2009; Shaddad et al. 2010; Popova et al. 2011). These data also imply that most of the mass of 2008 TC_3 was lost in the atmosphere, probably as dust. The total mass of fallen material was estimated to be ~40 kg (Shaddad et al. 2010), representing ≤0.1% of the estimated mass of the asteroid. Thus, the asteroid must have consisted of >99% loosely consolidated, porous material, with only the small fraction of more coherent clasts surviving as meteorite fragments (Jenniskens et al. 2009; Goodrich et al. 2015a). Nevertheless, the reflectance spectrum of the asteroid provides information on the composition and grain size of the lost material.

The reflectance spectrum of 2008 TC_3 was measured in the 0.5-1 μm range (Jenniskens et al. 2009, 2010), and most closely matches F-type asteroids in the Tholen taxonomy (Tholen and Barucci 1989). The average F-type albedo of 0.046 (Mainzer et al. 2011) is consistent with independent estimates of the asteroid's size (Jenniskens et al. 2009). F-type asteroids belong to the C complex of dark asteroids commonly identified with carbonaceous chondrites (Tholen and Barucci 1989; DeMeo et al. 2009, 2015). If Almahata Sitta had not been recovered, 2008 TC_3 would have been assumed to be a carbonaceous chondrite. The recovery of AhS provided irrefutable evidence that not all dark asteroids are primitive, making studies of the AhS stones important for distinguishing differentiated dark asteroids from primitive dark asteroids.

However, determining the structure and composition of asteroid 2008 TC_3 has been hindered so far because none of the studied AhS stones showed contacts between ureilitic and chondritic lithologies. Here we describe the first AhS stones that do. AhS 91/91A and AhS 671 are breccias consisting of C1 carbonaceous chondrite, ureilite, ordinary chondrite, and enstatite chondrite components. We report mineralogy and petrology, oxygen isotope compositions, density and porosity, reflectance spectra from visible through thermal infrared (VNIR to TIR) wavelengths, and noble gas abundances for these two AhS stones. We also measured chromium isotope compositions, which are reported elsewhere (Sanborn et al. 2017; Qin et al. 2018). We discuss implications for the structure, composition, and formation of asteroid 2008 TC_3, and for remote sensing of ureilitic asteroids.

SAMPLES AND ANALYTICAL METHODS

UoK stones 91 and 91A (hereafter referred to collectively as 91A) were recovered together near the central part of the AhS strewn field (Fig. 1). They were suspected to be paired (Shaddad et al. 2010) and this is confirmed by the results of our studies. The two stones originally had a combined mass of 8.57 g, but they are extremely friable and have been progressively crumbling into smaller fragments (e.g., Fig. 2). AhS 671 (original mass 11.85 g) was recovered ~1400 m from AhS 91A (Fig. 1) and is also very friable. We were allocated ~1.5 g of each, entirely as small fragments (most <100 mg each). We used a variety of analytical techniques to study these fragments (Supplement 1) including: X-ray Computed Tomography (XRCT or CT scans); field-emission scanning electron microscopy (FE-SEM); field emission electron microprobe analyses (FE-EMPA); focused ion beam (FIB) milling and transmission electron microscopy (TEM); Raman spectroscopy; visible-to-near-infrared (VNIR) and Fourier transform infrared (FTIR) reflectance spectroscopy; microscopic FTIR (μ-FTIR) reflectance spectroscopy; noble gas analysis; bulk and in-situ (SIMS) oxygen isotope analyses; chromium isotope analysis (reported elsewhere); and determination of bulk density, grain density, and porosity. All analytical methods are described in Supplement 2.

RESULTS

Petrography and Mineral Compositions

We studied polished sections of 20 fragments of AhS 91A and 22 fragments of AhS 671, with exposed areas ranging from ~0.05 to 10 mm^2. These two AhS breccias are very similar and consist of a hydrous carbonaceous chondrite-like lithology (C1) enclosing clasts of olivine, pyroxene, plagioclase, and graphite (ranging from <10 μm to ~3 mm in size), as well as chondrules (~130-600 μm in diameter) and metal-sulfide grains (up to ~1.3 mm in size). Most of the fragments studied do not show this entire assemblage. Individual fragments consist of either: 1) C1 matrix material; 2) olivine, pyroxene, plagioclase, or metal grains; 3) C1 material containing or in contact with clasts of olivine, pyroxene, plagioclase, and/or metal; or 4) C1 material containing chondrules, as well as clasts of olivine, pyroxene, plagioclase and metal.

C1 Material

C1 material is the most abundant component (Fig. 3-11). It consists mostly of fine-grained phyllosilicates, with varying abundances of a Ca-rich silicate phase, carbonates, magnetite, fayalitic olivine, and Fe,Ni sulfides, plus minor Ca-phosphate and ilmenite. Its texture shows a variety of rounded clasts in a fine-grained matrix, with the clasts differing in relative proportions of phases, as well as how distinct they are from the matrix. One common type of clast (e.g., areas 1 and 3 in Fig. 3a,b) is Ca-rich. It consists of phyllosilicates plus a high abundance of a patchy to fibrous Ca-rich silicate phase, as well as clusters of magnetite grains (Fig. 4). Another type of clast (e.g., area 4 in Fig. 3a,b) consists almost entirely of serpentine intergrown with one or more poorly-crystalline phyllosilicates, plus a few larger pyrrhotite grains (Fig. 5). The matrix of the C1 lithology is a fine-grained mixture of all observed phases in varying proportions (e.g., Fig. 3c,d).

Broad beam electron microprobe (EMP) analyses suggest that the most abundant phyllosilicates in both clasts and matrix are a mixture of serpentine with varying Mg# (=molar Mg/[Mg+Fe]) and saponite (Fig. 6; Table 1). FIB/TEM observations of area 1, a Ca-rich clast, revealed that most silicates are poorly crystalline (Fig. 7,8). Local regions of flaky phyllosilicates (Fig. 7, 8a,b) grade into moderately well crystalline spongy phyllosilicates, and then into poorly crystalline spongy material (Fig. 7, 8c,d). These morphologies are very similar to those commonly observed in CI chondrites (Barber 1981, 1985; Zolensky et al. 1993). Flaky phyllosilicates frequently surround Fe-Ni sulfide grains (Fig. 7). Phyllosilicate packets are generally <100 nm across and are not well crystalline. Interlayer lattice spacings vary from 0.95 to 1.3 nm. This information and EDX spectra indicate a mixture of at least two phyllosilicate phases and Fe-Ni sulfides. The interlayer lattice fringes and approximate composition of one of these phyllosilicates is consistent with a smectite, perhaps saponite, with lattice spacings from 1.1 to 1.3 nm. Approximately 1 nm d-spacings are common in smectite (saponite) in Orgueil (Klimentidis and MacKinnon 1986). Naturally-dehydrated meteoritic smectites exhibit a range of interlayer spacings from 1.1 to 1.4 nm (e.g. Nakamura 2005; Tonui et al. 2014), as observed in AhS 91A.

The Ca-rich silicate phase or assemblage (~13-15 wt.% CaO; Table 1) in area 1 and similar clasts has not yet been identified. Based on EMP totals of ~94-97%, this phase contains less OH than serpentine or a smectite (such as saponite), for which totals typically range from 87-89%.

FIB/TEM analyses (Fig. 4d) showed this "phase" to consist of Ca-rich, poorly crystalline material with occasional flakes of a layered phase with a basal spacing of 0.95-0.96 nm, which we verified by recalibrating our scale bar for TEM images. This layer lattice value would be correct for completely dehydrated smectites. However the Ca content of this "phase" is far too high to be only a smectite. Therefore, we hypothesize that this Ca-rich material is an assemblage of two phases. Elsewhere in AhS 91A we observe phyllosilicates in association with Ca-bearing carbonates. After phyllosilicates begin to dehydrate, Ca carbonates calcine to CaO plus CO_2 (Rodriguez-Navarro et al. 2009). In permeable rocks (e.g., at or near an asteroid's surface) the CO_2 would escape, and at this low CO_2 pressure calcination occurs at temperatures as low as 450 °C (Grasa et al. 2014), a temperature consistent with dehydration of smectites (Nakamura 2005; Tonui et al. 2014). Thus, the Ca-rich "phase" may be a mixture of poorly-crystalline CaO and dehydrated smectite. This posibility will be further investigated with other techniques.

FIB/TEM observations of area 4 (Fig. 5) showed that the dominant fibrous phase has a basal lattice spacing of 0.770 to 0.772 nm consistent with Mg-rich serpentines (Mg# ~0.9 based on EMPA; Fig. 6). The serpentine is surrounded by poorly crystalline spongy phyllosilicates. Chrysotile serpentine is occasionally observed here with characteristic cylindrical morphology, although these sometimes do not show well-defined lattice fringes (Fig. 5d), a characteristic of heating to temperatures <300ºC (Nakamura 2005; Tonui et al. 2014).

Breunnerite is the most abundant carbonate in the C1 lithology (Fig. 9a), occurring as rounded grains, ~70-400 μm in size, with average composition $Mg_{0.64}Fe_{0.26}Mn_{0.09}Ca_{0.01}CO_3$ in AhS 91A and $Mg_{0.67}Fe_{0.24}Mn_{0.07}Ca_{0.02}CO_3$ in AhS 671 (Table 2). Dolomite grains of similar size were observed in AhS 91A (Fig. 9b), with average composition $Mg_{0.43}Fe_{0.06}Mn_{0.03}Ca_{0.48}CO_3$ (Table 2). Both types of carbonate have corroded outer rims with magnesite-enriched breunnerite compositions (e.g., $Mg_{0.88}Fe_{0.11}Mn_{0.01}Ca_{0.00}CO_3$). Breunnerite similar in composition to the rims also occurs as 10-20 μm-sized irregular patches in the matrix (Fig. 3c,d; Table 2).

Magnetite occurs pervasively in the matrix as clusters of anhedral to subhedral grains with irregular rims of porous, fayalitic olivine (Fig. 10a,c,d), as clusters of radially oriented grains (Fig. 4a-c), and also as subhedral grains embedded in pyrrhotite (Fig. 10b). Abundances of minor elements in the magnetite are extremely low (Fig. 10e,f; Table 3), similar to magnetite in CI and CR chondrites (Folinsbee et al. 1967; Böstrom and Fredriksson 1966; Löhn and El Goresy 1992; Harju et al. 2014), as well as CC-like clasts in typical polymict ureilites. Fine-grained sulfides

200 are dispersed abundantly throughout the matrix. Some matrix areas have concentrations of
201 fayalitic olivine (Fo 28-42), which occurs as porous tabular crystals with numerous small
202 inclusions of other phases (Fig. 11). Such areas appear be more abundant in AhS 671 than AhS
203 91A.
204
205 *Clasts of Olivine, Pyroxene, Plagioclase, Graphite and Metal*
206 Clasts of olivine, pigeonite, orthopyroxene, plagioclase and graphite (in order of decreasing
207 abundance) are embedded in the C1 matrix (Fig. 12-13). They are rounded to angular and up to
208 ~3 mm in size. They are completely enclosed within the C1 material and show no evidence of
209 reaction with their surroundings (Fig. 12, 13). In a few occurrences, they are concentrated along
210 cracks or in brecciated zones. Some of the olivine clasts appear to be polymineralic and some
211 have small inclusions of graphite. Otherwise, no compound clasts were observed.
212 The olivine clasts are homogeneous except for reduced zones (Mg-enriched olivine
213 containing numerous tiny grains of metal) along grain boundaries and around inclusions of
214 graphite (Fig. 12a,c). Core compositions range from Fo 75 to Fo 87.5 among clasts (Table 4). At
215 least six distinct olivine core compositions were observed. Reduced zones have higher Fo than
216 cores, up to ~99. Several olivine clasts of Fo ~78-79 contain micron-sized symplectic lamellae of
217 chromite + pyroxene (Fig. 12e). Figure 14 shows plots of molar Fe/Mg vs. molar Fe/Mn and
218 wt.% Cr_2O_3 vs. CaO for all olivine clasts (including reduced zones), compared with olivine in
219 other types of meteorites. The clasts plot along the Fe/Mg vs. Fe/Mn trend defined by the
220 olivine+low-Ca pyroxene main group ureilites (Fig. 14a), and encompass most of the ureilite
221 range. They have high CaO (~0.25-0.50 wt.%) and Cr_2O_3 (~0.45-1.0 wt.%) contents, which are
222 also consistent with those in ureilite olivine (Fig. 14b). These features distinguish the olivine
223 clasts in AhS 91A and AhS 671 from olivines in C1 and C2 carbonaceous chondrites, type 4-6
224 ordinary and enstatite chondrites (Steele 1990; Leshin et al. 1997; Frank et al. 2014; Brearley
225 and Jones 1998), and all major groups of olivine-rich achondrites other than ureilites.
226 The pyroxene clasts in AhS 91A and AhS 671 (Table 4) include pigeonite of Wo ~7-10 (Mg#
227 78-88), orthopyroxene of ~Wo 4.5 (Mg# 88-89), and one clast of orthopyroxene of Wo 0.8 (Mg#
228 99.5) (note that we refer to pyroxenes with Wo <5 as orthopyroxene). Each clast is
229 homogeneous, except that some pigeonites have irregularly-shaped, porous, Mg-rich patches
230 containing blebs of metal (Fig. 13c). At least five distinct pigeonite compositions were observed

(Table 4). Major and minor (Al_2O_3 and Cr_2O_3) element compositions of the pyroxene clasts are compared with compositions of low-Ca pyroxenes in other types of meteorites in Figure 15. The pigeonite and Wo ~4.5 orthopyroxene clasts are consistent with compositions of low-Ca pyroxenes in main group and typical polymict ureilites, and are distinguished from those of low-Ca pyroxenes in most other groups of chondrites and achondrites. The one orthopyroxene clast of Wo ~0.8 has major and minor element composition consistent with orthopyroxenes in several types of chondrites (Fig. 15).

Three plagioclase clasts were observed (Fig. 13e, f). Two are Na-rich (An ~3-5, Or 3-4). The third is more calcic, with An ~35 (Table 4, columns 16-18). The analyses are stoichiometric (Table 4), suggesting that they are or once were crystalline. Graphite (identified by Raman spectroscopy, Supplement 3) occurs as inclusions in olivine clasts, and as isolated masses up to ~300 μm in size in the C1 matrix (Fig. 13d). Several of the isolated graphite masses were found to contain minor diamond (Supplement 3).

Three types of metal grains (or assemblages) were observed. The first type consists of kamacite containing significant P, Cr, and Si (Table 5), and is sometimes associated with Cr-bearing troilite. Metal grains of this type occur as inclusions in graphite masses (e.g. Fig. 13d). The second type consists of kamacite + taenite ± troilite (e.g., Fig. 16a), with the kamacite having very low Si, P, and Cr contents (Table 5). The third type consists of Si-rich, Cr-poor kamacite (Table 5) with abundant inclusions of enstatite and niningerite (e.g., Fig. 16c-d). One particularly large clast of this type is a 1.2 mm long lath in AhS 91A_09 (Fig. 16b). Compositions of the kamacite in the clasts are compared with compositions of kamacite in ureilites, ordinary chondrites, enstatite chondrites, and iron meteorites in Figure 17.

Chondrules

A CT scan of fragment AhS 91_01 showed that it contained spherical objects that appeared to be chondrules. The fragment was mounted in epoxy and then sectioned conservatively (near its outer surface), revealing four ~140 to 600 μm-diameter chondrules (#2-5), along with several clasts of olivine, pigeonite, orthopyroxene, and plagioclase, embedded in C1 material (Fig. 18a). The chondrules are located at the edge of the fragment in this section, without connecting material, so it was not possible to determine their textural relationship to one another or to the C1 material. They vary in internal texture (PO and POP types), mineral compositions (Table 6), and

degree of equilibration, and can be described within the standard classification scheme for chondrules in chondritic meteorites (e.g., Gooding and Keil 1981; Brearley and Jones 1998; Jones 2012). Chondrule #2 (Fig. 16b) consists of subhedral, normally-zoned olivine phenocrysts in a small amount of feldspathic mesostasis surrounded by a rim of subhedral to anhedral grains of orthopyroxene. Olivine and orthopyroxene cores are Fo ~95 and En ~98, respectively (Table 6). It is a partially equilibrated type IAB POP. Chondrule #3 (Fig. 18c) consists dominantly of orthopyroxene phenocrysts (Mg# ~95) with overgrowths of Ca-rich pyroxene, plus subhedral to anhedral grains of FeO-rich olivine (Fo ~80). It is a partially equilibrated Type IAB. Chondrule #4 (Fig. 18d) is a Type IIAB POP consisting of anhedral olivine (Fo ~79) and orthopyroxene (Mg# ~89), with one large metal (kamacite+taenite) grain (Fig. 18e). Chondrule #5 (Fig. 18f) is an unequilibrated Type IAB POP, consisting of zoned, anhedral olivine (Fo 89-99), anhedral orthopyroxene (Mg #99), and mesostasis containing acicular olivine crystals.

The CT scan of AhS 91_01 (Fig. 19a), shows that it contains additional chondrules not yet exposed, some of which are in contact with one another and the C1 matrix. Examining these chondrules could provide information on textural relationships between the chondrules and between the chondrules and the C1 matrix. Therefore, we have begun progressively polishing down the AhS 91_01 section and examining newly-exposed features. The first new feature observed is a highly brecciated area (Fig. 19b,c), which appeared in the area formerly occupied by chondrule #5 (chondrule #3 and #4 are still present). This area shows finely comminuted material consisting of angular mineral and lithic fragments <1 to 100 μm in size. Based on their textures and mineral compositions (Fig. 19d), these fragments are an intimate mix of C1 matrix material, olivine and pyroxenes similar to the ureilitic clasts in AhS 91A, and chondrule components. The C1 material in this area occurs as distinct clasts, rather than forming a matrix around the ureilitic clasts as it does in other areas of AhS 91A and AhS 671.

Oxygen Isotope Compositions

Oxygen isotope compositions for bulk samples of AhS 91A and AhS 671 (Table 7) are shown in Figure 20. The analyzed fragment of AhS 91A was separated into a main fragment that was dominated by the C1 lithology and a small chip with a "metallic" texture (based on binocular microscope observation). The main fragment (analyzed as two aliquots) had an average composition plotting on an extension of the CCAM line at $\delta^{18}O$ = 13.53 ‰ and $\delta^{17}O$ =

8.93 ‰, with $\Delta^{17}O$ = ~1.8 ‰. This does not match the composition of any known chondrite, but is very similar to the composition of a CC-like clast from the Nilpena polymict ureilite (Fig. 20a: Clayton and Mayeda 1988; Brearley and Prinz 1992) and similar to compositions of three CC-like clasts in other typical polymict ureilites (Patzek et al. 2018b). An aliquot of the "metallic" chip had a composition plotting on the terrestrial fractionation line (TFL) at $\delta^{18}O$ = -1.33. SEM observations and EMPA analyses of this chip showed only hydrous iron oxides, with a texture indicative of terrestrial alteration products. The fragment of AhS 671 (two aliquots) showed a composition slightly offset from that of AhS 91A, with $\Delta^{17}O$ = ~1.6 ‰ and slightly lower $\delta^{18}O$ = ~10.72 ‰. This composition would be consistent with a mixture of AhS 91A and a terrestrial component similar to the chip separated from AhS 91A.

Oxygen isotope compositions obtained by SIMS for various components of AhS 91_01 (Fig. 18a) are given in Table 8 and shown in Figure 20. Compositions of olivine and pyroxene in chondrules #2 and #4, and pyroxene in chondrule #3 (Fig. 18), are within the range of compositions of olivine and pyroxene in chondrules in LL ordinary chondrites (Kita et al. 2010). One analysis of FeO-rich olivine (Fo ~80) in chondrule #3 has a more ^{16}O-rich composition (Fig. 20a), suggesting that it is a relict grain, i.e., a remnant of chondrule precursor material that survived the last chondrule-forming melting event (Kunihiro et al. 2004; Ushikubo et al. 2012). Analyses of olivine and pyroxene from chondrule #5 are significantly more ^{16}O-rich (Fig. 20a) than the olivine from chondrules #2, 3, and 4, and are within the range of olivine and pyroxene in chondrules from primitive (type 3) CC (Ushikubo et al. 2012; Tenner et al. 2015). Clasts of olivine, pyroxene and plagioclase in AhS 91_01 have oxygen isotope compositions within the range of main group ureilites, ureilitic stones from AhS, and olivine, pyroxene, and plagioclase clasts in typical polymict ureilites (Fig. 20a). Five analyses from the core and zoned rim of a breunnerite grain in the C1 material (Fig. 18a) show $\Delta^{17}O$ = ~2.3±0.2 ‰ and form a $\delta^{17}O$-$\delta^{18}O$ line of slope = 0.526 (correlation coefficient 0.999) with $\delta^{18}O$ ~20 to 35.6 ‰ (Fig. 20b).

Bulk Sample Spectroscopy from 0.3 – 3.6 µm

Bulk sample spectra from 0.3 – 3.6 µm for two fragments of AhS 91A (chips and powders of each) are shown in Figure 21a (RELAB file names are given in Supplement 2). Spectra of the chips are dark (reflectance ~0.04-0.05) and relatively featureless across VNIR wavelengths. They show a strong absorption band at ~2.7 µm, indicative of water of hydration (OH^-) in

phyllosilicates. Spectra of powdered samples are similar to those of the corresponding chips but having lower reflectance (~0.03-0.04). The <125 μm powder of one fragment (91A_11) exhibits a shallow absorption at ~1.05 μm, attributable to olivine.

VNIR spectra of chips and powder samples of two AhS enstatite chondrites, AhS 2012 and AhS 1002 (Goodrich et al. 2018), measured to add to the data of Hiroi et al. (2010) for spectra of AhS stones, are also shown in Figure 21b. Both chips have very red, featureless slopes, with high reflectance values (~0.27-0.28 at 0.55 μm). The powders are also red and featureless, but with lower reflectance (0.08-0.09 at 0.55 μm). The AhS 1002 samples are more affected by terrestrial weathering than AhS 2012, evident from their stronger UV and 0.5 μm absorption features.

Microscopic Spectroscopy from 2.5 – 25 μm

We acquired μ-FTIR reflectance measurements on polished mounts of AhS 91A and AhS 671 in the 4,000-400 cm^{-1} range (2.5-25 μm). Microscopic measurements enable the targeted analysis of minerals and clasts of interest as well as allowing for mapping to obtain a bulk sample spectrum that represents coarse to solid rock (non-volume scattering) surfaces. Analytical spot sizes typically varied from ~100 – 300 $μm^2$.

A spectrum representing bulk or whole-rock 91A_1 was obtained by automated mapping of the sample at 200 $μm^2$ spatial resolution in a 10 x 9 array. After removal of pixels that did not fall completely on the sample area, 65 spectra remained, which we averaged to obtain the bulk spectrum due to the linear nature of mixing over this spectral range. Figure 22 shows this bulk spectrum compared to similarly acquired spectra of selected carbonaceous chondrites (Hamilton 2018; Hamilton et al. 2018). Like many of the CI and CM chondrites, the bulk spectrum of AhS 91A_1 exhibits an OH^- band at ~3686 cm^{-1} (~2.71 μm) indicative of the presence of serpentine group phyllosilicates. The Christiansen feature (CF), a minimum on the high wavenumber side of the silicate stretching peak, is located at ~1097 cm^{-1} / ~9.12 μm (at 2 cm^{-1} spectral sampling). This position lies between the CF positions of typical CI1 and CM meteorites, and is most consistent with petrologic type 1, 1/2, or low petrologic sub-type CM2 chondrites (Hamilton et al. 2018). The shape of the Si-O stretching region from the CF to ~695 cm^{-1} / ~14.4 μm is relatively broad, exhibits modest structure in the form of several small shoulders (at 944, 877, and 827 cm^{-1} / 10.59, 11.40, and 12.09 μm), and is not particularly well matched by any available meteorites in our collection. The broadened absorption of the bulk spectrum may

suggest the presence of an amorphous component. The smaller shoulders are attributable to a few pixels in the 91A_1 map to which pyroxene (one pixel) and fayalitic (not ureilitic) olivine contribute. Continuing across the spectrum, there is a slightly asymmetric Mg-OH absorption at ~616 cm^{-1} (16.23 μm) whose shape and position are most similar to CM1, CM1/2, and low petrologic type CM2 meteorites. The Si-O bending fundamental is located at 443 cm^{-1} in AhS 91A_1 and, not surprisingly, also bears strong similarities to the shape and position of the same feature in CI and CM1, CM1/2, and low petrologic type CM2 meteorites (Hamilton et al. 2018). Comparable spectra of CM 2.5-2.7 meteorites exhibit a lower wavenumber band minimum (~426 cm^{-1} / 23.47 μm) and additional structure in this region (e.g., a small minimum at ~490 cm^{-1} / 20.41 μm) due to the greater abundances of pyroxene and olivine they contain (e.g., Howard et al. 2015).

We also made targeted spectral measurements of areas 1 and 4 of AhS 91A_1 (Fig. 3a). Area 1 has a very consistent and feature-rich spectral shape that differs considerably from that of the bulk meteorites (Fig. 23). The area 1 spectrum has no discernible OH^- band and the Si-O stretching region (1120 to 625 cm^{-1}; 8.9 to 16.0 μm) looks quite similar to the platy or lath-like, fayalitic olivine-dominated matrix materials in $CV3_{ox}$ meteorites (e.g., Hamilton and Connolly 2012), although the Si-O bending region (<625 cm^{-1}; >16.0 μm) resembles olivine mixed with a small amount of phyllosilicate. These observations indicate the presence of one or more anhydrous compositions, consistent with the observed high abundance in area 1 of the Ca-rich silicate that is inferred from EMPA to be nearly anhydrous. It is also noteworthy that the minimum reflectance (values not shown in Fig. 23) of the bulk sample at the CF position is 4% whereas the reflectance of area 1 at the CF is ~16% – this overall brightening commonly occurs due to the presence of spectrally-neutral (in this region of the TIR) phases, such as metal and sulfide (Hamilton et al. 2018). This can be explained by a high abundance of sulfides seen in petrographic observations of area 1. We also collected an oversampled spectral map (100 μm/pixel at 25 μm spatial sampling) of area 1 in the hopes of extracting the individual component spectra using a statistical approach (factor analysis) demonstrated successfully for laboratory and remote sensing data (e.g., Bandfield et al. 2002; Hamilton and Ruff 2012). Using this approach, we recovered the spectrum of an olivine-like (Fo 55) component, but no other components, including crystalline serpentines or phyllosilicate minerals (for phyllosilicates, we searched using a test suite of spectra for samples that have been measured at temperatures

ranging from ambient to as much as 900°C: Che et al. 2011). If a disordered phyllosilicate (serpentine or clay mineral) and/or CaO component are present in area 1, as suggested based on TEM data, we do not have the correct trial spectra to extract those components from the measured AhS spectra. If these materials are present and intergrown at very small scales (<<25 μm), we also may not be able to extract their signatures with this analytical approach, which requires variability in the phase proportions between individual measurement spots/pixels.

The spectrum of AhS 91A_1, area 4 exhibits a feature at ~3687 cm^{-1} / 2.71 μm (at 4-cm^{-1} sampling) that is attributable to the fundamental hydroxyl stretching vibration in serpentines (Farmer 1974; Bishop et al. 2002). At lower wavenumbers (longer wavelengths), area 4 exhibits a distinct spectral shape (Fig. 24) that is shifted relative to a terrestrial saponite and more consistent with minerals of the serpentine group, including an Mg-OH-related band at ~641 cm^{-1} / 15.6 μm that generally is not present in other magnesian phyllosilicate group minerals (Michalski et al. 2006). The CF minimum and silicate stretching band features of cronstedtite (Fe-bearing serpentine) are shifted (~60-70 cm^{-1}) to lower wavenumbers than in Mg-serpentines and other features of cronstedtite are not apparent in the AhS area 4 spectrum (Fig. 24), indicating that the AhS composition is relatively magnesian, consistent with EMPA analyses from this area (Fig. 6).

Targeted spot analyses on AhS 671_2 and AhS 671_3 reveal the spectral character of carbonate (Fig. 25a,b) and mixed phyllosilicate/olivine (Fig. 25c,d). The positions of spectral peaks in spectra of carbonate are at 1506, 898, and 742 cm^{-1} (6.64, 11.14, and 13.48 μm); a large feature is present at the lowest wavenumbers (longest wavelengths), but the peak position is not clearly evident in our data and likely lies just beyond the 400 cm^{-1} / 25 μm limit of these data. The observed feature positions are consistent with a carbonate with an intermediate Mg-Fe composition (e.g., Lane and Christensen 1997) and is similar to magnesite and dolomite (we do not have a breunnerite spectrum for comparison), consistent with EMPA results (Fig. 9). To extract the individual mineral spectra from the mixed olivine/phyllosilicate analyses we employed factor analysis on data collected as an oversampled (100 μm spot size, 50 μm spatial resolution) 16 x 15 map (100 μm spot size, 50 μm spatial resolution) on a portion of AhS 671_03. We successfully extracted spectra consistent with magnesian serpentines (Fig. 25e) and olivine (~Fo 30-40, consistent with EMPA results, Fig. 25f). The shape of the olivine spectra in both 91A_2 and AhS 671_3 are more akin to those in the matrices of petrologic type 3

carbonaceous chondrites, as opposed to chondrule olivines, a property that may be indicative of their tabular and porous nature, as well as composition.

Noble Gas Analyses

The noble gas results are given in Tables 9-12. The isotopic compositions of all elements He-Xe can be explained with a mixture of cosmogenic (cos), primordially trapped (tr), and radiogenic (rad; very minor ^{4}He, ^{40}Ar and ^{129}Xe from decay of U, Th, ^{40}K, and ^{129}I) noble gases, as is expected for both primitive chondritic and ureilitic material (e.g., Ott 2014). In detail, cosmogenic noble gases are best visible in ^{21}Ne. The trapped noble gases of phase Q or a related "ureilitic" component (e.g., Göbel et. al. 1978) dominate ^{36}Ar, ^{38}Ar, and all Kr and Xe isotopes. Trapped HL (Heavy- and Light-enriched) gases from presolar diamonds (Huss and Lewis 1994) might contribute to the He and Ne isotopic compositions. The Ne three isotope plot (Fig. 26) shows the three fragments plotting on an apparent mixing line between trapped Ne and the cosmogenic endmember. The spread of the data points illustrates the distinct mixing ratios of the trapped and cosmogenic Ne.

Using Ne with trapped and cosmogenic endmember compositions $(^{20}Ne/^{22}Ne)_{tr}$ = 10.46 ± 0.05 (from fit through the data using $(^{21}Ne/^{22}Ne)_{tr}$ = 0.0294; Busemann et al. 2000) and $(^{21}Ne/^{22}Ne)_{cos}$ = 0.789 ± 0.016 for a typical $(^{20}Ne/^{22}Ne)_{cos}$ range from 0.70 to 0.93 (e.g., Wieler et al. 2002), we determined $^{20}Ne_{tr}$ and $^{21}Ne_{cos}$ concentrations for each of the AhS 91A fragments (Table 9). Using a physical model that predicts the production rates of cosmogenic nuclides as a function of chemical composition and shielding conditions (Leya and Masarik 2009), with two different estimates of bulk composition for AhS 91A (CI chondrite and ureilitic), we calculated cosmic ray exposure (CRE) ages (Table 13). The frequently used shielding indicator $(^{22}Ne/^{21}Ne)_{cos}$ is not appropriate for large bodies like 2008 TC_3 (average ~4 m diameter) and the production rates were averaged over most of the expected shielding depths in the asteroid (see Riebe at al. 2017a for more details). The $^{3}He/^{4}He$ ratios are between 6 and 11 × 10^{-4} (Table 9), close to the trapped HL or Q range (~1.5 × 10^{-4}, e.g., Ott 2014). Thus, $^{3}He_{cos}$ cannot reliably be determined because most ^{3}He is trapped and some ^{4}He might be radiogenic. Similarly, the $^{36}Ar/^{38}Ar$ ratios of >5.20 suggest only very small, if any, contributions from $^{38}Ar_{cos}$. Using $(^{36}Ar/^{38}Ar)_{cos}$ = 0.65 ± 0.02 (Wieler et al. 2002) and $(^{36}Ar/^{38}Ar)_{tr}$ in the range 5.31 to 5.36 (Q or air, Busemann et al. 2000) yields only very small concentrations of $^{38}Ar_{cos}$ (Table 10) with very large errors, so we do not use $^{38}Ar_{cos}$ to determine CRE ages. Similarly, significant amounts of

^{3}He may originate from trapped He components, and some ^{4}He might be radiogenic. This renders the determination of CRE ages based on ^{3}He very difficult. The most reliable CRE ages, from ^{21}Ne, averaged over both estimated chemical compositions, are between 5 and 9 Ma, lower than the ages of ~11-22 Ma reported for other Almahata Sitta stones (Riebe et al. 2017a; Meier et al. 2012, Welten et al. 2010).

Krypton and Xe isotope ratios (Tables 11,12) resemble purely trapped ratios as typical for phase Q Kr and Xe (Busemann et al. 2000). The element abundances and ratios in AhS 91A_12 and AhS 91A_15 are very similar, whereas AhS 91A_14 shows large enrichments in Ar (~11×), Kr (~2.9×), Ne (~2.5×) and He (~1.4×) relative to the other two fragments, but essentially similar Xe concentrations. This leads to high ^{36}Ar/^{132}Xe (~870) and ^{84}Kr/^{132}Xe (~2.2) ratios in AhS 91A-14, compared to these ratios in AhS 91A_12 and AhS 91A_15 (~90, ~0.8, respectively), which resemble Q gas compositions.

Density and Porosity

Results of the measurements of density and porosity for AhS 91A_18 and AhS 91A_19 are given in Table 14. The bulk densities of the two samples (2.33 ± 0.06 and 2.39 ± 0.01 g/cm^3, respectively) are within the range measured for twelve CM2 chondrites (1.88 to 2.54; median 2.20 g/cm^3) by Macke et al. (2011a), which are lower than those of any other CC except CI. In contrast, the grain density of the samples (3.69 ± 0.16 g/cm^3) is higher than those of CM2 (2.74-3.26 g/cm^3), and similar to the highest grain densities measured for CV (3.25-3.86 g/cm^3) or CO (3.17-3.78 g/cm^3) chondrites (Macke et al. 2011a). The porosity of the two samples (36.2 ± 3.0 %) is much higher than those of any CCs or other meteorite types except CI, the ungrouped CC Tagish Lake, or a few rare CM chondrites (Macke et al. 2011a,b; Bland et al. 2004; Hildebrand et al. 2006).

DISCUSSION

What Type of Meteorites are AhS 91A and AhS 671?

CC Lithology

The dominant component of AhS 91A and AhS 671 is a CC matrix-like material, which we have referred to as the C1 lithology because it appears to consist mainly, or entirely, of products of aqueous alteration (Zolensky and McSween 1988). The mineral assemblages, textures, and

mineral compositions of this lithology resemble those of CI1 meteorites, which consist almost entirely of diverse lithic fragments of aqueously altered matrix material (Brearley and Jones 1998; Bland et al. 2002). Like CI1s (Tomeoka and Buseck 1988), the CC lithology in AhS 91A and AhS 671 consists mostly of fine-grained Mg-rich serpentine and saponite, with abundant magnetite, sulfides, and carbonates. It is also similar in mineralogy and phyllosilicate Mg#s to CR1 matrix (Le Guillou et al. 2015), but differs from CR1 chondrites in not containing chondrules. It differs from CM matrices, in which cronstedtite is a major phase (Müller et al. 1977; Barber 1981; Akai 1980; MacKinnon 1980, 1982; Akai and Kanno 1986). The areas rich in fayalitic olivine in AhS 91A and AhS 671 CC bear some resemblance to CV matrices (Green et al. 1971; Kornacki and Wood 1984; Peck 1984; Keller et al. 1994; Krot et al. 1995), but the porous, tabular morphology of the olivine (Fig. 7) differs from that in most CVs (Krot et al. 1995); furthermore, other phases common in CV matrices (andradite, grossular, wollastonite, feldspathoids) are absent. Compositions of magnetite in AhS 91A and AhS 671 are like those of magnetite in CI and CR and distinct from those in CV and CK (Fig. 10). Compositions of carbonates in AhS 91A and AhS 671 (breunnerite and lesser dolomite) are most consistent with those in CI (Fig. 9), although dolomite is more abundant than breunnerite in CIs (Johnson and Prinz 1993; Endress and Bischoff 1996). They differ from carbonates in CMs, in which calcite is more abundant than dolomite (Barber 1981; Johnson and Prinz 1993; Brearley 1995) and breunnerite has not been reported (Fig. 9).

However, although this lithology appears to be most like CI1, it also shows evidence of spatially heterogeneous thermal metamorphism that resulted in dehydration, including the nearly anhydrous Ca-rich silicate phase, the absence of OH^- bands in μ-FTIR spectra of some areas of AhS 91A, and the presence of significant amounts of fayalitic olivine. In particular, the unique morphology (not seen in known CC) of magnetite clusters rimmed by fayalitic olivine (e.g., Fig. 10c) may be a product of reduction of magnetite during metamorphism (Zolotov et al. 2006). Evidence for post-aqueous alteration thermal metamorphism is seen in some CIs (Nakamura 2005; Tonui et al. 2014), and may have been common on primitive, volatile-rich bodies.

Furthermore, bulk oxygen isotope compositions of AhS 91A and AhS 671 show that it is distinct from CI and unlike any previously known chondrite (Fig. 20a). This result is underscored by Cr isotope compositions, which show that AhS 91A and AhS 671 have unique $\varepsilon^{54}Cr$ values, which are the highest of any known solar system materials (Sanborn et al. 2017; Yin et al. 2018).

511 The C1 lithology in AhS 91A and AhS 671 may, however, be related to some CC-like clasts
512 in meteoritic breccias. Carbonaceous chondrite-like clasts occur as xenoliths and microxenoliths
513 in typical polymict ureilites, HED (howardite-eucrite-diogenite) breccias, ordinary chondrite
514 regolith breccias, and Rumuruti-type chondrites, with their apparent abundance decreasing in this
515 order (Bischoff et al. 2006; Greshake 2014; Patzek et al. 2018a). In HED and ordinary
516 chondrites, most CC-like clasts are mineralogically similar to CM2 or CR2 chondrites, with CI-
517 like clasts being much less common (Zolensky et al. 1996, 2018; Herrin et al. 2011; Gounelle et
518 al. 2003; Briani et al. 2012; Patzek et al. 2018a). However, in polymict ureilites, all CC-like
519 clasts have been reported to be CI-like. Such clasts were first identified by Prinz et al. (1987) as
520 "black (opaque)" materials similar to carbonaceous chondrite matrix in the three polymict
521 ureilites known at the time (Nilpena, North Haig, EET 83309). Prinz et al. (1987) noted that
522 these clasts were "soft and friable" and consisted mostly of very fine-grained silicates with
523 magnetite, Fe,Ni sulfides, Fe-Mn-Mg carbonates, and minor ilmenite and apatite. Brearley and
524 Prinz (1992) conducted XRD, TEM and analytical microscopy on one such clast and found that
525 it consisted of very fine-grained phyllosilicates, with coarser sulfide and magnetite grains. The
526 phyllosilicates were dominated by serpentine, with lesser amounts of saponite, minor chlorite,
527 and other fine-grained and/or amorphous materials. They also identified a darker clast within the
528 main clast, indicating that the clast itself was a breccia. Brearley and Prinz (1992) showed that
529 the CC-like clasts in Nilpena were mineralogically more like CI than CM. However, one dark
530 clast from Nilpena was analyzed for bulk oxygen isotopes (Clayton and Mayeda 1988) and found
531 to be distinct from CI, as well as all other known chondrites (Fig. 20a). Patzer et al. (2018b)
532 recently reported three CC-like clasts in other typical polymict ureilites with similar oxygen
533 isotope compositions. Brearley and Prinz (1992) concluded that the CC-like clasts in polymict
534 ureilites were unique. This is supported by data for D/H ratios and S isotope ratios of a few CI-
535 like clasts in typical polymict ureilites (Patzek et al. 2017; Visser et al. 2018).
536 The C1 material in AhS 91A and AhS 671 is generally similar in mineralogy to the dark
537 clasts in typical polymict ureilites described by Prinz et al. (1987) and Brearley and Prinz (1992).
538 Furthermore, it is almost identical in oxygen isotope composition (Fig. 20a) to the dark clast
539 from Nilpena analyzed by Clayton and Mayeda (1988) and the three clasts reported by Patzer et
540 al. (2018b). However, studies of >130 CC-like xenoliths in 14 different polymict ureilites show
541 substantial diversity in the abundances and compositions of their constituents (Ikeda et al. 2000,

2003; Goodrich et al. 2004; Kita et al. 2017; Patzek et al. 2018a) and, so far, only one clast that could be considered petrologically "identical" to AhS 91A or AhS 671 has been reported (Goodrich et al. 2019a). Furthermore, bulk oxygen isotopes have been analyzed for another CC-like clast from a polymict ureilite, and found to have a composition very different from that of 91A and 671 (Goodrich et al. 2019a). Continued petrologic and isotopic studies of CC-like clasts in typical polymict ureilites and other meteoritic breccias are needed to determine whether AhS 91A and 671 are closely related to any of them.

Clasts and Chondrules

The clasts of olivine, pyroxene, plagioclase, graphite, and metal in AhS 91A and AhS 671 cannot be indigenous to the CC lithology. Although the matrices of C1 and C2 chondrites sometimes contain a small fraction (estimated <1 vol% in C1 by Brearley and Jones 1998) of relict olivine and orthopyroxene grains (Steele 1990; Leshin et al. 1997; Frank et al. 2014), the olivine and pyroxene clasts in AhS 91A and 671 are much larger than such grains (up to 3 mm vs. 400 μm). They also show sharp boundaries with the matrix, whereas relict grains in C1 and C2 have more diffuse edges (Steele 1990). Moreover, the olivine and pyroxene grains in AhS 91A and AhS 671 are compositionally distinct from those in C1/C2 (Fig. 14, 15). Plagioclase has not been reported in CC matrices. Although CC can have carbon contents up to ~8 wt.% (Pearson et al. 2006; Kerridge 1985), the carbon does not occur as large masses of graphite like those in AhS 91A and AhS 671 (Fig. 13d), but rather as widely dispersed organic compounds or poorly-graphitized carbon (Hayes 1967; Smith and Buseck 1981; Botta and Bada 2001; Alexander et al. 2017). The metal grains in AhS 91A and AhS 671 (Fig. 16) are also unlikely to belong to the CC lithology, because Fe,Ni metal is absent or extremely rare in all CC matrix materials except reduced CVs (which do not contain magnetite and so are not analogous to AhS 91A and AhS 671).

A similar argument can be made for the chondrules in AhS 91_01 (Fig. 18). Although CC with aqueously-altered matrices (C1 and C2) can contain chondrules (e.g., McSween 1979), such chondrules show various degrees of aqueous alteration (Ikeda 1983; Kojima et al. 1984; Browning et al. 1996). The chondrules in AhS 91_01 show no aqueous alteration, and therefore are not likely to be an indigenous component of the C1 material.

572 If the olivine, pyroxene, plagioclase, graphite, metal, and chondrules in AhS 91A and AhS
573 671 are not part of the C1 lithology, then they must be xenolithic. What is their provenance? The
574 olivine and pyroxene clasts can be identified as ureilitic from their compositions and internal
575 textural features. Olivines in main group ureilites, typical polymict ureilites, and ureilitic stones
576 from Almahata Sitta show characteristic compositions, with Fo ranging from ~75 to 95 (among
577 samples), a well-defined Fe/Mg-Fe/Mn trend of near-constant Mn/Mg ratio that passes through
578 the origin, and high CaO and Cr_2O_3 contents (Fig. 14). These combined features distinguish
579 ureilitic olivine from that in all other major meteorite groups (Fig. 14). The compositions of the
580 olivine clasts in AhS 91A and AhS 671 are consistent with these characteristics and encompass
581 most of the known ureilitic range. At least six distinct main group ureilite lithologies are
582 represented by these clasts. Internal textures further support ureilitic provenance. The reduced
583 zones along grain boundaries and around inclusions of graphite are a characteristic feature of
584 ureilitic olivine, as are the graphite inclusions themselves (Wlotzka 1972; Mittlefehldt et al.
585 1998). The micron-sized chromite+pyroxene symplectites in the Fo ~78-79 clasts (Fig. 12e) are
586 also a feature of ureilitic olivines of Fo 75-79 (Goodrich et al. 2013a).
587 Pyroxenes in ureilites also show characteristic compositional features. The sole or dominant
588 pyroxene in ~95% of main group ureilites is pigeonite with Wo ~6-14. Most meteoritic
589 pigeonites are significantly more ferroan than the pigeonite in ureilites (Fig. 15a). Ureilites (main
590 group ureilites, clasts in typical polymict ureilites, and ureilitic stones from AhS) represent a
591 unique occurrence of Mg-rich (Mg# ~78-92) pigeonite, which also has higher Cr_2O_3 contents
592 than low-Ca pyroxenes in most other meteorites (Fig. 15b). The pigeonite clasts in AhS 91A and
593 AhS 671 have Wo, Mg#, and Al_2O_3 and Cr_2O_3 contents consistent with ureilitic pigeonite (Fig.
594 15). The primary orthopyroxenes (i.e., ignoring shock-recrystallized pyroxenes) in ureilites also
595 have distinct compositions. They occur mostly in the more magnesian ureilites, with Mg# >~87,
596 and invariably have Wo ~4.5-4.9 (Mittlefehldt et al. 1998; Goodrich et al. 2004). Two of the
597 three orthopyroxene clasts in AhS 91A and AhS 671 have Wo, Mg#, and Al_2O_3 and Cr_2O_3
598 contents consistent with those of ureilitic orthopyroxene. The porous, reduced patches in some of
599 the pigeonite clasts (Fig. 13c) further support their ureilitic provenance. Internal textures like
600 these occur in pigeonites in some main group ureilites and many Almahata Sitta ureilites and
601 have been attributed to pyroxene-selective impact-smelting (Bischoff et al. 2010; Zolensky et al.
602 2010; Warren and Rubin 2011). From the number of distinct pigeonite compositions, at least five

603 main group ureilites are represented by these clasts. The Wo 4.5 orthopyroxene clast could be
604 derived from the most magnesian of these, based on compositions of coexisting pigeonite and
605 orthopyroxene in main group ureilites. Based on typical compositions of coexisting olivine and
606 pigeonite in main group ureilites (Mittlefehldt et al. 1998; Goodrich et al. 2004), these could be
607 the same five ureilitic lithologies that are represented by the olivine clasts in AhS 91A and AhS
608 671. The orthopyroxene clast of Wo 0.8, Mg #99.5 (Table 4, column 15) has major and minor
609 element compositions out of the range of ureilites and consistent with those of orthopyroxenes in
610 several types of chondrites (Fig. 15).
611 The plagioclase clasts in AhS 91A and 671 could also be derived from ureilites. Main group
612 ureilites do not contain plagioclase (Mittlefehldt et al. 1998), but typical polymict ureilites
613 contain a few vol. % of plagioclase as mineral and lithic clasts (Jaques and Fitzgerald 1982;
614 Prinz et al. 1987, 1988; Ikeda et al. 2000; Goodrich et al. 2004; Cohen et al. 2004; Kita et al.
615 2004, 2006; Goodrich and Wilson 2014; Goodrich et al. 2017b). These clasts span the entire
616 range from albite to anorthite, with two main populations, one "albitic" (An ~0-30) and the other
617 'labradoritic" (An ~33-70) (Ikeda et al. 2000; Cohen et al. 2004; Goodrich et al. 2017b). These
618 two populations probably represent indigenous melt lithologies complementary to main group
619 ureilites (Cohen et al. 2004; Goodrich et al. 2004; Kita et al. 2004). One Almahata Sitta stone,
620 called ALM-A (Bischoff et al. 2015b), is a trachyandesite with mineral and oxygen isotope
621 compositions resembling those of the "albitic" lithology in typical polymict ureilites. Two of the
622 three plagioclase clasts in AhS 91A and AhS 671 have major and minor (Mg, Fe) element
623 compositions (Table 4) consistent with the "albitic" lithology and ALM-A, and the third has
624 major and minor element compositions consistent with the "labradoritic" lithology.
625 Oxygen isotope compositions of the olivine, pyroxenes, and plagioclase clasts in AhS 91_01
626 (Fig. 18a) are within the range of compositions of main group ureilites and clasts in polymict
627 ureilites (Fig. 20a), and thus support the ureilitic provenance of these clasts.
628 The provenance of the graphite masses in the C1 material cannot be determined from any in
629 situ analyses we were able to make on the carbon. However, some of them have inclusions of
630 metal (Fig. 13d) of characteristically ureilitic composition (see next paragraph). Furthermore, the
631 fact that they are found with numerous other clasts derived from ureilites (which contain
632 abundant graphite) strongly suggests ureilitic provenance. The presence of minor diamond in

633 some of the graphite masses (Supplement 3) further supports this interpretation (Mittlefehldt et
634 al. 1998; Ross et al. 2011).

635 Based on composition, the metal grains in AhS 91A and AhS 671 are derived from three
636 different meteorite types – ureilites, ordinary chondrites, and enstatite chondrites. Ureilitic metal
637 is kamacite with ~1-7 wt.% Ni (Goodrich et al. 2013b). It is distinguished from kamacite in
638 ordinary chondrites and iron meteorites by its significant Si, P, and Cr contents, and from
639 kamacite in enstatite chondrites by higher Cr (Fig. 17). Thus, kamacite grains that occur in AhS
640 91A and 671 without taenite, and contain significant Si, P and Cr (e.g., Table 5, column 1), are
641 likely of ureilitic provenance. The association of Cr-bearing troilite with some of these grains
642 further supports this interpretation, as Cr-bearing troilite is common in ureilites (Goodrich et al.
643 2013b). The kamacite-taenite-troilite assemblages in AhS 91A and AhS 671 (e.g., Fig. 16a) are
644 likely derived from ordinary chondrites, considering the low abundances of Cr, P and Si in their
645 kamacite (consistent with either OC or iron meteorites; Fig. 17) in combination with their
646 textures (similar to those of kamacite-taenite-troilite particles in OC rather than the typical
647 Widmanstätten texture of iron meteorites: Brearley and Jones 1998). Cobalt contents of the
648 kamacite further narrow it down to the H group (Kallemeyn et al. 1989). The grains of Si-rich
649 kamacite in AhS 91A and 671 (e.g., Fig. 16b-d) have compositions that constrain them to being
650 from enstatite chondrites (Fig. 17). Nickel and Si contents of these grains further narrow it down
651 to EH type 4-6 (Weisberg and Kimura 2012). Enstatite chondrite provenance is also supported
652 by inclusions of enstatite and niningerite in these grains (Fig. 16b-d) (Ehlers and El Goresy 1988;
653 El Goresy et al. 1988; Weisberg and Kimura 2012; Horstmann et al. 2014).

654 Based on textures, mineralogy, and mineral compositions, the chondrules and chondrule
655 fragments in AhS 91_01 are most likely derived from type 3 OC, RC, or CC (Bischoff 2000;
656 Jones 2012; Scott and Krot 2004). Oxygen isotope compositions (Fig. 20a) of chondrules #2, #3
657 and #4 (Fig. 18b-d) are most consistent with OC. The combined Fo of olivine and Co content of
658 kamacite in chondrule #4 suggest H type (Kallemeyn et al. 1989). The ^{16}O-rich composition of
659 chondrule #5 (Fig. 20a) suggests derivation from type 3 CC.

660

661 *Summary and Implications*

662 Summarizing the petrology and oxygen isotope compositions of AhS 91A and AhS 671,
663 these stones are breccias of a type not previously known among meteorites. They are dominated

by aqueously-altered (C1) matrix material that has similarities to CI1 but also shows unique mineralogic features and oxygen and Cr isotope compositions, showing that it represents a reservoir of volatile-rich early solar system material not so far sampled by whole meteorites. The C1 matrix material encloses clasts of ureilitic olivine, pyroxene, plagioclase, graphite and metal representing at least six different ureilite lithologies, EC metal-sulfide and enstatite grains, OC metal-sulfide grains, and chondrules derived from type 3 OC and CC.

Although most of the material in AhS 91A is mineralogically similar to CI chondrites, both the bulk density and the grain density of two 91A fragments (Table 14) are higher than those of CI (Macke et al. 2011a). Two factors could account for this. First, the AhS 91A samples measured could contain ureilitic and OC type mineral clasts (no CT scans were obtained on these fragments), which would increase density relative to the phyllosilicate-dominated matrix. Second, the C1 material in AhS 91A and 671 shows indications of partial dehydration, which would also increase density. On the other hand, the porosity of AhS 91A (36%) is very similar to that of CI and similar ungrouped CC such as Tagish Lake (Macke et al. 2011a). The combination of density and porosity in AhS 91A does not match any known CC, which supports the interpretation that these stones are a previously unknown type of material.

AhS 91A and AhS 671 are the first Almahata Sitta stones to contain both ureilitic and chondritic lithologies. They contain most of the previously known AhS stone types (multiple types of ureilites, EC and OC), as well as a type of chondritic material not previously reported in AhS (C1). This suggests that AhS 91A and AhS 671 do not just give us another meteorite type to add to the inventory of Almahata Sitta stones. Rather, these stones may be giving us direct information about the structure and composition of Almahata Sitta (i.e., asteroid 2008 TC_3) overall.

Implications for the Structure and Composition of Asteroid 2008 TC_3

Two observations suggest that AhS 91A and AhS 671 could represent a substantial fraction of the pre-atmospheric mass of 2008 TC_3. First, the extreme friability of these samples suggests that materials like these could easily have disintegrated into ≤tens-of-micron-sized fragments when 2008 TC_3 impacted the atmosphere and became unrecoverable as macroscopic meteorites. Thus, they are plausible candidates for the missing >99% of the mass of the asteroid (Jenniskens et al. 2009; Shaddad et al. 2010). Second, the clasts in AhS 91A and 671 are derived from the

same meteorite types as most of the AhS stones that have been studied so far and, like the other AhS stones, are predominantly ureilitic. Thus, the mineral clasts in 91A and 671 are broken-down fragments of the same materials represented by the lithic clasts (the other AhS stones) in 2008 TC_3. Based on these considerations, a plausible model for the structure and composition of 2008 TC_3 is that it was a breccia with a fine-grained, friable matrix like the C1 material in AhS 91A and AhS 671, which enclosed a small fraction of more coherent, few cm-sized, lithic clasts of ureilitic, OC, and EC materials, as well as smaller fragments (mineral fragments, chondrules, metal-sulfide particles) derived from comminution of similar materials. In the following subsections we consider whether such a model is consistent with the VNIR reflectance spectrum and the density and porosity of 2008 TC_3.

Spectral Modeling

The reflectance spectrum of 2008 TC_3 was measured in the 0.55-1.00 μm range (Fig. 21c-d), and most closely matches F-type asteroids in the Tholen taxonomy (Jenniskens et al. 2009, 2010). F-type asteroids belong to the C complex of dark asteroids that are commonly identified with carbonaceous chondrites (Tholen and Barucci 1989; DeMeo et al. 2009, 2015). The albedo of the asteroid was not directly measured, but the average F-type albedo of 0.046 (Mainzer et al. 2011) is consistent with independent estimates of the asteroid's size (Jenniskens et al. 2009). Albedo estimates ranging from 0.046 to 0.12 (at 0.55 μm) have been proposed from laboratory spectra of some of the ureilitic AhS stones (Jenniskens et al. 2009; Hiroi et al. 2010).

Hiroi et al. (2010) obtained reflectance spectra of chips and powders of ten AhS ureilites and one ordinary chondrite (Fig. 21b) and used least-squares modeling of linear combinations of these spectra to fit the spectrum of 2008 TC_3 in order to constrain the structure and composition of the asteroid. He found that mixtures dominated by chips and coarse powders of the ureilites, with only a small component (~4-10%) of OC, reproduced the main features of the asteroid spectrum (Fig. 21c,d), suggesting that ureilitic material dominated the surface of 2008 TC_3.

We extended this modeling to include the data obtained here for AhS 91A (Fig. 21a) and the enstatite chondrite (EC) stones AhS 1002 and AhS 2012 (Fig. 21b). Critical features of the asteroid spectrum are the lack of a strong spectral downturn shortward of ~0.7-0.8 μm and a shallow absorption at ~0.9 μm attributable to pyroxene. We parameterized these features as the 700/550 nm, 900/550 nm, and 1000/900 nm ratios, and used these as criteria for constructing

linear mixtures of small numbers of components (4-5) that plausibly matched the spectrum of the asteroid. The asteroid spectrum used was the same 55-pt averaged spectrum that was used in Hiroi et al. (2010). Albedo was not a fixed constraint. We first focused on testing how large a component of AhS 91A would be consistent with the asteroid spectrum. Two of the best-fit mixtures from this modeling (mix 2 and mix 5) are shown in Figure 21c,d (Table 16).

These two spectra show that mixtures of AhS ureilites + 0-3% AhS OC + 70-79% AhS 91A provide fits to the asteroid spectrum that are comparable in quality to those of the ureilite + OC mixtures of Hiroi et al. (2010) within the uncertainty of the asteroid spectrum, and therefore are consistent with there being a significant component of AhS 91A-like material in the asteroid. Furthermore, adding large fractions of AhS 91A to ureilites results in lower albedo values (Fig. 21d) that are within the range of those of F-type asteroids (<0.09, average 0.046; Mainzer et al. 2011), whereas the ureilite + OC mixtures of Hiroi et al. (2010) are not. This is a strong argument for there being a large component of AhS 91A-like material in the asteroid, because none of the other AhS stones studied so far (by VNIR reflectance spectroscopy) have lower albedos than the ureilites.

We then tested how large a component of EC would be consistent with the asteroid spectrum by adding up to 30% EC chips or powders to one of the ureilite + OC + AhS 91A mixtures (Fig. 21c). Results show that addition of 30% EC chips or powders (the percentage of EC among currently studied non-UOK AhS stones) results in a spectrum that is outside the uncertainty of the 55-pt averaged spectrum for 2008 TC_3 over much of its spectral range. Addition of even 10% EC chips or powders results in a spectrum that deviates significantly from the averaged asteroid spectrum (though consistent with it within uncertainty) and therefore appears implausible.

Thus, based on currently available spectra for AhS stones, it is likely that asteroid 2008 TC_3 consisted dominantly of ureilitic and AhS 91A-like materials, with as much as 40-70% of the latter, and only small amounts (<10% each) of OC, EC and other meteorite types.

Density and Porosity

The bulk density determined for AhS 91A (2.35 ± 0.05 g/cm^3) is lower than the average bulk density (~2.8 g/cm^3) of 42 AhS ureilites (Welten et al. 2010), and significantly lower than densities of other AhS stone types such as EC (e.g., 3.5 g/cm^3) (Shaddad et al. 2010). It is also much closer than the ureilites to the bulk density estimates of ~1.7-2.2 g/cm^3 for asteroid 2008

757 TC_3 (Welten et al. 2010). The porosity of AhS 91A (36%) is higher than the porosities of 36 of
758 the 42 AhS ureilites measured, and within the range of estimates of porosity (33-50%) of the
759 asteroid (Welten et al. 2010). These physical properties of AhS 91A are consistent with the
760 results of the spectral modeling suggesting that material like AhS 91A could have comprised a
761 large fraction of the asteroid. If we accept the argument of Welten et al. (2010) that the lower
762 density (e.g., ~1.7 g/cm^3) and higher porosity values (e.g., 50%) determined for the asteroid are
763 the most robust, then AhS 91A is still denser and less porous than the asteroid. This is, in fact,
764 consistent with the observation that the bulk of the asteroid disintegrated in the atmosphere,
765 while AhS 91A survived. The asteroid could have contained some less-dense, more-porous
766 material that we have not sampled, or it could have consisted mainly of a less-dense, more-
767 porous version of AhS 91A. However, it is also likely that the asteroid had significant
768 macroporosity (Consolmagno et al. 2008), which could account for the lower bulk density of the
769 asteroid compared to AhS 91A and is consistent with its low strength and fragmentation behavior
770 (Jenniskens et al. 2009).
771
772 **Implications for the Formation of Asteroid 2008 TC_3**
773 At least thirteen different parent asteroids are represented among the AhS stones (Horstmann
774 and Bischoff 2014; Goodrich et al. 2018). Two types of model have been proposed to explain
775 how all these materials became mixed together in asteroid 2008 TC_3: 1) secondary accretion
776 models (Bischoff et al. 2010; Gayon-Markt et al. 2012; Horstmann and Bischoff 2014; Scott et
777 al. 2018); and 2) regolith models (Herrin et al. 2010; Hartmann et al. 2011; Goodrich et al.
778 2015a). Both models begin with catastrophic impact disruption of the ureilite parent body (UPB),
779 an event which has been proposed based on evidence independent of AhS (Takeda 1987; Warren
780 and Kallemeyn 1992; Goodrich et al. 2004, 2015a; Downes et al. 2008; Herrin et al. 2010;
781 Michel et al. 2015), and which likely occurred at ~5 Ma after CAI (Goodrich et al. 2010, 2015).
782 Secondary accretion models for 2008 TC_3 posit that at the time of the catastrophic disruption,
783 abundant fragments of mixed chondritic debris were present around the UPB and re-accreted
784 along with the ureilitic fragments to form mixed 2nd generation asteroids, one of which spawned
785 2008 TC_3. In contrast, regolith models for 2008 TC_3 posit that in the aftermath of the
786 catastrophic disruption, daughter bodies consisting solely of ureilitic materials formed by
787 gravitational re-accretion of subsets of fragments from the shattered parent (Michel et al. 2001,

788 2015). Over an extended period of time (tens of millions to billions), these ureilitic daughter
789 bodies then developed regoliths consisting of comminuted fragments of their host ureilitic
790 lithologies, as well as surviving remnants of foreign impactors. Goodrich et al. (2015a) suggested
791 that one daughter body could be the source of all ureilitic material in our collections – main
792 group ureilites from the interior, typical polymict ureilites (from deep, consolidated regolith
793 ("asteroidal megaregolith"), and AhS from shallower, less coherent regolith.
794 These two formation models make distinct predictions for the overall structure and
795 composition of the asteroid. The secondary accretion model predicts that 2008 TC_3 consisted of
796 centimeter(s)-sized, loosely agglomerated lithic components (i.e., similar to the studied AhS
797 stones), and broke up mainly into monolithologic fragments along their original boundaries, with
798 some of these fragments becoming the recovered stones (Bischoff et al. 2010). This suggests that
799 the asteroid had relatively uniform clast sizes similar to those of the fallen fragments, and no
800 strong distinction between clasts and matrix. In contrast, the regolith model predicts large
801 variations in clast sizes and a distinct clast-matrix structure.
802 The structure of the AhS 91A and AhS 671 breccias strongly suggests that they formed in a
803 regolith environment. Regolith (fragmentary debris) is produced through multiple large and
804 small impacts onto an asteroid's surface over an extended period of time, leading to
805 fragmentation, comminution, and redistribution of both indigenous asteroidal material and
806 surviving fragments of impactors (McKay et al. 1989; Bischoff et al. 2006). The products of
807 these combined processes include both regolith breccias (which resided on the outermost few
808 mm of the surface for long enough to acquire solar wind implanted gases), and fragmental
809 breccias, which formed at various depths below the surface and include materials that were not
810 exposed to space for long enough to acquire solar gases. The observations that the clasts in AhS
811 91A and AhS 671 are small fragments of their parent meteorite types (i.e., ureilitic mineral
812 fragments rather than complete ureilitic assemblages, enstatite chondrite metal grains rather than
813 a representative piece of an enstatite chondrite, OC chondrules rather than a representative piece
814 of an OC), and that diverse types of clast are intimately mixed over short distances, are
815 consistent with regolith processes, and inconsistent with the predictions of the secondary
816 accretion model. In addition, the physical properties of AhS 91A (i.e., much higher porosity than
817 seen in CC of similar density) suggest that this material has been significantly "shaken and
818 stirred," as would occur in a regolith environment. Based on the absence (so far) of SW gases in

AhS 91A and AhS 671, they are classified as fragmental breccias, which we argue formed dominantly in sub-surface layers of a regolith environment.

However, on what type of parent asteroid did this regolith form? If these meteorites had been discovered independent of the other AhS stones, they would probably be considered a new type of carbonaceous chondrite breccia, formed on a carbonaceous chondrite asteroid with the ureilite, ordinary chondrite, and enstatite chondrite materials being foreign. Instead, we know that they are pieces of asteroid 2008 TC_3, which has been assumed to be a ureilitic asteroid based on the predominance of ureilites among the studied AhS stones (Horstmann and Bischoff 2014; Goodrich et al. 2015a). This apparent paradox can be resolved by recognizing that regolith can be extremely heterogeneous, with some regions being dominated by material from a single impactor. In fact, two other types of asteroids – Vesta (a differentiated asteroid with a basaltic crust), and Psyche (thought to be metallic) – have extensive dark areas on their surfaces that are interpreted as remnants of CC-like impactors (Reddy et al. 2012, 2017; De Sanctis et al. 2012; Turrini et al. 2014; Takir et al. 2017). Thus, we hypothesize that 2008 TC_3 was a fragment of the regolith of a ureilitic asteroid, with AhS 91A and AhS 671 representing a volume of regolith that was dominated by the remnant of a CC-like body that impacted into an already well-gardened (finely comminuted) mixture of ureilitic + impactor-derived (e.g., OC and EC) fragments. Such an interpretation is supported by the dominance of ureilitic material in both AhS 91A/671 and AhS stones overall, and by comparisons between AhS and typical polymict ureilites discussed below.

Noble Gases – The Apparent Absence of Solar Wind Implanted Gases

Regolith breccias in meteorite collections are defined by their brecciated nature and the presence of solar wind (SW) derived noble gases that are implanted into the grain surfaces (100s of nm) in the upper meters of the regolith while the grains are still being impact-gardened, prior to final compaction and lithification (Bischoff et al. 2006, 2018a). Typically, the gases are abundant and can easily dominate over the other noble gas components, particularly in He and Ne. Thus, the detection of SW in AhS 91A fragments would be unequivocal support for the regolith model suggested above.

The noble gas results obtained here for AhS 91A do not obviously show a Ne-SW component (Fig. 26), but they do not exclude the possibility that one is present. For example, the

trapped endmember in all three samples could be a mixture of HL and SW in constant proportions (as indicated by the nearly constant trapped $^{20}Ne/^{22}Ne$ ratio of all samples, Fig. 26). However, it is also possible that the primordially trapped Ne component has a $^{20}Ne/^{22}Ne$ ratio above the typically dominating one in CI chondrites of HL (8.5) but well below SW-Ne (12.5 - 13.7, Fig. 26). This component would have a $^{20}Ne/^{22}Ne$ ratio of ~10.45, similar to what is found for carbonaceous carriers in carbonaceous chondrites (Q-gases) and the carbon-rich veins of ureilites (Göbel et al. 1978). The nearly constant trapped $^{20}Ne/^{22}Ne$ ratio of all three AhS fragments, including AhS 91A_14 with the largest trapped ^{20}Ne concentration (2× more than in the other two, Table 9), supports this interpretation, as a significant presence of SW-Ne in AhS 91A_14 would increase the trapped $^{20}Ne/^{22}Ne$ ratio considerably. Furthermore, AhS 91A_14 also contains an Ar-, Kr- and Ne-rich component ("subsolar") that plots at the upper right end of the trend observed by Göbel et al. 1978 in their Figure 8 for several ureilites with strongly elevated $^{36}Ar/^{132}Xe$ and $^{84}Kr/^{132}Xe$ ratios. All noble gas patterns taken together may suggest that AhS 91A_14 simply contained more of the ureilitic, gas-rich material that is suggested to be carried in C-rich veins (Göbel et al. 1978), diamond or amorphous C (see, e.g., Wieler et al. 2006, and references therein) whereas AhS 91A_12 and AhS 91A _15 contain more of the C1 material with typical Q-like elemental compositions.

On the other hand, it is possible that the SW component is present in AhS 91A but was not detected in our analyses. It has been shown that a SW-Ne component in grain surfaces can be hidden in analyses of bulk samples (i.e., swamped by the SW-poor grain interiors), particularly for CC samples that contain high concentrations of trapped gases (e.g., CI Ivuna: Riebe et al., 2017b). In such cases, minor contributions of SW can only be detected during stepwise gas-extraction with a large number of steps, such as applied with the closed-system step etching technique (Riebe et al. 2017b). Thus, the presence or absence of SW gases in AhS 91A cannot be determined without further analyses.

The absence of SW gases in previously studied AhS stones (Murty et al. 2010; Ott et al. 2010; Welten et al. 2010; Meier et al. 2012; Nagao et al. 2014; Riebe et al. 2017a) has been cited as an argument against a regolith origin for 2008 TC_3 (Horstmann and Bischoff 2014). However, all previously analyzed AhS samples were from the interiors of well-consolidated stones, which we interpret as having been the larger clasts in 2008 TC_3 (a volumetrically minor component). SW gases would not necessarily be expected in such samples, even if they were derived from a

881 regolith environment (see discussion in Riebe et al. 2017a). Further, even the complete absence
882 of SW gases in AhS 91A does not preclude a regolith origin. Solar gases are only implanted in
883 the top millimeter of an asteroidal surface (Wieler et al. 1986), and even extensive gardening
884 may not redistribute affected grains homogeneously in sub-surface regolith layers. Solar gases in
885 the typical polymict ureilites EET 83309 and 87720 are known to be heterogeneously distributed
886 (Ott et al. 1990; Rai et al. 2003), showing that some bulk samples of even strictly defined
887 (Bischoff et al. 2006) regolith breccias can be devoid of SW gases. All typical polymict ureilites
888 are sufficiently similar petrographically that they are likely to have had a common origin
889 (Goodrich et al. 2004; Downes et al. 2008); thus, the fact that some of them are regolith breccias
890 (SW gas-bearing) implies that all of them (including the fragmental breccias) formed in a
891 regolith environment. By anology, the absence of SW in AhS 91A does not rule out 2008 TC_3
892 having formed as regolith.
893 AhS 91A has a low CRE (~5-9 Ma) compared with the previously analyzed AhS chondrites
894 and ureilites (~11-22 Ma: Welten et al. 2010; Meier et al. 2012; Riebe et al. 2017a). Riebe et al.
895 (2017a) suggested that the large spread in CRE ages in the AhS samples could be due to
896 irradiation in a regolith environment. In such an environment, different clasts will spend different
897 lengths of time in the upper ~2 m layer where they are exposed to cosmic rays producing
898 cosmogenic noble gases, resulting in a spread in CRE ages. The low CRE ages of AhS 91A
899 increase the CRE age spread of the AhS samples, consistent with a regolith origin of Almahata
900 Sitta.
901
902 *Comparisons with Typical Polymict Ureilites*
903 Similarities between typical polymict ureilites and AhS have been argued to support the
904 regolith model for formation of 2008 TC_3 (Goodrich et al. 2015a). As mentioned above, typical
905 polymict ureilites are fragmental and regolith breccias that are dominated by ureilitic materials
906 but also contain multiple types of chondritic and non-ureilitic achondritic clasts (Prinz et al.
907 1986, 1987; Goodrich et al. 2004, 2015c, 2016, 2017c,d; Bischoff et al. 2006; Downes et al.
908 2008; Ross et al. 2010). They are unique among meteoritic breccias for the large diversity of
909 their foreign clasts (Bischoff et al. 2006). What makes AhS anomalous, then, is not that it
910 contains many different meteorite types, but that it disaggregated in the atmosphere and its clasts
911 landed on Earth as individual stones.

912 Goodrich et al. (2015a) argued that the differences between AhS and typical polymict
913 ureilites were principally differences in structure (i.e., grain size, grain and/or clast size
914 distribution, degree of lithification). The range of types and relative abundances of non-ureilitic
915 materials in AhS do appear to differ from those in typical polymict ureilites, at least based on the
916 AhS stones that have been studied to date. Enstatite chondrites and unique enstatite achondrites
917 dominate among non-ureilitic Almahata Sitta stones (Table 15), whereas enstatite meteorite
918 clasts are rare in typical polymict ureilites (Goodrich et al. 2015b). However, Boleaga and
919 Goodrich (2018) found that half of observed xenolithic metal-sulfide grains in several polymict
920 ureilites were derived from enstatite chondrites, indicating that enstatite chondrites did contribute
921 significant material. Furthermore, our spectral modeling (Fig. 21c) showed that enstatite
922 chondrites could not have been as abundant in 2008 TC_3 as they are among currently studied
923 AhS stones, but perhaps were concentrated relative to other stone types during the fall or
924 recovery.

925 Another apparent difference is that hydrous CC-like clasts are the most abundant foreign
926 clast type (both in numbers and volume) in typical polymict ureilites (Goodrich et al. 2015b)
927 whereas prior to the discovery of AhS 91A and AhS 671, no hydrous CCs had been found among
928 AhS stones (Bischoff et al. 2010; Horstmann and Bischoff 2014). The C1 material in AhS 91A
929 and AhS 671 is therefore a critical addition to the inventory of AhS meteorite types, particularly
930 considering its mineralogic and oxygen isotope similarites to the CC-like clasts in typical
931 polymict ureilites (Clayton and Mayeda 1988; Brearley and Prinz 1992; Patzek et al. 2018b;
932 Goodrich et al. 2019a,b). The presence of this component in AhS greatly strengthens the analogy
933 between AhS and typical polymict ureilites, and thus supports the interpretation that 2008 TC_3
934 (like typical polymict ureilites) is a piece of ureilitic regolith.
935
936 **Implications for Reflectance Spectroscopy of Asteroids**
937 Regardless of the overall fraction of CC-dominated materials in 2008 TC_3, AhS 91A and
938 AhS 671 provide direct evidence that such regions exist in ureilitic regolith. This has important
939 implications for asteroid spectroscopy, because such regions would have an ~2.7 μm absorption
940 band due to the water of hydration in their phyllosilicates (Fig. 21c,d). Depending on the areal
941 extent of these regions, the ~2.7 μm band could be detectable in disk-resolved asteroid spectra.
942 The presence of 2.7-3.0 μm band is usually considered diagnostic of a carbonaceous chondrite

943 asteroid (Rivkin 2012; Rivkin et al. 2015). However, recent investigations have found that the
944 surfaces of Vesta (a basaltic asteroid) and Psyche (thought to be a metal-rich asteroid) have dark
945 regions that show 2.7-3 μm absorption bands that are attributed to contamination by CC
946 impactors (Reddy et al. 2012, 2017; DeSanctis et al. 2012; Turrini et al. 2014; Takir et al. 2017).
947 The discovery of AhS 91A and AhS 671 shows that ureilitic asteroids can also have such
948 regions. Further, small asteroidal fragments consisting wholly of ureilitic regolith (e.g., 2008
949 TC_3?) could have CC-dominated regions that constitute a significant fraction of their mass, in
950 which case even disk-averaged spectra might show a 2.7-3.0 μm band leading to an incorrect
951 interpretation of asteroid type.
952
953 **Summary**
954 Almahata Sitta stones 91A and 671 are the first AhS stones to contain both ureilitic and
955 chondritic lithologies. They are friable breccias, consisting of a hydrous CC-like lithology that
956 encloses clasts of olivine, pyroxenes, plagioclase, graphite, and metal-sulfide, as well as
957 chondrules and chondrule fragments. The CC lithology consists mainly of fine-grained
958 serpentine and saponite, magnetite, carbonates (breunnerite and dolomite), fayalitic olivine, an
959 unidentified Ca-rich silicate phase, and Fe,Ni sulfides. It has mineralogic similarities to known
960 CI, but also shows heterogeneous thermal metamorphism (dehydration). Its bulk oxygen isotope
961 composition ($\delta^{18}O$ = 13.53‰, $\delta^{17}O$ = 8.93‰) is unlike that of known CC, but essentially
962 identical to that of a several CC-like clasts in typical polymict ureilites. Its Cr isotope
963 composition shows higher $\varepsilon^{54}Cr$ than any known meteorite. The clasts and chondrules do not
964 belong to the CC lithology. The olivine, pyroxene, plagioclase, graphite, and some of the metal-
965 sulfide clasts are ureilitic and represent at least six main group ureilite lithologies. The
966 chondrules are most likely derived from OC and/or type 3 CC. Some of the metal-sulfide clasts
967 are derived from EC.
968 AhS 91A and AhS 671 provide direct information about the structure and composition of
969 asteroid 2008 TC_3 overall and could represent a substantial fraction of its pre-atmospheric mass.
970 Their friability makes them plausible candidates for the bulk of the asteroid that was lost in the
971 atmosphere. Spectral modeling using laboratory spectra of AhS stones suggest that 2008 TC_3
972 consisted dominantly of ureilitic and AhS 91A-like materials, with as much as 70% of the latter,
973 and <10% of OC, EC and other meteorite types. Physical properties of AhS 91A are also

consistent with materials like this comprising a large fraction of the asteroid. Its bulk density (2.35 g/cm^3) is lower than densities of most AhS ureilites and other stone types, and closer to estimates for the asteroid (1.7-2.2 g/cm^3). Its porosity (36%) is within the range estimated for the asteroid (33-50%). Nevertheless, the fragmentation behavior of the asteroid suggests that it had significant macroporosity.

The texture of AhS 91A and AhS 671 supports the hypothesis that 2008 TC_3 represents regolith developed on a ureilitic asteroid. The observations that the clasts in these fragmental breccias are small, unrepresentative fragments of their parent meteorite types, and that diverse types of clast are intimately mixed, are consistent with regolith processes. The absence of a solar wind Ne component implies formation dominantly in sub-surface layers that were not directly exposed to space for long enough to acquire solar gases. The observed spread in CRE ages among AhS stones (increased by AhS 91A) also argues for irradiation in a regolith environment where different clasts spend different amounts of time in the uppermost layers.

AhS 91A and AhS 671 provide direct evidence that CC-dominated regions exist in ureilitic regolith. Such regions would have an ~2.7 μm absorption band due to the water of hydration in their phyllosilicates, which could be detectable in disk-resolved asteroid spectra. The presence of 2.7-3.0 μm band is usually considered diagnostic of a primitive, CC-like asteroid. AhS 91A and AhS 671 show that this interpretation may not always be correct.

Acknowledgements: We are grateful to Dave Draper and Lindsay Keller of ARES, JSC for making the JSC electron-beam facilities available for this work. We thank Allan Treiman and Tom Burbine for helpful discussions and encouragement. We thank Jessie Maisano and Matthew Colbert at the University of Texas (Austin), and Michele Secco at the University of Padova, for conducting XRCT scans. We thank Maciej Śliwiński for assisting with SIMS analyses of carbonate and running multiple standards. We appreciate the helpful reviews from Ed Cloutis, Alan Rubin, Addi Bischoff, and the Associate Editor Adrian Brearley. This work was supported by NASA grants 80NSSC17K0165, NNX17AH09GS03, and 80NSSC19K0507. WiscSIMS is partly supported by NSF (EAR03-19230, EAR-1658823). MR and HB thank the Swiss National Science Foundation for support through the framework of the NCCR "PlanetS" and grant P2EZP2_165234. This is LPI contribution #xxxx.

REFERENCES

Afiattalab F. and Wasson J. T. 1980 Composition of the metal phases in ordinary chondrites: implications regarding classification and metamorphism. *Geochimica et Cosmochimica Acta* 44:431-446.

Akai J. 1980. Tubular form of interstratified mineral consisting of a serpentine-like layer plus two brucite-like sheets newly found in the Murchison (C2) meteorite. *Memoirs of the National Institute for Polar Research Special Issue* 17:299-310.

Akai J. and Kanno J. 1986. Mineralogical study of matrix- and groundmass-phyllosilicates, and isolated olivines in Yamato-791198 and -793321: With special reference to new find of 14Å chlorite in groundmass. *Memoirs of the National Institute for Polar Research Special Issue* 41:259-275.

Alexander C. M. O'D., Cody G. D., De Gregorio B. T., Nittler L. R., and Stroud R. M. 2017. The nature, origin, and modification of insoluble organic matter in chondrites, the major source of Earth's C and N. *Chemie der Erde-Geochemistry* 77:227-256.

Bandfield J. L., Edgett K. S., and Christensen P. R. 2002. Spectroscopic study of the Moses Lake dune field, Washington: Determination of compositional distributions and source lithologies. *Journal of Geophysical Research* 107;5092, doi:5010.1029/2000JE001469.

Barber D. J. 1981. Matrix phyllosilicates and associated minerals in C2M carbonaceous chondrites. *Geochimica et Cosmochimica Acta* 45:945-970.

Barber D. J. 1985. Phyllosilicates and other layer-structured materials in stony meteorites. *Clay Minerals* 20:415-454.

Benedix G. K., McCoy T. J., Keil K., Bogard D. D., and Garrison D. H. 1998. A petrologic and isotopic study of winonaites: Evidence for early partial melting, brecciation, and metamorphism. *Geochimica et Cosmochimica Acta* 62:2535-2553.

Bischoff A. 2000. Mineralogical characterization of primitive, type-3 lithologies in Rumuruti chondrites. *Meteoritics & Planetary Science* 35*:*699-706.

Bischoff A., Scott E. R. D., Metzler K., and Goodrich C. A. 2006. Nature and origin of meteoritic breccias. In *Meteorites and the early solar system II*, edited by Lauretta D. S. and McSween H. Y. Jr. Tucson, Arizona: The University of Arizona Press. pp. 679-714.

Bischoff A., Horstmann M., Pack A., Laubenstein M., and Haberer S. 2010. Asteroid 2008 TC_3 – Almahata Sitta: a spectacular breccia containing many different ureilitic and chondritic lithologies. *Meteoritics & Planetary Science* 45:1638–1656.

Bischoff A., Vogel N., and Roszjar J. 2011. The Rumuruti chondrite group. *Chemie der Erde* 71:101-133.

Bischoff A., Ebert S., Patzek M., Horstmann M., Pack A., Barrat J.-A., and Decker S. 2015a. New individuals from the Almahata Sitta strewn field: Old friends and brand-new fellows (abstract #5092). 78th Annual Meeting of the Meteoritical Society.

Bischoff A., Horstmann M., Barrat J-A., Chaussidon M., Pack A., Herwatz D., Ward D., Vollmer C., and Decker S. 2015b. Trachyandesitic volcanism in the early Solar System. *Proceedings of the National Academy of Science* 111:12689-12692.

Bischoff A., Ebert S., Patzek M., Horstmann M., Pack A., and Decker S. 2016. Almahata Sitta news: well-known varieties and new species in the zoo (abstract #6319). 79th Annual Meeting of the Meteoritical Society.

Bischoff A., Schleiting M., Wieler R., and Patzek M. 2018a. Brecciation among 2280 ordinary chondrites - Constraints on the evolution of their parent bodies. *Geochimica et Cosmochimica Acta* 238:516-541.

Bischoff A., Kraemer A. –K., Klemm K. I., and Decker S. 2018b. News from the Almahata Sitta Strewn field – seven new samples: three ureilities, three enstatite chondrites, and one ordinary chondrite (abstract #2067). 81st Annual Meeting of the Meteoritical Society.

Bischoff A., Lentfort S., Möhlmann K., Klemm K., and Haberer S. 2019. Mineralogical characteristics of 20 new samples from the Almahata Sitta Strewnfield (abstract #6030). 82nd Annual Meeting of the Meteoritical Society.

Bishop J. L., Murad E., and Dyar M. D. 2002. The influence of octahedral and tetrahedral cation substitution on the structure of smectites and serpentines as observed through infrared spectroscopy. *Clay Minerals* 37:617-628.

Bland P. A., Cressey G., Alard O., Rogers N. W., Forder S. D., and Gounelle M. 2002. Modal mineralogy of carbonaceous chondrites, and chemical variation in chondrite matrix (abstract #1754). 33rd Lunar and Planetary Science Conference. CD-ROM.

Bland P. A., Cressey G., and Menzies N. 2004. Modal mineralogy of carbonaceous chondrites by X-ray diffraction and Mossbauer spectroscopy. *Meteoritics & Planetary Science* 39:3-16.

Boleaga Y. and Goodrich C. A. 2019. Xenolithic Fe,Ni metal in polymict ureilite meteorites (abstract #1622). 50th Lunar and Planetary Science Conference.

Borovička J. and Charvát Z. 2009. Meteosat observation of the atmospheric entry of 2008 TC_3 over Sudan and the associated dust cloud. *Astronomy and Astrophysics* 507:1015–1022.

Böstrom K. and Fredriksson K. 1966. Surface conditions of the Orgueil meteorite parent body as indicated by mineral associations. *Smithsonian Miscellaneous Collections* 151:1-39.

Botta O. and Bada J. L. 2002. Extraterrestrial organic compounds in meteorites. *Surveys in Geophysics* 23:411-467.

Brearley A. J. 1995. Aqueous alteration and brecciation in Bells, an unusual, saponite-bearing CM carbonaceous chondrite. *Geochimica et Cosmochimica Acta* 59:2291-2317.

Brearley A. J. and Jones R. H. 1998. Chondritic meteorites. In *Planetary Materials*, edited by Papike J. J. Washington, D.C.: Mineralogical Society of America. pp. 3.1-3-398.

Brearley A. J. and Prinz M. 1992. CI chondrite-like clasts in the Nilpena polymict ureilite. Implications for aqueous alteration processes in CI chondrites. *Geochimica et Cosmochimica Acta* 56:1373-1386.

Briani G., Gounelle M., Bourot-Denise M., and Zolensky M. E. 2012. Xenoliths and microxenoliths in H chondrites: Sampling the zodiacal cloud in the asteroid Main Belt. *Meteoritics & Planetary Science* 47:880-902.

Browning L. B., McSween H. Y., Jr., and Zolensky M. E. 1996. Correlated alteration effects in CM carbonaceous chondrites. *Geochimica et Cosmochimica Acta* 60:2621-2633.

Buroni A. and Folco L. 2008. Frontier Mountain meteorite specimens of the acapulcoite-lodranite clan: Petrography, pairing, and parent-rock lithology of an unusual intrusive rock. *Meteoritics & Planetary Science* 43:731-744.

Busemann H., Baur H., and Wieler R. 2000. Primordial noble gases in "phase Q" in carbonaceous and ordinary chondrites studied by closed-system stepped etching. *Meteoritics & Planetary Science* 35:949-973.

Che C., Glotch T. D., Bish D. L., Michalski J. R., and Xu W. 2011. Spectroscopic study of the dehydration and/or dehydroxylation of phyllosilicate and zeolite minerals. *Journal of Geophysical Research* 116:E05007.

Chesley S., Chodas P., and Yeomans S. 2008. NASA/JPL Near-Earth Object Program Office Statement. (http://neo.jpl.nasa.gov/news/2008tc3.html) (4 November, 2008).

Clayton R. N. and Mayeda T. K. 1988. Formation of ureilites by nebular processes. *Geochimica et Cosmochimica Acta* 52:1313-1318.

Clayton R. N. and Mayeda T. K. 1996. Oxygen isotope studies of achondrites. *Geochimica et Cosmochimica Acta* 60:1999-2017.

Cohen B. A., Goodrich C. A., and Keil K. 2004. Feldspathic clast populations in polymict ureilites: stalking the missing basalts from the ureilite parent body. *Geochimica et Cosmochimica Acta* 68**:**4249–4266.

Consolmagno G. J., Britt D. T., and Macke R. J. 2008. The significance of meteorite density and porosity. *Chemie der Erde Geochemistry* 68:1-29.

Day J. M. D., Corder C. A., Rumble D. III, Assayag N., Cartigny P., and Taylor L. A. 2015. Differerentiation processes in FeO-rich asteroids revealed by achondrite Lewis Cliff 88763. *Meteoritics & Planetary Science* 50:1750-1766.

DE Leuw S., Rubin A. E., and Wasson J. T. 2010. Carbonates in CM chondrites: Complex formational histories and comparison to carbonates in CI chondrites. *Meteoritics & Planetary Science* 45:513-530.

De Sanctis M. C., Combe J. -Ph., Ammannito E., Palomba E., Longobardo A., McCord T. B., Marchi S., Capaccioni F., Capria M. T., Mittlefehldt D. W., Pieters C. M., Sunshine J., Tosi F., Zambon F., Carraro F., Fonte S., Frigeri A., Magni G., Raymond C. A., Russell C. T., and Turrini D. 2012. Detection of widespread hydrated materials on Vesta by the VIR imaging spectrometer on board the Dawn mission. *Astrophysics Journal* 758:1-5, L36.

Deer W. A., Howie R. A. and Zussman J. 1962. Rock forming minerals. Volume 3. Sheet silicates. London: Longman Group Limited. 269 pages.

Delaney J. S., Zanda B., Clayton R. N., and Mayeda T. 2000. Zag(b): A ferroan achondrite intermediate between brachinites and lodranites (abstract #1745). 31st Lunar and Planetary Science Conference. CD-ROM.

DeMeo F. E., Binzel R. P., Slivan S. M., and Bus S. J. 2009. An extension of the Bus asteroid taxonomy into the near-infrared. *Icarus* 202**:**160-180.

DeMeo F. E., Alexander C. M. O'D., Walsh K. J., Chapman C. R., and Binzel R. P. 2015. The compositional structure of the asteroid belt. In Asteroids IV, edited by Michel P., DeMeo F. E., and Bottke W. F. Tucson: The University of Arizona Press. pp. 13-42.

DE Sanctis M. C., Combe J. –PH., Ammannito E., Palomba E., Longobardo A., McCord T. B., Marchi S., Capaccioni F., Capria M. T., Mittlefehldt D. W., Pieters C. M., Sunshine J., Tosi F., Zambon F., Carraro F., Fonte S., Frigeri G. , Magni G., Raymond C. A., Russell C. T., and Turrini D. 2012. Detection of widespread hydrated materials on Vesta by the VIR imaging spectrometer on board the Dawn mission. *The Astrophysical Journal Letters 758:*L36 (5pp).

Downes H., Mittlefehldt D. W., Kita N. T., and Valley J. W. 2008. Evidence from polymict ureilites for a disrupted and re-accreted single ureilite parent asteroid gardened by several distinct impactors. *Geochimica et Cosmochimica Acta* 72:4825–4844.

Dunn T. L., Gross J., Ivanova M. A., Runyon S. E., and Bruck A. M. 2016. Magnetite in the unequilibrated CK chondrites: Implications for metamorphism and new insights into the relationship between the CV and CK chondrites. *Meteoritics & Planetary Science* 51:1701-1720.

Ehlers K. and El Goresy A. 1988. Normal and reverse zoning in niningerite: a novel key parameter to the thermal histories of EH-chondrites. *Geochimica et Cosmochimica Acta* 52:877-887.

El Goresy A., Yabuki H., Ehlers K., Woolum D., and Pernicka E. 1988. Qingzhen and Yamato-691: a tentative alphabet for the EH chondrites. *Proceedings of the National Institute for Polar Research Symposium on Antarctic Meteorites* 1:65-101.

Endress M. and Bischoff A. 1996. Carbonates in CI chondrites: Clues to parent body evolution. *Geochimica et Cosmochimica Acta* 60:489-507.

Farmer V. C. 1974. The infrared spectra of minerals. London: Mineralogical Society.

Fioretti A. M., Goodrich C. A., Shaddad M., Jenniskens P., Zolensky M., Kohl I., Young E., Rumble D., Kita N., Hiroi T., Turrin B., and Herzog G. 2017. A report on 63 newly sampled stones of the Almahata Sitta fall (asteroid 2008 TC_3) from the University of Khartoum collection, including a C2 carbonaceous chondrite (abstract #1846). 48th Lunar and Planetary Science Conference.

Fleet M. 2003. Rock forming minerals. Volume 3A. Sheet Silicates: Micas. Second Edition. London: The Geological Society, 758p.

Folinsbee K., Douglas J. A. V., and Maxwell J. A. 1967. Revelstoke, a new Type I carbonaceous chondrite. *Geochimica et Cosmochimica Acta* 31:1625-1635.

Frank D. R., Zolensky M. E., and Le L. 2014. Olivine in terminal particles of Stardust aerogel tracks and analogous grains in chondrite matrix. *Geochimica et Cosmochimica Acta* 142:240-259.

Fredriksson K. and Kerridge J. F. 1988. Carbonates and sulfates in CI chondrites: Formation by aqueous activity on the parent body. *Meteoritics* 23:35-44.

Gardner-Vandy K. G., Lauretta D. S., Greenwood R. C., McCoy T. J., and Killgore M. 2012. The Tafassasset primitive achondrite: Insights into initial stages of planetary differentiation. *Geochimica et Cosmochimica Acta* 85:142-159.

Gardner-Vandy K. G., Lauretta D. S., and McCoy T. J. 2013. A petrologic, thermodynamic and experimental study of brachinites: Partial melt residues of an R chondrite-like precursor. *Geochimica et Cosmochimica Acta* 122:36-57.

Gayon-Markt J., Delbo M., Morbidelli A., and Marchi S. 2012. On the origin of the Almahata Sitta meteorite and 2008 TC_3 asteroid. *Monthly Notices of the Royal Astronomical Society* 424:508–518.

Göbel R., Ott U., and Begemann F. 1978. On trapped noble gases in ureilites. *Journal of Geophysical Research* 83:855-867.

Goldstein J. I., Huss G. R., and Scott E. R. D. 2017. Ion microprobe analyses of carbon in Fe-Ni metal in iron meteorites and mesosiderites. *Geochimica et Cosmochimica Acta* 200:367-407.

Gooding J. L. and Keil K. 1981. Relative abundances of chondrule primary textural types in ordinary chondrites and their bearing on conditions of chondrule formation. *Meteoritics* 16:17-43.

Goodrich C. A. 1999. Are ureilites residues from partial melting of chondritic materials? The answer from MAGPOX. *Meteoritics & Planetary Science* 34:109-117.

Goodrich C. A. and Righter K. 2000. Petrology of unique achondrite Queen Alexandra Range 93148: A piece of the pallasite (howardite-eucrite-diogenite?) parent body? *Meteoritics & Planetary Science* 35:521-535.

Goodrich C. A. and Wilson L. 2014. Feldspathic clast populations in polymict ureilites: determining the compositions of melts and the mode of melt extraction on the ureilite parent body (abstract #1342). 45th Lunar and Planetary Science Conference.

Goodrich C. A., Jones J. H., and Berkley J. L. 1987. Origin and evolution of the ureilite parent magmas: multi-stage igneous activity on a large parent body. *Geochimica et Cosmochimica Acta* **51**, 2255-2274.

Goodrich C. A., Fioretti A. M., Tribaudino M., and Molin G. 2001. Primary trapped melt inclusions in olivine in the olivine-augite-orthopyroxene ureilite Hughes 009. *Geochimica et Cosmochimica Acta* 65:621-652.

Goodrich C. A., Scott E. R. D., and Fioretti A. M. 2004. Ureilitic breccias: clues to the petrologic structure and impact disruption of the ureilite parent body. *Chemie der Erde* 64:283–327.

Goodrich C. A., Wlotzka F., Ross D. K., and Bartoschewicz R. 2006. NWA 1500: Plagioclase-bearing monomict ureilite or ungrouped achondrite? *Meteoritics & Planetary Science* 41:925-952.

Goodrich C. A., Fioretti A. M., and Van Orman J. A. 2009. Petrogenesis of augite-bearing ureilites Hughes 009 and FRO 90054/93008 inferred from melt inclusions. *Geochimica et Cosmochimica Acta* 73:3055-3076.

Goodrich C. A. , Hutcheon I. D., Kita N. T., Huss G. R., Cohen B. A. and Keil K. 2010. ^{53}Mn-^{53}Cr and ^{26}Al-^{26}Mg ages of a feldspathic lithology in polymict ureilites. *Earth and Planetary Science Letters* 295:531-540.

Goodrich C. A., Kita N. T., Spicuzza M. K., Valley J. W., Zipfel J., Mikouchi T. and Miyamoto M. 2011. The Northwest Africa 1500 meteorite: Not a ureilite, maybe a brachinite. *Meteoritics & Planetary Science* 45:1906-1928.

Goodrich C. A., Sutton S. R., Wirick S., and Jercinovic M. J. 2013a. Chromium valences in ureilite olivine and implications for ureilite petrogenesis. *Geochimica et Cosmochimica Acta* 122:280-305.

Goodrich C. A., Ash R. D., Van Orman J. A., Domanik K. and McDonough W. F. 2013b. Metallic phases and siderophile elements in main group ureilites: Implications for ureilite petrogenesis. *Geochimica et Cosmochimica Acta* 112**:**340-373.

Goodrich C. A., Harlow G., Van Orman J. A., Sutton S. R. Jercinovic M. J. and Mikouchi T. 2014. Petrology of chromite in ureilites: Deconvolution of primary oxidation states and secondary reduction processes. *Geochimica et Cosmochimica Acta* 135:126-169.

Goodrich C. A., Hartmann W. K., O'Brien D. P., Weidenschilling S., Wilson L., Michel P., and Jutzi M. 2015a. Origin and history of ureilitic material in the solar system: the view from

asteroid 2008 TC_3 and the Almahata Sitta meteorite. *Meteoritics & Planetary Science* 50:782-809.

Goodrich C. A., Fioretti A. M., O'Brien D. P., Zolensky M., Jenniskens P., and Shaddad M. H. 2015b. Comparing the foreign clast populations of Almahata Sitta and typical polymict ureilites, with implications (abstract #5018). 78th Annual Meeting of the Meteoritical Society.

Goodrich C. A., Mikouchi T., and Treiman A. H. 2015c. A volcanic (quenched) angrite clast in polymict ureilite DaG 319 (abstract #5048). 78th Annual Meeting of the Meteoritical Society.

Goodrich C. A., Treiman A. H., Kita N. T., and Defouilloy C. 2016. Increasing diversity of ordinary chondrite and Rumuruti-type chondrites clasts in polymict ureilites (abstract #1617). 47th Lunar and Planetary Science Conference.

Goodrich C. A., Fioretti A. M., Zolensky M., Fries M., Shaddad M., Kohl I., Young E., and Jenniskens P. 2017a. A breccia of ureilitic and C2 carbonaceous chondrite materials from Almahata Sitta: Implications for the regolith of ureilitic asteroids (abstract #6214). 80th Annual Meeting of the Meteoritical Society.

Goodrich C. A., Treiman A. H. and Boyle S. 2017b. Melt formation and evolution on the ureilite parent body, as shown by feldspathic clasts in polymict ureilites (abstract #1196). 48th Lunar and Planetary Science Conference.

Goodrich C. A., Kita N. T., Yin Q-Z., Sanborn M. E., Williams C. D., Nakashima D., Lane M. D., and Boyle S. 2017c. Petrogenesis and provenance of ungrouped achondrite Northwest Africa 7325 from petrology, trace elements, oxygen, chromium and titanium isotopes, and mid-IR spectroscopy. *Geochimica et Cosmochimica Acta* 203:381-403.

Goodrich C. A., Ross D. K., and Treiman A. H. 2017d. A new type of foreign clast in a polymict ureilite: a CAI or Al-rich chondrule (abstract #1101). 48th Lunar and Planetary Science Conference.

Goodrich C. A., Kita N. T., Sutton S. R., Wirick S., and Gross J. 2017d. The Miller Range 090340 and 090206 meteorites: New brachinite-like achondrites with implications for the diversity and petrogenesis of the brachinite clan. *Meteoritics & Planetary Science* 52:949-978.

Goodrich C. A., Fioretti A. M., Zolensky M., Shaddad M., Ross D. K., Kohl I., Young E., Kita N., Hiroi T., Śliwiński M. G., and Jenniskens P. 2018. The Almahata Sitta polymict ureilite from the University of Khartoum collection: Classification, distribution of clast types in the

strewn field, new meteorite types, and implications for the structure of asteroid 2008 TC_3 (abstract #1321). 49th Lunar and Planetary Science Conference.

Goodrich C.A., Zolensky M., Kohl I., Young E. D., Yin Q. –Z., Sanborn M. E., and Shaddad M. H. 2019a. Carbonaceous chondrite-like xenoliths in polymict ureilites: A large variety of unique outer solar system materials (abstract #1312). 50th Lunar and Planetary Science Conference.

Goodrich C.A., Kita N. T., Zolensky M., and Shaddad M. H. 2019b. Oxygen isotope compositions of magnetite in CC-like clasts from Almahata Sitta and other polymict ureilites (abstract #1551). 50th Lunar and Planetary Science Conference.

Gounelle M., Zolensky M. E., Liou J. –C., Bland P. A., and Alard O. 2003. Mineralogy of carbonaceous chondritic microclasts in howardites: Identification of C2 fossil micrometeorites. *Geochimica et Cosmochimica Acta* 67:507-527.

Grasa G., Martínez I., Diego M., Abanades J. 2014. Determination of CaO carbonation kinetics under recarbonation conditions. *Energy Fuels* 28: 4033-4042.

Green H. W., Radcliffe S. V., and Heuer A. H. 1971. Allende meteorite: A high voltage electron petrographic study. *Science* 172:936-939.

Greenwood R. C., Franchi I. A., Kearsley A. T., and Alard O. 2010. The relationship between CK and CV chondrites. *Geochimica et Cosmochimica Acta* 74:1684-1705.

Greshake A. 2014. A strongly hydrated microclast in the Rumuruti chondrite NWA 6828: Implications for the distribution of hydrous material in the solar system. *Meteoritics & Planetary Science* 49:824-841.

Hamilton V. E. 2018. Spectral classification of ungrouped carbonaceous chondrites I: Data collection and processing (abstract #1759). 49th Lunar and Planetary Science Conference.

Hamilton V. E. and Connolly Jr., H. C. 2012. In situ microspectroscopy of a Type B CAI in Allende: Mineral identification in petrographic context (abstract #2495). 43rd Lunar and Planetary Science Conference.

Hamilton V. E., Abreu N. M., Bland P. A., Connolly H. C., Jr., Hanna R. D., Lauretta D. S., and Schrader D. L. 2018. Spectral classification of ungrouped carbonaceous chondrites II: Parameters and comparison to independent measures (abstract #1753). 49th Lunar and Planetary Science Conference.

Hamilton V. E. and Ruff S. W. 2012. Distribution and characteristics of Adirondack-class basalt as observed by Mini-TES in Gusev crater, Mars and its possible volcanic source. *Icarus* 218:917-949.

Harju E. R., Rubin A. E., Ahn I., Choi B-G., Ziegler K., and Wasson J. T. 2014. Progressive aqueous alteration of CR carbonaceous chondrites. *Geochimica et Cosmochimica Acta* 139:267-292.

Hartmann W. K., Goodrich C. A., O'Brien D. P., Michel P., Weidenschilling S. J., and Sykes M. V. 2011. Breakup and reassembly of the ureilite parent body, formation of 2008 TC_3/Almahata Sitta, and delivery of ureilites to Earth (abstract #1360). 42nd Lunar and Planetary Science Conference. CD-ROM.

Hayes J. M. 1967. Organic constituents of meteorites – a review. *Geochimica et Cosmochimica Acta* 31:1395-1440.

Heber V. S., Wieler R., Baur H., Olinger C., Friedmann T. A., and Burnett D. S. 2009. Noble gas composition of the solar wind as collected by the Genesis mission. *Geochimica et Cosmochimica Acta* 73:7414-7432.

Herrin J. S., Zolensky M. E., Ito M., Le L., Mittlefehldt D. W., Jenniskens P., Ross A. J., and Shaddad M. H. 2010. Thermal and fragmentation history of ureilitic asteroids: insights from the Almahata Sitta fall. *Meteoritics & Planetary Science* 45:1789–1803.

Herrin J. S., Zolensky M. E., Cartwright J. A., Mittlefehldt D. W., and Ross D. K. 2011. Carbonaceous chondrite-rich howardites: The potential for hydrous lithologies on the HED parent (abstract #2806). 42nd Lunar and Planetary Science Conference.

Hildebrand A. R., McCausland P. J. A., Brown P. G., Longstaffe F. J., Russell S. D. J., Tagliaferri E., Wacker J. F., and Mazur M. J. 2006. The fall and recovery of the Tagish Lake meteorite. *Meteoritics & Planetary Science* 41:407-431.

Hiroi T., Jenniskens P., Bishop J. L., Shatir T. S. M., Kudoda A. M., and Shaddad M. H. 2010. Bi-directional visible-NIR and biconical FT-IR reflectance spectra of Almahata Sitta meteorite samples. *Meteoritics & Planetary Science* 45:1836-1845.

Hiroi T., Milliken R. E., Pieters C. M., Kaiden H., Imae N., Yamaguchi A., Kojima H., Sasaki S., Matsuoka M., Sato Y., and Nakamura T. 2017. Visible and near-infrared spectral survey of carbonaceous chondrites and its application to HAYABUSA 2 (abstract #1086). 48th Lunar and Planetary Science Conference.

Horstmann M. and Bischoff A. 2014. The Almahata Sitta polymict breccia and the late accretion of asteroid 2008 TC_3. *Chemie der Erde* 74:149-183.

Horstmann M., Humayun M., and Bischoff A. 2014. Clues to the origin of metal in Almahata Sitta EL and EH chondrites and implications for primitive E chondrite thermal histories. *Geochimica et Cosmochimica Acta* 140:720-744.

Howard K. T., Alexander C. M. O. D., Schrader D. L., and Dyl K. A. 2015. Classification of hydrous meteorites (CR, CM and C2 ungrouped) by phyllosilicate fraction: PSD-XRD modal mineralogy and planetesimal environments. *Geochimica et Cosmochimica Acta* 149:206–222.

Huss G. R. and Lewis R. S. 1994. Noble gases in presolar diamonds I: Three distinct components and their implications for diamond origins. *Meteoritics* 29:791-810.

Huss G. R. and Lewis R. S. 1995. Presolar diamond, SiC, and graphite in primitive chondrites: Abundances as a function of meteorite class and petrologic type. *Geochimica et Cosmochimica Acta* 59:115-160.

Ikeda Y. 1983. Alteration of chondrules and matrices in the four Antarctic carbonaceous chondrites ALH-77307(C3), Y-790123(C2), Y-75293(C2), and Y-74662(C2). *Proceedings of the National Institute of Polar Research Special Issue* 30:93-108.

Ikeda Y., Prinz M., and Nehru C. E. 2000. Lithic and mineral clasts in the Dar al Gani (DaG) 319 polymict ureilite. *Antarctic Meteorite Research* 13:177–221.

Ikeda Y., Kita N. T., Morishita Y., and Weisberg M. K. 2003. Primitive clasts in the Dar al Gani 319 polymict ureilite: precursors of the ureilites. *Antarctic Meteorite Research* 16:105–127.

Inoue M., Mikouchi T., and Goodrich C. A. 2016. Petrography and mineralogy of Northwest Africa 3222: Magmatically zoned augite-bearing ureilite with only little carbon (abstract #6417). 79th Annual Meeting of the Meteoritical Society.

Jaques A. L. and Fitzgerald M. J. 1982. The Nilpena ureilite, an unusual polymict breccia: Implications for origin. *Geochimica et Cosmochimica Acta* 46:893-900.

Jenniskens P., Shaddad M. H., Numan D., Elsir S., Kudoda A. M., Zolensky M. E., Le L., Robinson G. A., Friedrich J. M., Rumble D., Steele A., Chesley S. R., Fitzsimmons A., Duddy S., Hsieh H. H., Ramsay G., Brown P. G., Edwards W. N., Tagliaferri E., Boslough M. B., Spalding R. E., Dantowitz R., Kozubal M., Pravec P., Borovička J., Charvát Z., Vaubaillon J., Kuiper J., Albers J., Bishop J., Mancinelli R. L., Sandford S. A., Milam S. N.,

Nuevo M., and Worden S. P. 2009. The impact and recovery of asteroid 2008 TC_3. *Nature* 458:485–488.

Jenniskens P., Vaubaillon J., Binzel R. P., Demeo F. E., Desvorný D., Bottke W. F., Fitzsimmons A., Hiroi T., Marchis F., Bishop J. L., Vernazza P., Zolensky M. E., Herrin J. S., Welten K. C., Meier M. M. M., and Shaddad M. H. 2010. Almahata Sitta (=asteroid 2008 TC_3) and the search for the ureilite parent body. *Meteoritics & Planetary Science* 45:1590–1617.

Johnson C. A. and Prinz M. 1993. Carbonate compositions in CM and CI chondrites and implications for aqueous alteration. *Geochimica et Cosmochimica Acta* 57*:2843-2852.*

Jones R. H. 2012. Petrographic constraints on the diversity of chondrule reservoirs in the protoplanetary disk. *Meteoritics & Planetary Science* 47:1176-1190.

Kallemeyn G. W., Rubin A. E., Wang D., and Wasson J. T. 1989. Ordinary chondrites: Bulk compositions, classification, lithophile-element fractionations, and composition-petrographic type relationships. *Geochimica et Cosmochimica Acta* 53:2747-2767.

Keller L. P., Thomas K. L., Clayton R. N., Mayeda T. K., DeHart J. M., and McKay D. S. 1994. Aqueous alteration of the Bali CV3 chondrite: Evidence from mineralogy, mineral chemistry, and oxygen isotopic compositions. *Geochimica et Cosmochimica Acta* 58:5589-5598.

Kerridge J. F. 1985. Carbon, hydrogen and nitrogen in carbonaceous chondrites: abundances and isotopic compositions in bulk samples. *Geochimica et Cosmochimica Acta* 49:1701-1714.

Kimura M., Tsuchiyama A., Fukuoka T., and Iimura Y. 1992. Antarctic primitive achondrites Yamato-74025, -75300, and 75305: Their mineralogy, thermal history, and the relevance to winonaite. *Proceedings, National Institute of Polar Research Symposium on Antarctic Meteorites* 5:165-190.

Kita N. T., Ikeda Y., Togashi S., Liu Y., Morishita Y., and Weisberg M. K. 2004. Origin of ureilites inferred from a SIMS oxygen isotopic and trace element study of clasts in the Dar al Gani 319 polymict ureilite. *Geochimica et Cosmochimica Acta* 68:4213-4235.

Kita N. T., Goodrich C. A., Fu B., Spicuzza M. J., and Valley J. W. 2006. Oxygen isotopes in mafic and feldspathic clasts from polymict ureilites (abstract #5161). 69th Annual Meeting of the Meteoritical Society. *Meteoritics & Planetary Science* 41 (Suppl):A96.

Kita N. T., Nagahara H., Tachibana S., Tomomura S., Spicuzza M. J., Fournelle J. H., and Valley J.W. 2010. High precision SIMS oxygen three isotope study of chondrules in LL3

chondrites: Role of ambient gas during chondrule formation. *Geochimica et Cosmochimica Acta* 74:6610-6635.

Kita N. T., Defouilloy C., Goodrich C. A., and Zolensky M. E. 2017. Oxygen isotope ratios of magnetite in CI-like clasts from a polymict ureilite (abstract #6153). 80th Annual Meeting of the Meteoritical Society.

Klimentidis R. and MacKinnon I. D. R. 1986. High resolution imaging of ordered mixed-layer clays. *Clays and Clay Minerals* 34:155-164.

Kojima H., Ikeda Y., and Yanai K. 1984. The alteration of chondrules and matrices in new Antarctic carbonaceous chondrites. *Proceedings 9th Symposium on Antarctic Meteorites, NIPR Special Issue* 35:184-199.

Kornacki A. S. and Wood J. A. 1984. The mineral chemistry and origin of inclusion matrix and meteorite matrix in the Allende CV3 chondrite. *Geochimica et Cosmochimica Acta* 48:1663-1676.

Kowalski R. A. et al. in MPEC 2008-T50 (ed. Williams, G.V.) 1-1 (Minor Planet Center, Smithsonian Astrophysical Observatory, 2008).

Kozubal M. J., Gasdia F. W., Dantowitz R. F., Scheirich P., and Harris A. W. 2011. Photometric observations of Earth-impacting asteroid 2008 TC_3. *Meteoritics & Planetary Science* 46: 534-542.

Kunihiro T., Rubin A. E., McKeegan K. D., and Wasson J. T. 2004. Oxygen-isotopic compositions of relict and host grains in chondrules in the Yamato 81020 CO3.0 chondrite. *Geochimica et Cosmochimica Acta* 68:3599-3606.

Krot A. N., Scott E. R. D., and Zolensky M. E. 1995. Mineralogical and chemical modification of components in CV3 chondrites: Nebular or asteroidal processing? *Meteoritics* 30:748-775.

Lane M. D. and Christensen P. R. 1997. Thermal infrared emission spectroscopy of anhydrous carbonates. *Journal of Geophysical Research* 102:25,581-25,592.

Lane M. D., Glotch T. D., Dyar M. D., Pieters C. M., Klima R., Hiroi T., Bishop J. L. and Sunshine J. 2011. Mid-infrared spectroscopy of synthetic olivines: Thermal emission, specular and diffuse reflectance, and attenuated total reflectance studies of forsterite to fayalite. *Journal of Geophysical Research* 116, doi:10.1029/2010JE003588.

Le Guillou C., Changela H. G., and Brearley A. J. 2015. Widespread oxidized and hydrated amorphous silicates in CR chondrites matrices: Implications for alteration conditions and H_2 degassing of asteroids. *Earth and Planetary Science Letters* 420: 162-173.

Leshin L. A., Rubin A. E., and McKeegan K. D. 1997. The oxygen isotopic composition of olivine and pyroxene from CI chondrites. *Geochimica et Cosmochimica Acta* 61:835-845.

Leya I. and Masarik J. 2009. Cosmogenic nuclides in stony irons revisited. *Meteoritics & Planetary Science* 44:1061-1086.

Löhn B. and El Goresy A. 1992. Morphologies and chemical composition of individual magnetite grains in CI and CM chondrites: A potential genetic link to their origin? *Meteoritics* 27:252.

Macke R. J., Consolmagno G. J., and Britt D. T. 2011a. Density, porosity, and magnetic susceptibility of carbonaceous chondrites. *Meteoritics & Planetary Science* 46:1842-1862.

Macke R. J., Britt D. T., and Consolmagno G. J. 2011b. Density, porosity, and magnetic susceptibility of achondritic meteorites. *Meteoritics & Planetary Science* 46:311-326.

MacKinnon I. D. R. 1980. Structures and textures of the Murchison and Mighei carbonaceous chondrite matrices. Proceedings of the 11th Lunar and Planetary Science Conference. pp. 839-852.

MacKinnon I. D. R. 1982. Ordered mixed-layer structures in the Mighei carbonaceous chondrite matrix. *Geochimica et Cosmochimica Acta* 46:479-489.

Mainzer A., Grav T., Masiero J., Hand E., Bauer J., Tholen D., McMillan R. S., Spahr T., Cutri R. M., Wright E., Watkins J., Mo W., and Maleszewski C. 2011. Neowise studies of spectrophotometrically classified asteroids: preliminary results. *Astrophysical Journal* 741: 90 (25 pp).

McKay D. S., Swindle T. D. and Greenberg R. 1989. Asteroidal regoliths: What we do not know. In *Asteroids II*, edited by Binzel R. P. Tucson: University of Arizona Press. pp. 617-642.

McSween H. Y., Jr. 1979. Alteration in CM carbonaceous chondrites inferred from modal and chemical variations in matrix. *Geochimica et Cosmochimica Acta* 43:1761-1770.

Meier M. M., Welten K. C., Caffee M. W., Friedrich J. M., Jenniskens P., Nishiizumi K., Shaddad M. H., and Wieler R. 2012. A noble gas and cosmogenic radionuclide analysis of two ordinary chondrites from Almahata Sitta. *Meteoritics & Planetary Science* 47:1075–1086.

Michalski J. R., Kraft M. D., Sharp T. G., Williams L. B., and Christensen P. R. 2006. Emission spectroscopy of clay minerals and evidence for poorly crystalline aluminosilicates on Mars from Thermal Emission Spectrometer data. *Journal of Geophysical Research* 11:DOI:10.1029/2005JE002438.

Michel P., Benz W., Tanga P., and Richardson D. C. 2001. Collisions and gravitational reaccumulation: Forming asteroid families and satellites. *Science* 294:1696-1700.

Michel P., Jutzi M., Richardson D. C., Goodrich C. A., Hartmann W. K., and O'Brien D. P. 2015. Selective sampling during catastrophic disruption: mapping the location of reaccumulated fragments in the original parent body. Proceedings of the 8th Catastrophic Disruption Workshop. *Planetary and Space Science* 107:24-28.

Mittlefehldt D. W., Lindstrom M. M., Bogard D. D., Garrison D. H., and Field S. W. 1996. Acapulco- and Lodran-like achondrites: Petrology, geochemistry, chronology, and origin. *Geochimica et Cosmochimica Acta* 60:867-882.

Mittlefehldt D. W., McCoy T. J., Goodrich C. A., and Kracher A. 1998. Non-chondritic meteorites from asteroidal bodies. In *Planetary Materials*, edited by Papike J. J. Washington, D.C.: Mineralogical Society of America. pp. 4-1 to 4-195.

Mittlefehldt D. W., Bogard D. D., Berkley J. L., and Garrison D. H. 2003. Brachinites: Igneous rocks from a differentiated asteroid. *Meteoritics & Planetary Science* 38:1601-1625.

Müller W. F., Kurat G., and Kracher A. 1977. Crystal structure and composition of cronstedtite from the Cochabamba carbonaceous chondrite. *Meteoritics* 12:322 (abstract).

Murty S.V.S., Mahajan R. R., Jenniskens P., Shaddad M. H., and Eldien B. 2010. Noble gases and nitrogen in the Almahata Sitta ureilite. *Meteoritics & Planetary Science* 45:1751-1764.

Nagahara H. 1992. Yamato-8002: Partial melting residue on the “unique” chondrite parent body. *Proceedings of the NIPR Symposium on Antarctic Meteorites* 5:191-223.

Nagao K., Haba M. K., Zolensky M., Jenniskens P and Shaddad M. H. 2014. Noble gases in two fragments of different lithologies from the Almahata Sitta meteorite (abstract #5204). 77th Annual Meeting of the Meteoritical Society.

Nakamura T. 2005. Post-hydration thermal metamorphism of carbonaceous chondrites. *Journal of Mineralogical and Petrological Sciences* 100:260-272.

Nehru C. E., Prinz M., and Delaney J. S. 1983. Brachina: A new type of meteorite, not a chassignite. Proceedings, 14th Lunar and Planetary Science Conference, Part 1. *Journal of Geophysical Research* 88:B237-B244.

Ott U. 2014. Planetary and pre-solar noble gases in meteorites. *Chemie der Erde* 74:519–544.

Ott U., Löhr H. P., and Begemann F. 1985. Trapped neon in ureilites - a new component. In Isotopic ratios in the solar system. Tolouse, France: CEPA DUES-EDITIONS. pp. 129-136.

Ott U. , Löhr H. P., and Begemann F. 1990. EET 83309: A ureilite with solar noble gases. *Meteoritics* 25: 396.

Ott U., Hermann S., Jenniskens P. M., and Shaddad M. 2010. A noble gas study of two stones from the Almahata Sitta meteorite (abstract #1195). 41st Lunar and Planetary Science Conference.

Papike J. J., Spilde M. N., Fowler G. W., Layne G. D., and Shearer C. K. 1995. The Lodran primitive achondrite: Petrogenetic insights from electron and ion microprobe analysis of olivine and orthopyroxene. *Geochimica et Cosmochimica Acta* 59:3051-3070.

Patzek M., Hoppe P., Bischoff A., Visser R., and John T. 2017. Water-bearing, volatile-rich clasts in howardites and polymict ureilites – Carriers of deuterium-enriched waters not sampled by individual meteorites (abstract #6183). 80th Annual Meeting of the Meteoritical Society.

Patzek M., Bischoff A., Visser R., and John T. 2018a. Mineralogy of volatile-rich clasts in brecciated meteorites. *Meteoritics & Planetary Science* 53:2519-2540.

Patzek M., Pack A., Bischoff A., Visser R., and John T. 2018b. O-isotope composition of CI- and CM-like clasts in ureilites, HEDs, and CR chondrites (abstract #6254). 81st Annual Meeting of the Meteoritical Society.

Pearson V. K., Sephton M. A., Franchi I. A., Gibson J. M., and Gilmour I. 2006. Carbon and nitrogen in carbonaceous chondrites: Elemental abundances and stable isotopic compositions. *Meteoritics & Planetary Science* 41:1899-1918.

Peck J. A. 1984. Origin of the variation in properties of CV3 meteorite matrix and matrix clasts. In *Lunar and Planetary Science XV*, pp. 635-636. Lunar and Planetary Institute, Houston.

Petaev M. I., Barsukova L. D., Lipschutz M. E., Wang M. –S., Ariskin A. A., Clayton R. N., and Mayeda T. K. 1994. The Divnoe meteorite: Petrology, chemistry, oxygen isotopes and origin. *Meteoritics* 29:182-199.

Popova O., Borovička J., Hartmann W. K., Spurný P., Gnos E., Nemtchinov I., and Trigo-Rodríguez J. M. 2011. Very low strengths of interplanetary meteoroids and small asteroids. *Meteoritics & Planetary Science* 46:1525-1550.

Prinz M., Weisberg M. K., Nehru C. E., and Delaney J. S. 1986. North Haig and Nilpena: paired polymict ureilites with Angra dos Reis-related and other clasts. In *Lunar and Planetary Science XVII*, pp. 681-682.

Prinz M., Weisberg M. K., Nehru C. E., and Delaney J. S. 1987. Black inclusions of carbonaceous chondrite matrix material in polymict ureilites. *Meteoritics* 22:482-483.

Prinz M., Weisberg M. K., and Nehru C. E. 1988. Feldspathic components in polymict ureilites. In *Lunar and Planetary Science XIX,* pp. 947-948.

Rai V. K., Murty V. S., and Ott U. 2003. Noble gases in ureilites: cosmogenic, radiogenic, and trapped components. *Geochimica et Cosmochimica Acta* 67:4435-4456.

Reddy V., Le Corre L., O'Brien D. P., Nathues A., Cloutis E. A., Durda D. D., Bottke W. F., Bhatt M. U., Nesvorny D., Buczkowski D., Scully J. E. C., Palmer E. M., Sierk H., Mann P. J., Becker K. J., Beck, A.W., Mittlefehldt D., Li J.-Y., Gaskell R., Russell C. T., Gaffey M. J., McSween H. Y., McCord T. B., and Blewett D. 2012. Delivery of dark material to Vesta via carbonaceous chondritic impacts. *Icarus* 221:544–559.

Reddy V., Shephard M. K., Takir D., Sanchez J. A., Richardson J., Emery J. P., and Taylor P. A. 2017. Psyche: state of knowledge from ground-based observations (abstract #6335). 80th Annual Meeting of the Meteoritical Society.

Reisener R. J. and Goldstein J. I. 2003. Ordinary chondrite metallography: Part 2. Formation of zoned and unzoned metal particles in relatively unshocked H, L, and LL chondrites. *Meteoritics & Planetary Science* 38:1679-1696.

Riebe M. E. I. , Welten K. C., Meier M. M. M., Wieler R., Barth M. U. F., Ward D., Laubenstein M., Bischoff A., Caffee M. W., Nishiizumi K., and Busemann H. 2017a. Cosmic-ray exposure ages of six chondritic Almahata Sitta fragments. *Meteoritics & Planetary Science* 52, 2353-2374.

Riebe M. E. I., Busemann H., Wieler R., and Maden C. 2017b. Closed System Step Etching of CI chondrite Ivuna reveals primordial noble gases in the HF-solubles. *Geochimica et Cosmochimica Acta* 205:65-83.

Rivkin A. S., Campins H., Emery J. P., Howell E. S., Licandro J., Takir D., and Vilas F. 2015. Astronomical observations of volatiles on asteroids. *In* Asteroids IV, edited by Michel P., DeMeo R.E. and Bottke W.F. Tucson: The University of Arizona Press. pp. 65-88.

Rivkin A.S. (2012) The fraction of hydrated C-complex asteroids in the asteroid belt from SDSS data. *Icarus* 221(2):327-333.

Rodriguez-Navarro C., Ruiz-Agudo E., Luque A., Rodriguez-Navarro A., and Ortega-Huertas M. 2009. Thermal decomposition of calcite: Mechanisms of formation and textural evolution of CaO nanocrystals. *American Mineralogist* 94:578–593.

Ross A. J., Downes H., Smith C. L., and Jones A. P. 2010. DaG 1047: A polymict ureilite containing exotic clasts including a chondrite (abstract #2361). 41st Lunar and Planetary Science Conference.

Ross A. J., Steele A., Fries M. D., Kather L., Downes H., Jones A. P., Smith C. L., Jenniskens P. M., Zolensky M. E., and Shaddad M. H. 2011 MicroRaman spectroscopy of diamond and graphite in Almahata Sitta and comparison with other ureilties. *Meteoritics & Planetary Science* 46:364-378.

Rout S. S., Heck P. R., Isheim D., Stephan T., Zaluzec N. J., Miller D. J., Davis A. M., and Seidman D. N. 2017. Atom-probe tomography and transmission electron microscopy of the kamacite-taenite interface in the fast-cooled Bristol IVA iron meteorite. *Meteoritics & Planetary Science* 52:2707-2729.

Rubin A. E. 1990. Kamacite and olivine in ordinary chondrites: Intergroup and intragroup relationships. *Geochimica et Cosmochimica Acta* 54:1217-1232.

Sanborn M. E., Yin Q.-Z., Goodrich C. A., Zolensky M., and Fioretti A. M. 2017. A case for nebula scale mixing between non-carbonaceous and carbonaceous chondrite reservoirs: Testing the Grand Tack model with chromium isotopic composition of Almahata Sitta stone 91A (abstract #6277). 80th Annual Meeting of the Meteoritical Society.

Scheirich P., Ďurech., Pravec P., Kozubal M., Dantowitz R., Kaasalainen M., Betzler A. S., Meltrame P., Muler G., Birtwhistle P., and Kugel F. 2010. The shape and rotation of asteroid 2008 TC_3. *Meteoritics & Planetary Science* 45**:**1804–1811.

Scott E. R. D. and Krot A. N. 2004. Chondrites and their components, pp. 143-200, In *Meteorites, Comets, and Planets* (ed. A.M. Davis) Vol. 1 *Treatise on Geochemistry* (eds. H.D. Holland and K.K. Turekian), Elsevier-Pergamon, Oxford.

Scott E. R. D., Krot A. N., and Sanders I. S. 2018. Isotopic dichotomy among meteorites and its bearing on the protoplanetary disk. *The Astrophysical Journal* 854:164 (12 pp).

Shaddad M. H., Jenniskens P., Numan D., Kudoda A. M., Elsir S., Riyah I. F., Ali A. E., Alameen M., Alameen N. M., Eid O., Osman A.T., AbuBaker M. I., Yousif M., Chesley S. R., Chodas P. W., Albers J., Edwards W. N., Brown P. G., Kuiper J., and Friedrich J.M. 2010. The recovery of asteroid 2008 TC_3. *Meteoritics & Planetary Science* 45:1618–1637.

Singletary S. J. and Grove T. L. 2003. Early petrologic processes on the ureilite parent body. *Meteoritics & Planetary Science.* 3895-108.

Smith P. P. K. and Buseck P. R. 1981. Graphitic carbon in the Allende meteorite, a microstructural study. *Science* 212:323-342.

Steele I. M. 1990. Minor elements in forsterites of Orgueil (C1), Alais (C1 and two interplanetary dust particles compared to C2-C3-UOC forsterites. *Meteoritics & Planetary Science* 25:301-307.

Takeda H. 1987. Mineralogy of Antarctic ureilites and a working hypothesis for their origin and evolution. *Earth and Planetary Science Letters* 81:358-370.

Takeda H. 1989. Mineralogy of coexisting pyroxenes in magnesian ureilites and their formation conditions. *Earth and Planetary Science Letters* 93:181-194.

Takeda H., Mori H., and Ogata H. 1989. Mineralogy of augite-bearing ureilites and the origin of their chemical trends. *Meteoritics* 24:73-81.

Takeda H., Mori H., Hiroi T., and Saito J. 1994. Mineralogy of new Antarctic achondrites with affinity to Lodran and a model of their evolution in an asteroid. *Meteoritics* 29:830-842.

Takir D., Reddy V., Sanchez J. A., Shepard M. K. and Emery J. P. 2017. Detection of water and/or hydroxyl on asteroid (16) Psyche. *The Astronomical Journal* 153:31 (6 pp).

Tenner T. J., Nakashima D., Ushikubo T., Kita N. T., and Weisberg M. K. 2015. Oxygen isotope ratios of FeO-poor chondrules in CR3 chondrites: influence of dust enrichment and H_2O during chondrule formation. *Geochimica et Cosmochimica Acta* 148:228-250.

Tholen D. J. 1984. Asteroid taxonomy from cluster analysis of photometry. Ph.D. Thesis, Univ. Arizona.

Tholen D. J. and Barucci M. 1989. Asteroid taxonomy. In Asteroids II, edited by Binzel R., Gehrels T., and Matthews M. Tucson: University of Arizona Press. pp. 298–315.

Tomeoka K. and Buseck P. R. 1988. Matrix mineralogy of the Orgueil CI carbonaceous chondrite. *Geochimica et Cosmochimica Acta* 52:1627-1640.

Tonui E., Zolensky M., Hiroi T., Nakamura T., Lipschutz M., Wang M.-S., Okudaira K. 2014. Petrographic, chemical and spectroscopic evidence for thermal metamorphism in carbonaceous chondrites I: CI and CM chondrites. *Geochimica et Cosmochimica Acta* 126:284–306.

Treiman A. H. and Berkley J. L. 1994. Igneous petrology of the new ureilites Nova 001 and Nullarbor 010. *Meteoritics* 29:843-848.

Turrini D., Combe J. -P., McCord T. B., Oklay N., Vincent J. -B., Prettyman T. H., McSween H. Y., Consolmagno G. J., De Sanctis M. C., Le Corre L., Longobardo A., Palomba E., and Russell C. T. 2014. The contamination of the surface of Vesta by impacts and the delivery of the dark material. *Icarus* 240:86-102.

Ushikubo T., Kimura M., Kita N. T., and Valley J. W. 2012. Primordial oxygen isotope reservoirs of the solar nebula recorded in chondrules in Acfer 094 carbonaceous chondrite. *Geochimica et Cosmochimica Acta* 90:242-264.

Visser R., John T., Patzek M., Bischoff A., and Whitehouse M. 2018. Sulfur isotope compositions of sulfides in carbonaceous chondrites and volatile-rich, CI- and CM-like clasts from various chondrites and achondrites (abstract #6190). 81st Annual Meeting of the Meteoritical Society.

Warren P. H. and Kallemeyn G. W. 1989. Allan Hills 84025: The second brachinite, far more differentiated than Brachina, and an ultramafic achondritic clast from L chondrite Yamato 75097. Proceedings of the 19th Lunar and Planetary Science Conference. pp. 475-486.

Warren P. H. and Kallemeyn G. W. 1992. Explosive volcanism and the graphite-oxygen fugacity buffer on the parent asteroid(s) of the ureilite meteorites. *Icarus* 100:110-126.

Warren P. H. and Rubin A. E. 2011. Pyroxene-selective impact smelting in ureilites. *Geochimica et Cosmochimica Acta* 74:5109-5133.

Weber I., Bischoff A., and Weber D. 2003. TEM investigations on the monomict ureilites Jalanash and Hammadah al Hamra 064. *Meteoritics & Planetary Science* 38:145-156.

Weisberg M. K. and Kimura M. 2012. The unequilibrated enstatite chondrites. *Chemie der Erde* 72:101-115.

Welten K. C., Meier M. M. M., Caffee M. W., Nishiizumi K., Wieler R., Jenniskens P., and Shaddad M. H. 2010. Cosmogenic nuclides in Almahata Sitta ureilites: Cosmic-ray exposure age, preatmospheric mass, and bulk density of asteroid 2008 TC_3. *Meteoritics & Planetary Science* 45:1728–1742.

Wieler R. 2002. Cosmic-ray-produced noble gases in meteorites. *Reviews in Mineralogy and Geochemistry* 47:125-170.

Wieler R., Baur H., and Signer P. 1986. Noble gases from solar energetic particles revealed by closed system stepwise etching of lunar soil minerals. *Geochimica et Cosmochimica Acta* 50:1997-2017.

Wieler R., Busemann H., and Franchi I. A. 2006. Trapping and modification processes of noble gases and nitrogen in meteorites and their parent bodies. In *Meteorites and the early solar system II*, edited by Lauretta D. S. and McSween H. Y. Jr. Tucson, Arizona: The University of Arizona Press. pp. 499-521.

Wlotzka F. 1972. Haverö ureilite: Evidence for recrystallization and partial reduction. *Meteoritics* 7:591-600.

Yeomans D. 2008. NASA/JPL Near-Earth Object Program Office Statement (http://neo.jpl.nasa.gov/news/news159.html) (6October 2008).

Yin Q.-Z., Sanborn M. E., Goodrich C. A., Zolensky M., Fioretti A. M., Shaddad M., Kohl I. E., and Young E. D. 2018. Nebula scale mixing between non-carbonaceous and carbonaceous chondrite reservoirs: Testing the Grand Tack model with Almahata Sitta stones (abstract #1810). 49th Lunar and Planetary Science Conference.

Zanda B., Bourot-Denise M., Perron C., and Hewins R. H. 1994. Origin and metamorphic redistribution of silicon, chromium, and phosphorus in the metal of chondrites. *Science* 265, 1846-1849.

Zolensky M. and McSween H. Y., Jr. 1988. Aqueous Alteration. *In* Meteorites and the early solar system, edited by Kerridge J. F. and Matthews M. S. Tucson: The University of Arizona Press. pp. 114-143.

Zolensky M. E., Barrett T., and Browning L. 1993. Mineralogy and composition of matrix and chondrule rims in carbonaceous chondrites. *Geochimica et Cosmochimica Acta* 57:3123-3148.

Zolensky M. E., Weisberg M. K., Buchanan P. C., and Mittlefehldt D. W. 1996. Mineralogy of carbonaceous chondrite clasts in HED achondrites and the Moon. *Meteoritics & Planetary Science* 31:518-537.

Zolensky M., Herrin J., Mikouchi T., Ohsumi K., Friedrich J., Steele A., Rumble D., Fries M., Sandford S., Milam S., Hagiya K., Takeda H., Satake W., Kurihara T., Colbert M., Hanna R., Maisano J., Ketcham R., Goodrich C. A., Le L., Robinson G.-A., Martinez J., Ross K., Jenniskens P., and Shaddad M. 2010. Mineralogy and petrography of the Almahata Sitta ureilite. *Meteoritics & Planetary Science* 45:1618–1637.

Zolensky M., Fries M., Chan Q. H. –S., Yebukawa Y., Steel A., Bodnar R. J., Ito M., Nakashima D., Nakamura T., Greenwood R., Rahman Z., Le L., Ross D. J., Ziegler K., Bottke W., and Martinez J. 2018. Outer solar system material in inner solar system regolith breccias (abstract #6103). 81st Annual Meeting of the Meteoritical Society.

Zolotov M. Yu., Mironenko M. V., and Shock E. L. 2006. Thermodynamic constraints on fayalite formation on parent bodies of chondrites. *Meteoritics & Planetary Science* 41:1775-1796.

Figure Captions

Figure 1. Find coordinates for Almahata Sitta (AhS) stones in the University of Khartoum (UoK) collection (Shaddad et al. 2010). Classification of 85 stones from Zolensky et al. (2010) and Goodrich et al. (2018). The asteroid path was from NW to SE. The three carbonaceous chondrite (CC) stones are noted by sample number. AhS 91/91A and AhS 671 are the subject of this paper. AhS #202 was briefly described in Fioretti et al. (2017) and Goodrich et al. (2018).

Figure 2. (a) Fragment AhS 91A_11, showing the highly friable nature of this stone. Crumbs in this image were not chipped off the sample, but fell off by themselves. (b) Image from the interior of a CT scan of AhS 91A_11, showing large mineral clast (possibly ureilitic) embedded in fine-grained CC-like material.

Figure 3. Back-scattered electron images (BEI) and X-ray elemental maps of fragment AhS 91A_1. This fragment consists mostly of a C1 lithology, but contains a few small clasts of ureilitic minerals. (a) BEI of whole fragment. (b) Mg (red) – Al (green) – Ca (blue) map corresponding to [a]. (c) BEI of area 2 marked in [a,b]. sulf = (sulfide); pig = pigeonite; br = breunnerite. (d) Mg (red) – Si (green) – S (blue) – Ca (cyan) map corresponding to [c]. Pigeonite grain in [c,d] is consistent with ureilitic pigeonite compositions.

Figure 4. (a) BEI of a common type of clast in the C1 lithology of AhS 91A. Such clasts consist of laths or patches of an unidentified Ca-rich silicate phase in a matrix of serpentine (serp) and other (?) phyllosilicates, with clusters of magnetite (mgt) grains. (b) BEI showing interior of clast in area 1 of AhS 91A_1 (Fig. 3a,b). (c) Detail from lower left corner of [b]. Rectangular box indicates position of FIB section made from this area and studied by TEM. [d] Bright field TEM image of a detail from the FIB section from [c] showing a well-crystallized phyllosilicate with a 0.95-0.96 nm interlayer spacing, possibly dehydrated smectite with a composition between montmorillonite and saponite.

Figure 5. (a) BEI of phyllosilicate-rich clast in area 4 of AhS 91A_1 (Fig. 3a,b). (b) Detail of clast in [a], showing fine-grained mixture of serpentine (serp) plus other phyllosilicates. (c) Low magnification bright field TEM image of the flaky serpentine with flakes exhibiting 0.7 nm basal lattice fringes characteristic of serpentine-type phases. (d) Detail from (c) showing a few serpentine flakes, but with none showing basal lattice fringes, indicating heating and dehydration.

Figure 6. (Si+Al)–Mg–Fe atomic percent ternary diagram plotting compositions of phyllosilicates in AhS 91A and AhS 671 compared with those in selected carbonaceous chondrites (data collected in this work for CM, CI, and CR chondrites). Lines cutting through the ternary represent the observed stoichiometric compositions of serpentine and saponite (from Fleet 2003; Deer, Howie and Zussman 1962). CMs in the plot are Boriskino (96 points), Crescent (18), Santa Cruz (21), Cochabamba (51), and MET01070 (75). CIs are Alais (55 points) and Orgueil (101). The CR is Renazzo (18 points). Essebi (39) is a C2 related to CMs. Data for AhS 91A (area 4 − 76 points, other areas – 45 points), and AhS 671 (19 points). Data for all samples were obtained by line scans of analyses of matrix areas (see Supplement 2), and then filtered to remove analyses with high FeO (presumably including magnetite and/or fayalite and/or sulfides) and CaO (including Ca-rich phases), as well as those with extremely low totals.

Figure 7. Low magnification TEM bright field image of the FIB slice of area 1 in AhS 91A_1. Areas dominated by different phyllosilicate morphologies are indicated (A,B,C). Area A is dominated by poorly-crystalline, fibrous phyllosilicate. Area B consists mainly of coarse-grained phyllosilicate. Area C consists mainly of poorly-crystalline, spongy phyllosilicate. Some Fe-Ni sulfides are indicated. Possible organic nanoglobules, identified by typical morphology and EDS spectra showing carbon, are indicated.

Figure 8. Higher magnification TEM bright field images of phyllosilicate morphologies in 91A. (a-b) views of relatively well crystalline phyllosilicates from area B in Figure 7. Interlayer lattice fringes (lines from upper left to lower right) measuring 1.1 to 1.3 nm are evident in (b). (c-d) poorly crystalline, spongy phyllosilicates from area C in Figure 7. (d) shows a few, very thin phyllosilicate crystallites (arrowed), with 1.1 to 1.3 nm spacings and only 2-4 sheets thick.

Figure 9. BEI of large breunnerite grain (a) and large dolomite grain (b) in AhS 91A. Both carbonates have narrow rims of Mg-enriched breunnerite. Dolomite has inclusions of Fe,Ni sulfides. (c) Compositions of carbonates in AhS 91A and AhS 671 in the calcite-magnesite-siderite ternary system, compared with carbonates in various groups of carbonaceous chondrites. Data sources: Fredricksson and Kerridge (1988); Endress and Bischoff (1996); DE Leuw et al. (2010).

Figure 10. (a-d) BEI showing magnetite (mgt) in AhS 91A, which commonly occurs in clusters of grains having irregular rims of fayalitic olivine (fay), and less commonly in clusters with interstitial sulfide (sulf). (e) Plot of wt.% MgO vs. wt.% Al_2O_3 in magnetite in AhS 91A and AhS 671 compared with magnetite in various chondrite groups. (f) Plot of wt.% Cr_2O_3 vs. wt.% TiO_2 in magnetite in AhS 91A and AhS 671 compared with magnetite in various chondrite groups. Data for CK and CV from Dunn et al. (2016) and Greenwood et al. (2010); CR from Harju et al. (2014); CC clasts in typical polymict ureilites from Brearley and Prinz (1992) and Goodrich et al. (2019a).

Figure 11. BEI of area of AhS 671 with flaky, porous, fayalitic olivine (fay) of Fo 28-42 intergrown with phyllosilicates dominated by serpentine (serp). Area of [b] is marked in [a].

Figure 12. BEI showing clasts of ureilitic olivine (oliv) and pigeonite (pig) enclosed or in direct contact with C1 material in AhS 91A and AhS 671. Olivine clasts in (a,c,d) show reduction rims (Mg-enriched olivine containing tiny grains of metal), which are a characteristic feature of ureilite olivine. Olivine clast of Fo 78 shown in (e) contains sub-micron sized lamellar exsolutions of chromite (chr) + pyroxene (px), a feature that has observed in olivine of Fo 75-78 in ureilites. Samples: (a) AhS 91A_2A; (b) AhS 91A_6A; (c) AhS 91A_2B; (d) AhS 671_4-17; (e) AhS 91A_2A; (f) AhS 91A_9.

Figure 13. BEI showing clasts of ureilitic pigeonite (a,b,c), graphite (d), and plagioclase (e,f) in AhS 91A and AhS 671. (e) Optical (stereo microscope) image of albite grain in C1 material in AhS 91A. This grain was first observed on surface of the fragment, as shown here. It subsequently fell out and was mounted separately for EMPA. Pigeonite in (c) shows patches of impact-smelted texture, characterized by reduced composition, blebs of metal, and pores (black),

which is common in pigeonite in Almahata Sitta ureilites. Samples: (a) AhS 91A_9; (b) AhS 91A_6B; (c) AhS 671_4-6; (d) AhS 91A_9; (e) AhS 91A_3; (f) AhS 91_1. Pig = pigeonite; gph = graphite; plag = plagioclase; Ca-px = Ca-rich pyroxene.

Figure 14. Compositions of olivine clasts in AhS 91A and AhS 671 compared with olivine in other groups of meteorites. (a) Plot of molar Fe/Mg vs. Fe/Mn. (b) Plot of wt.% Cr_2O_3 vs. wt.% CaO. In combination, these two plots show that olivine in main group ureilites, typical polymict ureilites, and ureilitic stones from Almahata Sitta show a characteristic compositional range, which distinguishes them from olivine in other groups of achondrites and most chondrites. The olivine clasts in AhS 91A and AhS 671 are consistent with ureilitic compositions. Data sources as follows. Acapulcoites and lodranites: Nagahara (1992); Takeda et al. (1994); Papike et al. (1995); Mittlefehldt et al. (1996); Buroni and Folco (2008); Goodrich et al. (2011). Brachinite clan meteorites: Nehru et al. (1983); Warren and Kallemeyn (1989); Petaev et al. (1994); Delaney et al. (2000); Goodrich and Righter (2000); Mittlefehldt et al. (2003); Goodrich et al. (2006, 2011, 2017d); Gardner-Vandy et al. (2012, 2013); Day et al. (2015). Winonaites/IAB silicates: Kimura et al. (1992); Benedix et al. (1998). Main group ureilites: Goodrich et al. (1987, 2001, 2006, 2013a, 2014); Takeda (1987, 1989); Treiman and Berkley (1994); Goodrich and Righter (2000); Inoue et al. (2016); Singletary and Grove (2003); Weber et al. (2003); Warren and Rubin (2011). Typical polymict ureilites: Downes et al. (2008). C1 chondrites: Steele (1990); Leshin et al. (1997); Frank et al. (2014). C2 chondrites: Brearley and Jones (1998). Type 4-6 OC and EC: Brearley and Jones (1998). R-chondrites: Bischoff et al. (2011).

Figure 15. Compositions of low-Ca pyroxene clasts in AhS 91A and AhS 671 compared with low-Ca pyroxenes in other groups of meteorites. (a) wt. % FeO vs. wt.% Al_2O_3. (b) Wo content (molar CaO/[CaO+FeO+Mg]) vs. wt.% Cr_2O_3. These two plots show that low-Ca pyroxenes in main group ureilites, typical polymict ureilites, and ureilitic stones from Almahata Sitta are well distinguished from those in other groups of meteorites. With one exception, the pigeonite and orthoyproxene clasts in AhS 91A and AhS 671 are consistent with the ureilite fields (the boundary between pigeonite and orthopyroxene is defined compositionally at Wo = 5). One orthopyroxene clast of very low Wo content is out of the range of ureilites and consistent with orthopyroxene in type 4-6 enstatite chondrites. Data sources as follows. Main group ureilites: Goodrich et al. (1987, 2001, 2009, 2013a, 2014); Takeda (1987, 1989); Takeda et al. (1989); Treiman and Berkley (1994); Weber et al. (2003); Singletary and Grove (2003); Inoue et al. (2016). Typical polymict ureilites: Downes et al. 2008); Acapulcoites and lodranites: Mittlefehldt et al. (1998); Eucrites: Mittlefehldt et al. (1998); R-chondrites: Bischoff et al. (2011). Other chondrites: Brearley and Jones (1998).

Figure 16. (a) BEI of kamacite-troilite-metal assemblage surrounded by C1 matrix material in AhS 91_1 (see Fig. 18a for location). Texture and compositions (Table 5) of this assemblage are consistent with derivation from an ordinary chondrite. (b) Optical (stereo microscope) image of an elongated grain (1.2 mm long) of Si-bearing kamacite embedded in C1 material in AhS 91A_9. The grain subsequently fell out and was mounted separately for EMPA. Its composition (Table 5) is consistent with derivation from an EH chondrite. (c) and (d) = BEI showing inclusions of enstatite and niningerite within the metal grain shown in [b].

Figure 17. Compositions of kamacite grains in AhS 91A and AhS 671 compared with compositions of metal in ureilites, ordinary chondrites (OC), enstatite chondrites (EC), and iron meteorites. Three different types of metal are distinguished by composition and associated minerals. Data for ureilites from Goodrich et al. (2013b); ordinary chondrites from Rubin (1990), Zanda et al. (1994), Afiattalab and Wasson (1980); Brearley and Jones (1998), Reisener and Goldstein (2003); enstatite chondrites from Weisberg and Kimura (2012); Horstmann et al. (2014); Brearley and Jones (1998); iron meteorites from Goldstein et al. (2017), Brearley and Jones (1998), Rout et al. (2017).

Figure 18. (a) Combined elemental X-ray map of polished section of AhS 91_1. Red = Mg, green = Ca, blue = Fe, magenta = S. Section shows dominantly C1 material, containing clasts of ureilitic minerals (olivine, pigeonite, plagioclase, orthopyroxene), a metal-sulfide globule, (shown in Fig. 16a), and four chondrules. (b) BEI of chondrule #2 from [a]. Type IAB POP. (c) BEI of chondrule #3 from [a]. Type IAB. (d) BEI of chondrule #4 from [a]. Type IIAB POP. (e) BEI of kamacite-metal grain in chondrule #4, area outlined by red box in [d]. (f) BEI of chondrule #5 from [a]. Type IAB POP. opx = orthopyroxene; ol = olivine.

Figure 19. (a) Frame from XRCT scan of fragment AhS 91_1, showing several chondrules in the interior, not yet exposed in section. (b,c) BEI of brecciated zone in AhS 91_01, exposed by polishing down the section shown in Fig. 18. Lithic and mineral fragments of mixed ureilitic (ur), C1, and chondrule-like (ch) materials. (d) Plot of wt.% Cr_2O_3 vs. wt.% CaO in olivine grains from the areas in [b,c], showing that some of these grains could be derived from chondrules similar to chondrules #2-5 (Fig. 18), whereas others are ureilitic.

Figure 20. (a) Three oxygen isotope plot showing bulk compositions of fragments of AhS 91A and AhS 671 dominated by the C1 lithology. These compositions do not match those of any known chondrite group, but are very similar to the composition of a CC-like clast from the Nilpena polymict ureilite (Brearley and Prinz 1992). A "metallic" looking chip removed from the AhS 91A fragment has a composition on the terrestrial fractionation line (TFL), and was found to consist of iron oxides/hydroxides (rust). The bulk composition obtained for AhS 671 is consistent with being a mix of AhS 91A and terrestrial contamination similar to the "metallic" chip. Also shown are oxygen isotope compositions obtained by SIMS for various components of AhS 91_1 (Fig. 18). Clasts of olivine, pyroxene, and plagioclase in this section have oxygen isotope compositions consistent with those of main group ureilites and silicate clasts in typical polymict ureilites. Olivine and pyroxene in chondrules #2-4 (Fig. 18b-d) have oxygen isotope compositions consistent with those of olivine and pyroxene in chondrules in LL3.0-3.1 chondrites (Kita et al. 2010). One olivine grain in chondrule #3 is more ^{16}O-rich ($\Delta^{17}O$=-2.8‰) and may be a relict grain (remnant of chondrule precursors). Olivine and pyroxene in chondrule #5 have oxygen isotope composition out of the range of OC and consistent with olivine and pyroxene in primitive (type 3) CC (Ushikubo et al. 2012; Tenner et al. 2015). (b) Three oxygen isotope plot showing compositions obtained by SIMS from the core and zoned rim of a carbonate (breunnerite) grain in AhS 91_0 (Fig. 18). These data show $\Delta^{17}O$ slightly higher than bulk AhS 91A, and form a mass-dependent fractionation line (slope = 0.526, correlation coefficient 0.999). Main group ureilite data from Clayton and Mayeda (1996); clasts in typical polymict ureilites from Downes et al. (2008) and Kita et al. (2004, 2006).

Figure 21. (a) Bulk sample reflectance spectra from 0.3 to 3.6 μm for chips and powdered samples of AhS 91A and AhS 671. Data for CM and ungrouped C2 chondrites (Hiroi et al. 2017) for comparison. (b) VNIR reflectance spectra. Asteroid 2008 TC_3 was measured in the 0.55 to 1 μm range (Jenniskens et al. 2009) and is shown in light grey at the range of albedo estimates of Jenniskens et al. (2009) and Hiroi et al. (2010). Spectra for chips and coarse (125-500 μm) powders of AhS ureilites and ordinary chondrite from Hiroi et al. (2010). Spectra for chips (solid cyan lines) and powders (dashed cyan lines) of AhS 1002 and AhS 2012 enstatite chondrites and AhS 91A from this work. (c) Spectrum of asteroid 2008 TC_3 (original data in light grey; 55-pt averaged spectrum in red with standard deviations [sd] in dark grey), normalized to 1 at 0.55 μm, compared with model spectra for mixtures of AhS stones from Hiroi et al. (2010) and calculated in this work. (d) Model spectra (black) for mixtures of AhS ureilites + AhS 91A + OC calculated in this work and by Hiroi et al. (2010) compared with asteroid 2008 TC_3 (original data in light grey; 55-pt averaged spectrum in red) scaled to match the 0.55 μm reflectance of the mixtures in each case. Also shown in blue is the average spectrum of F-type asteroids (Tholen 1984) normalized to the average F-type albedo of 0.046 (Mainzer et al. 2011) at 0.55 μm.

Figure 22. Whole-rock reflectance spectrum of fragment AhS 91A_1 from μ-FTIR compared to similarly acquired spectra of carbonaceous chondrites (Hamilton 2018; Hamilton et al. 2018). Spectra are normalized and offset for comparison. Vertical lines denote features described in text.

Figure 23. Whole-rock reflectance spectrum of Almahata Sitta fragment 91A_1 from μ-FTIR compared to spectra isolated from areas 1 and 4 (Fig. 3a). Spectra are normalized and offset for comparison. Vertical line denotes position of OH^- feature described in text.

Figure 24. Comparison of AhS 91A_1 area 4 reflectance and phyllosilicate mineral spectra measured in emission. Spectra are normalized and offset for comparison. Vertical lines denote positions of key features in the AhS area 4 spectrum at 1116, 1015, 640, and 456 cm^{-1}.

Figure 25. (a) Backscattered electron image of carbonate grain in fragment AhS 671_2. (b) μ-FTIR reflectance spectrum of carbonate grain in (a). (c) Backscattered electron image of fragment AhS 671_3 showing the outline of the area of the oversampled μ-FTIR map in yellow. (d) Average μ-FTIR spectrum of the area outlined in (c) exhibiting features of both phyllosilicate and olivine. (e) Laboratory emission spectrum of lizardite (inverted for comparison to reflectance) and the phyllosilicate spectrum recovered from AhS 671_3 by factor analysis. Features are not perfectly matched due to compositional differences between terrestrial and meteoritic serpentines. (f) Laboratory emission spectrum of synthetic olivine (Fo_{30}) from Lane et al. (2011) and the olivine spectrum recovered from AhS 671_3 by factor analysis.

Figure 26. Neon three isotope plot showing the data points for AhS 91A_12, AhS 91A_14 and AhS 91A_15. They appear to plot on a mixing line between a trapped component (upper left) and a cosmogenic Ne endmember composition (lower right). The spread along the line suggests varying mixing ratios of these two endmembers, with AhS 91A_14 containing by far more trapped Ne relative to cosmogenic Ne than the other two samples. This is consistent with the huge trapped ^{36}Ar concentration detected in AhS 91A_14 relative to AhS 91A_12 and AhS 91A_15 (see text). Extrapolation of this line to a typical trapped $^{21}Ne/^{22}Ne$ (0.0294) yields a

$^{20}Ne/^{22}Ne$ ratio of 10.45±0.05, similar to Ne observed in phase Q and ureilites. The remarkably constant trapped $^{20}Ne/^{22}Ne$ ratio observed for all three samples suggests that the additional trapped component in AhS 91A_14 is not SW, which would shift the data point towards higher $^{20}Ne/^{22}Ne$. References: HL (noble gas component residing in presolar diamonds) − Huss and Lewis (1995); Q − Busemann et al. (2000); "ureilites" − Göbel et al. (1978) and Ott et al. (1985); SW (solar wind as measured by Genesis) − Heber et al. (2009); GCR (typical range for cosmogenic Ne) − Wieler (2002).

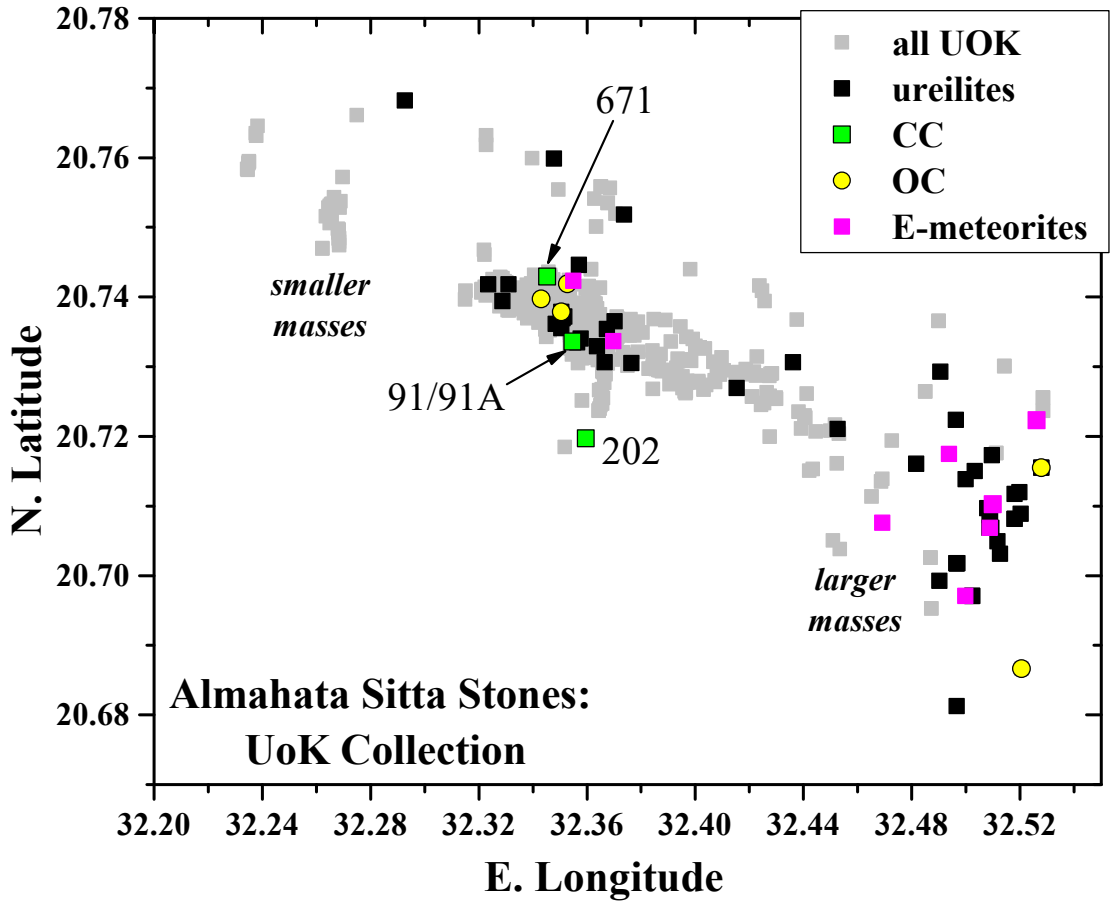
all UOK
ureilites
CC
OC
E-meteorites
671
91/91A
202
smaller masses
larger masses
Almahata Sitta Stones:
UoK Collection
N. Latitude
E. Longitude
20.78
20.76
20.74
20.72
20.70
20.68
32.20
32.24
32.28
32.32
32.36
32.40
32.44
32.48
32.52

Fig. 1

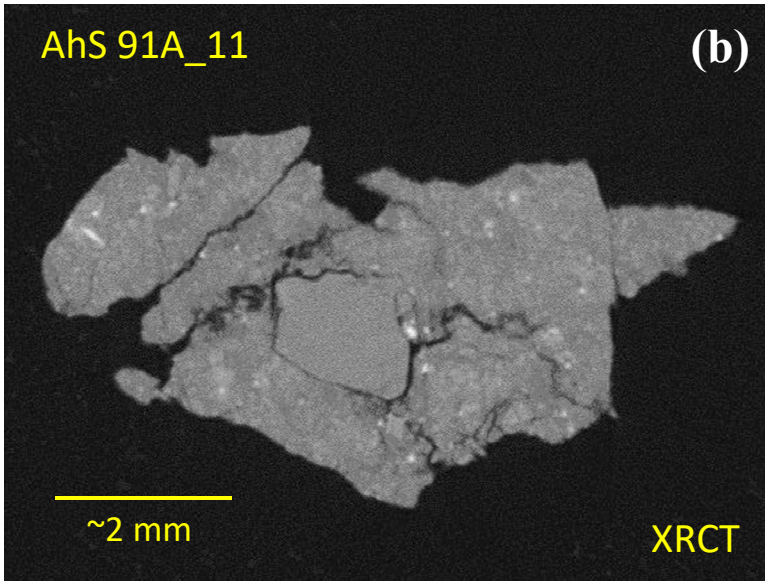

Fig. 2

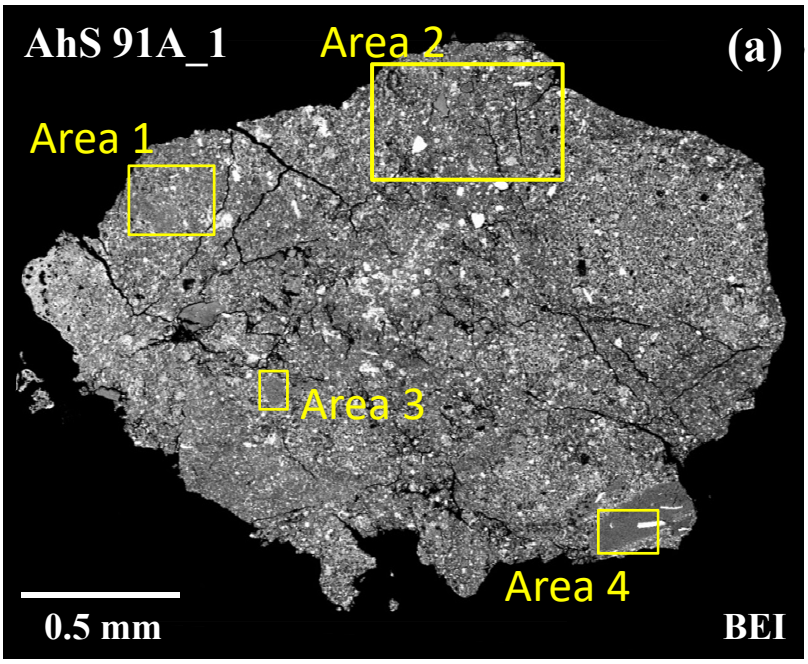
AhS 91A_1
(a)
Area 1
Area 2
Area 3
Area 4
0.5 mm
BEI

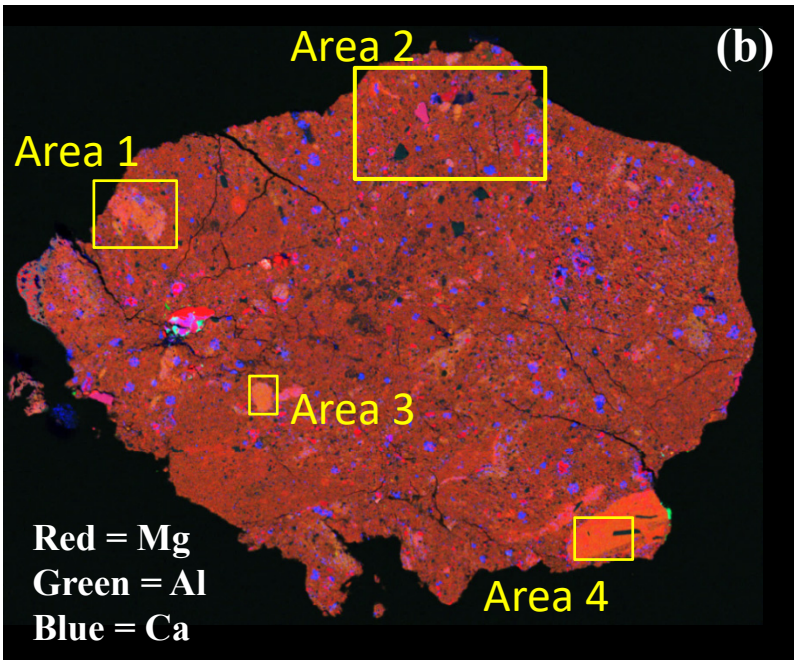
(b)
Area 1
Area 2
Area 3
Area 4
Red = Mg
Green = Al
Blue = Ca

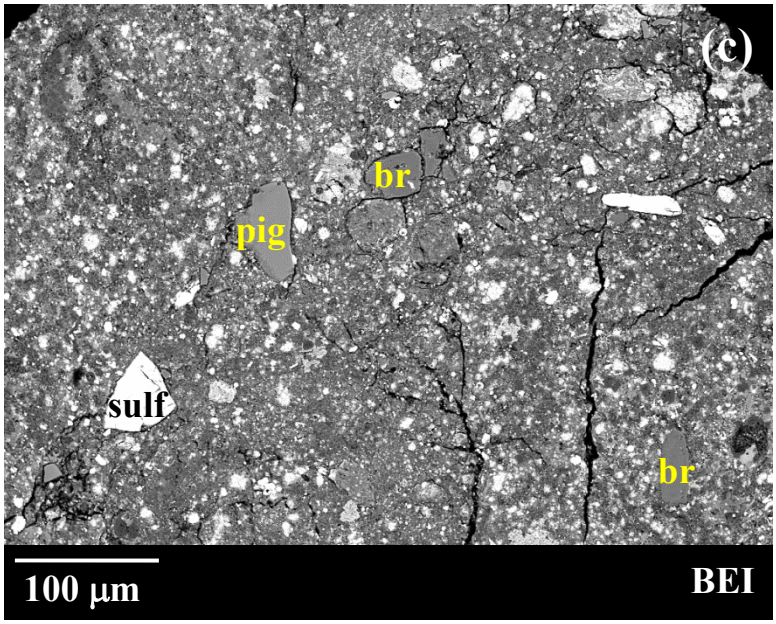
(c)
br
pig
sulf
br
100 µm
BEI

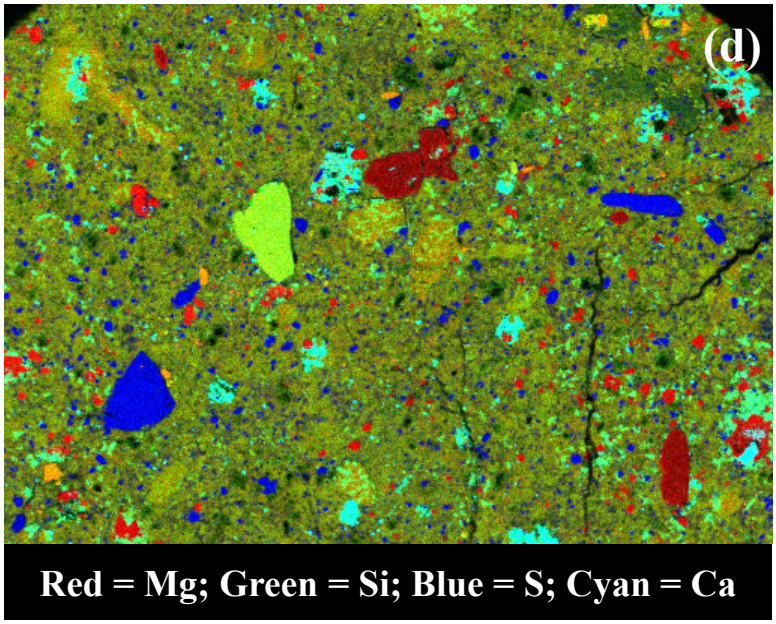
(d)
Red = Mg; Green = Si; Blue = S; Cyan = Ca

Fig. 3

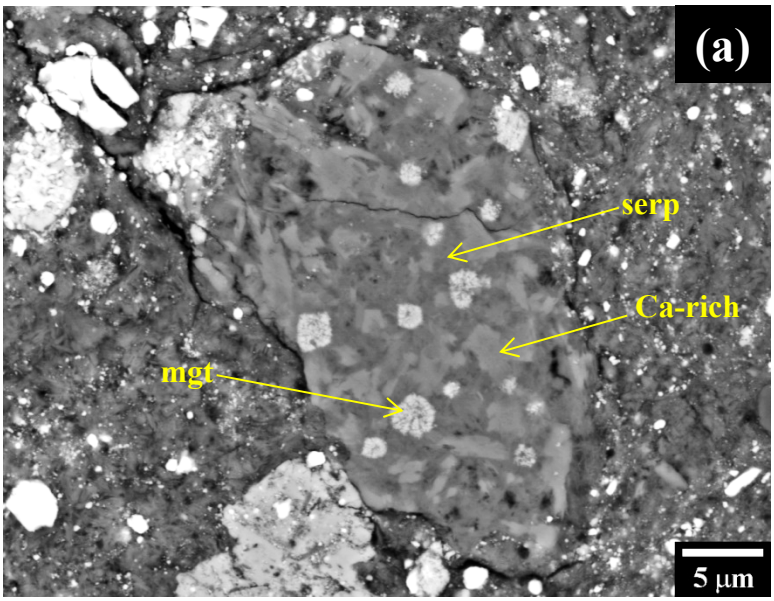
(a)
serp
Ca-rich
mgt
5 μm

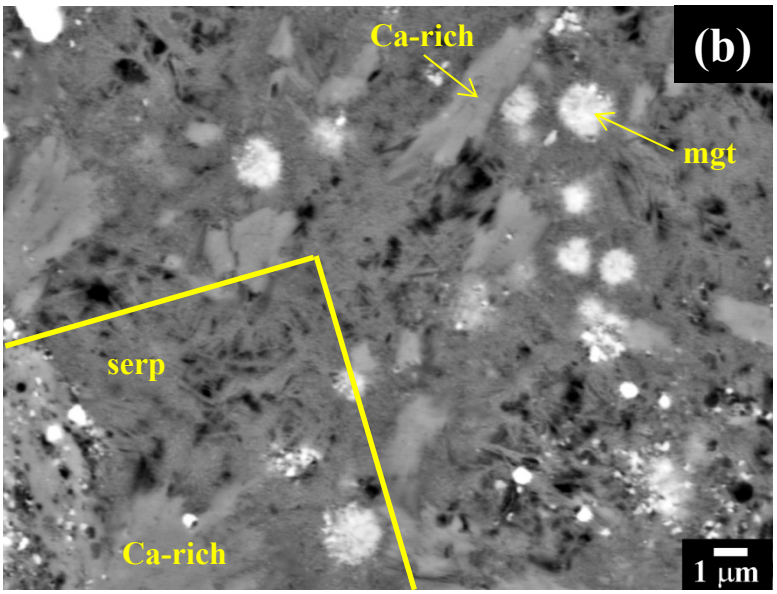
(b)
Ca-rich
mgt
serp
Ca-rich
1 μm

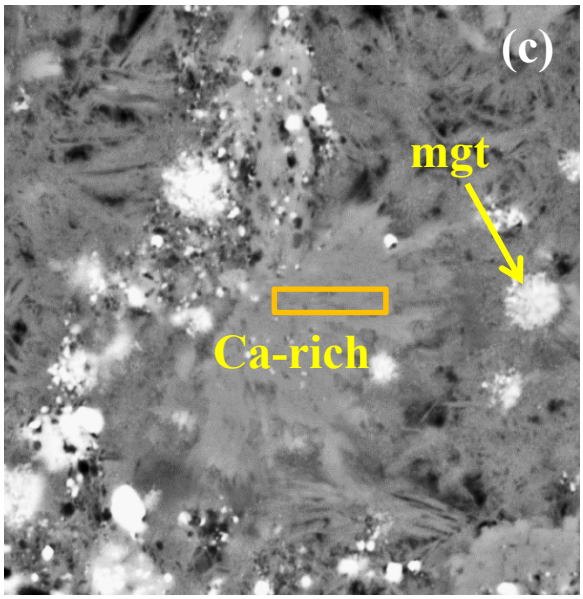
(c)
mgt
Ca-rich

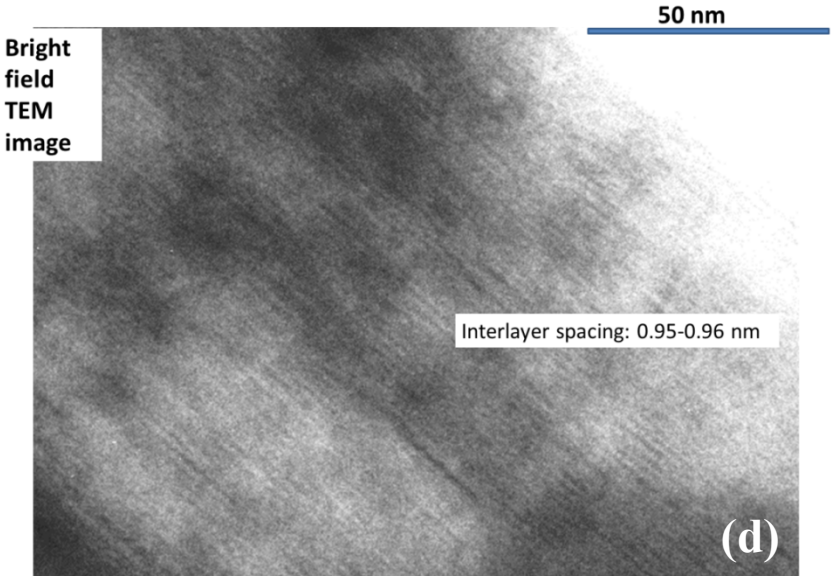
50 nm
Bright field TEM image
Interlayer spacing: 0.95-0.96 nm
(d)

Fig. 4

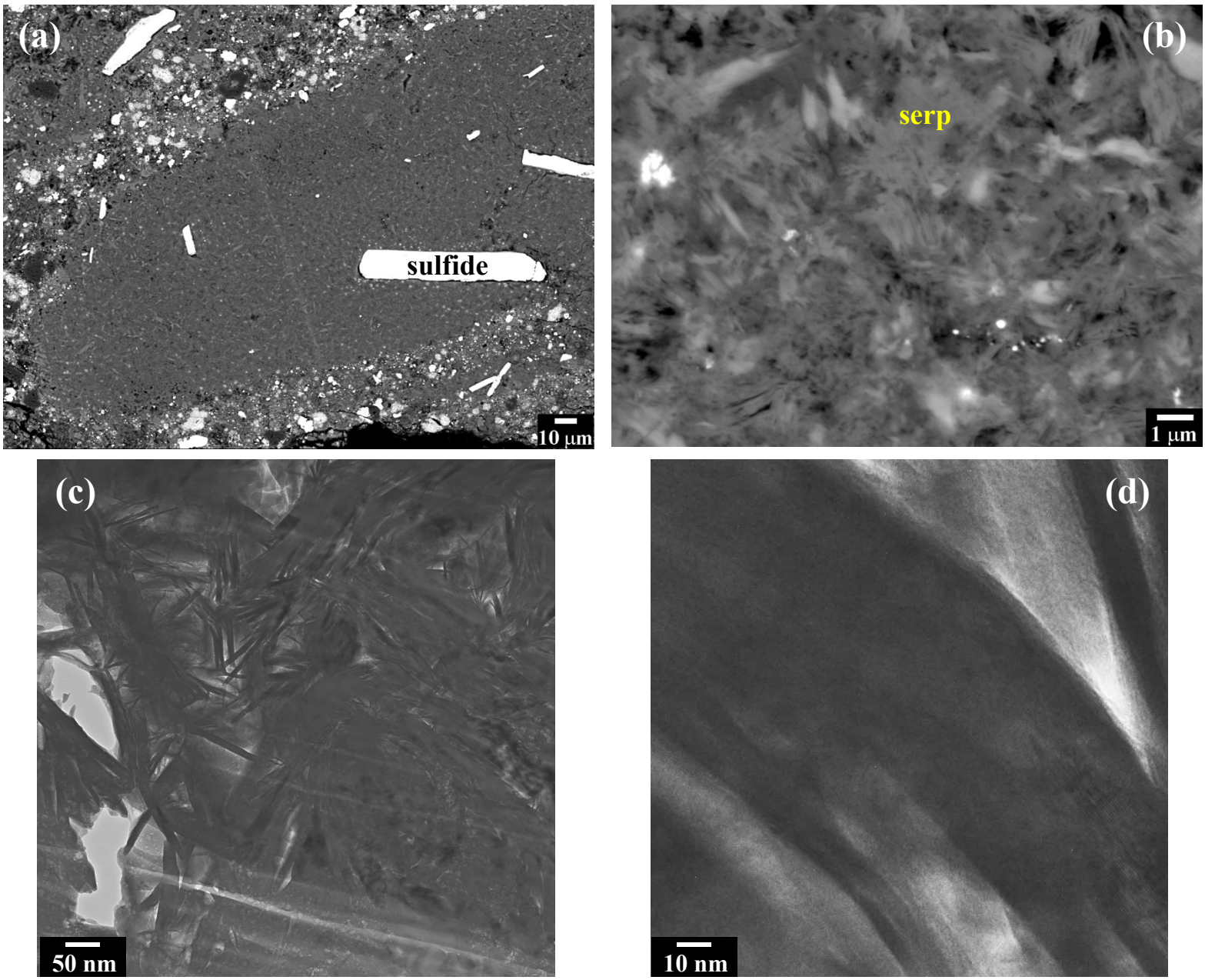

Fig. 5

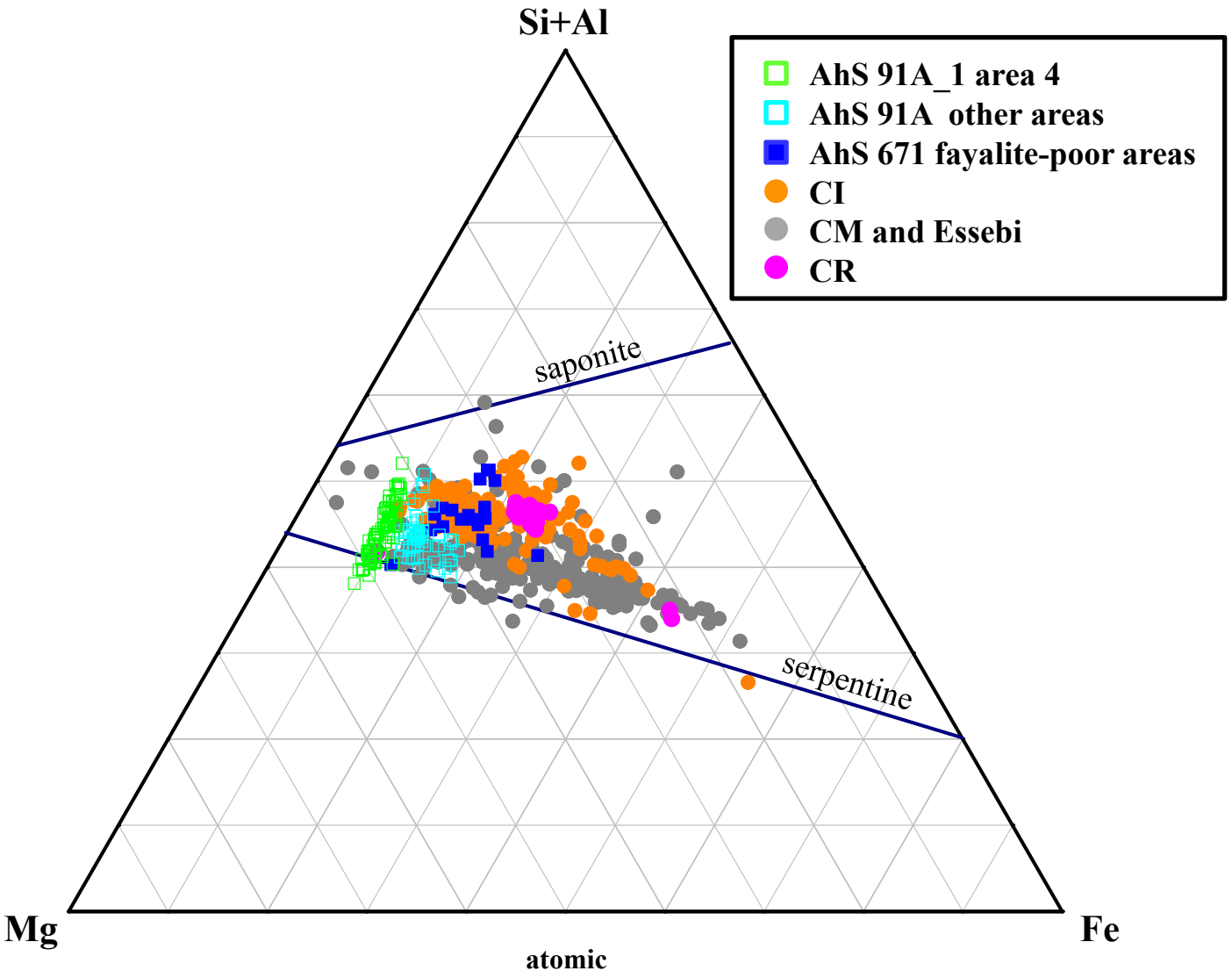
Si+Al
AhS 91A_1 area 4
AhS 91A_other areas
AhS 671 fayalite-poor areas
CI
CM and Essebi
CR
saponite
serpentine
Mg
Fe
atomic

Fig. 6

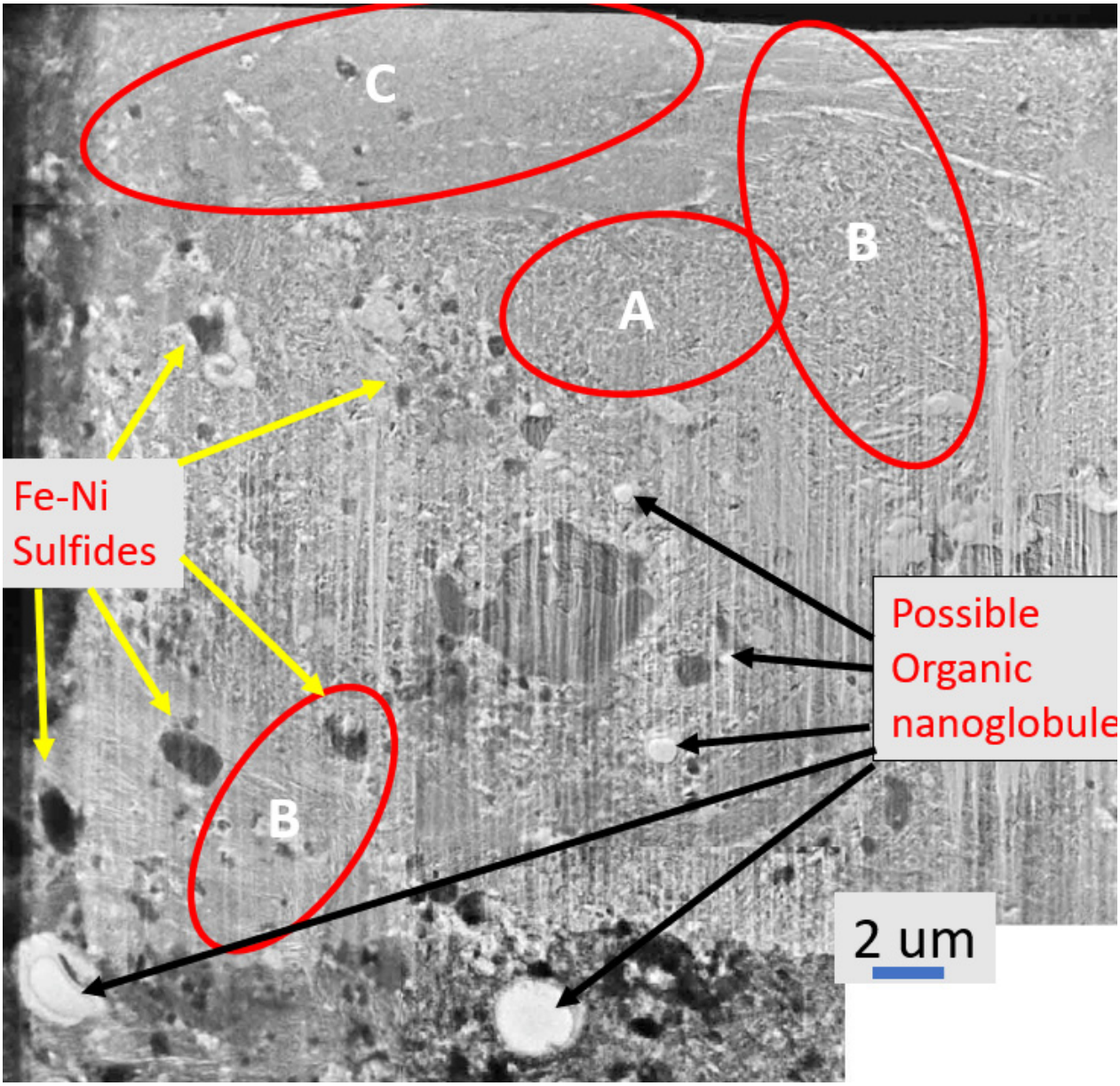

Fig. 7

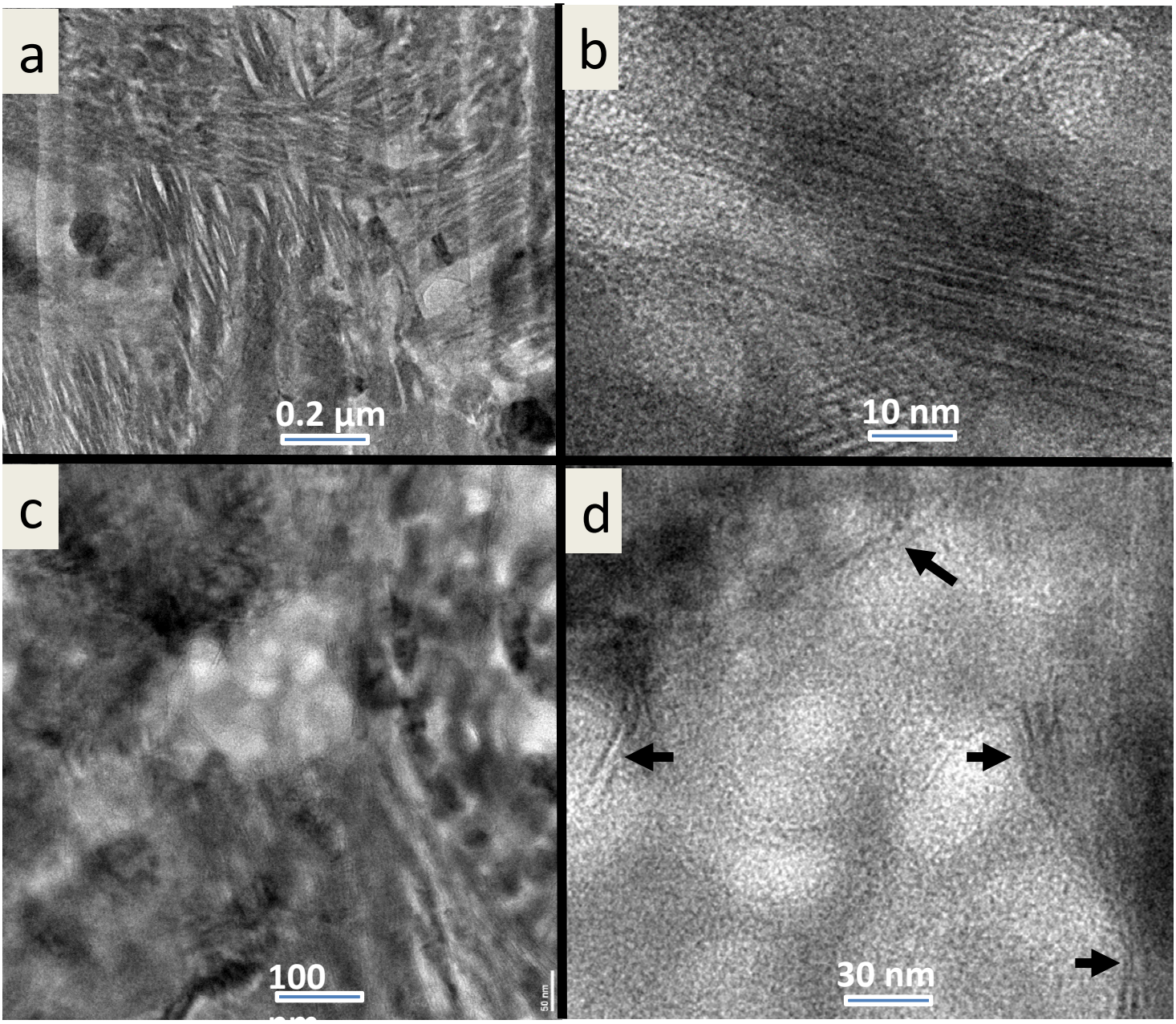

Fig. 8

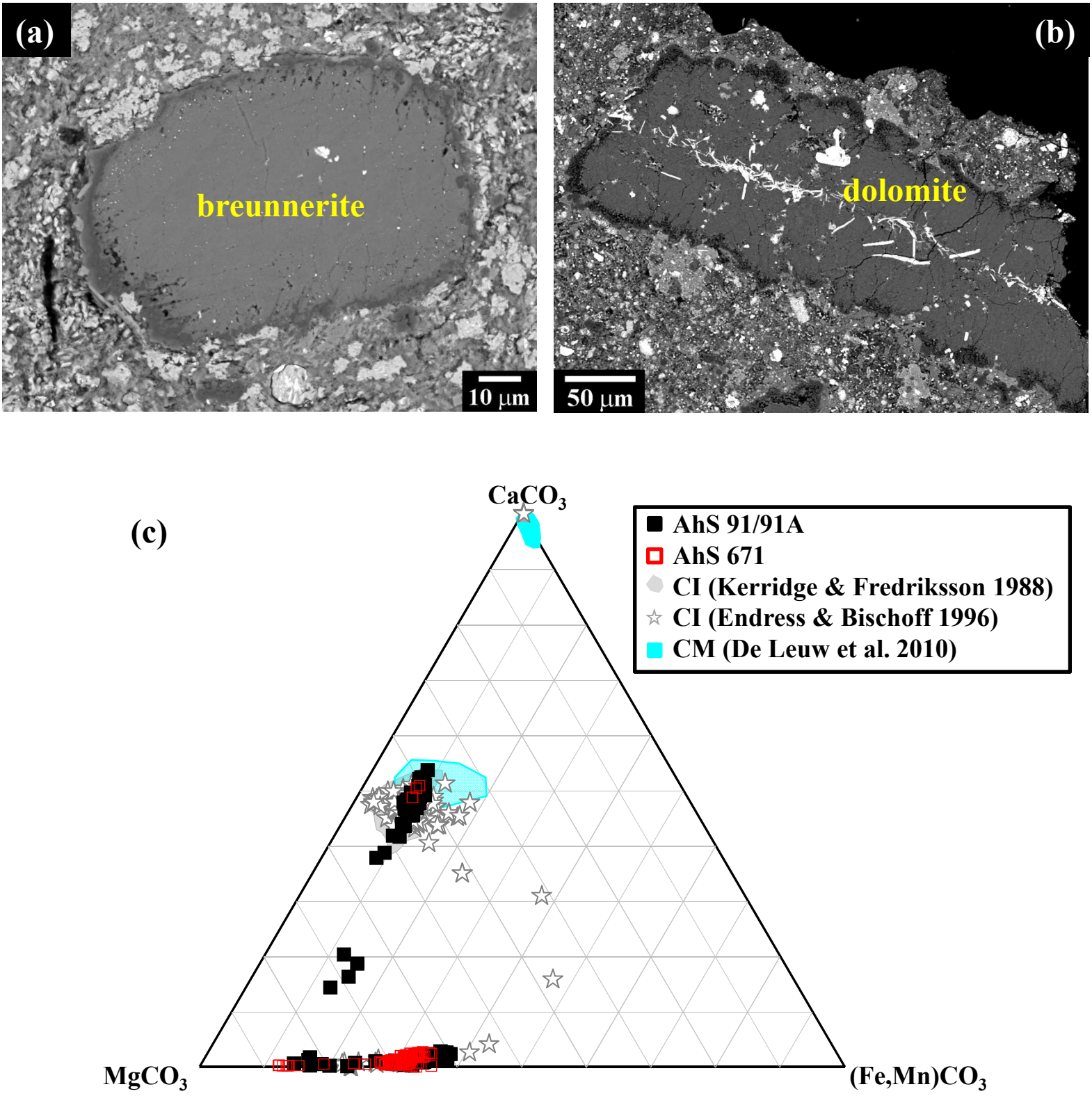
(a)
breunnerite
10 μm
(b)
dolomite
50 μm
(c)
CaCO3
MgCO3
(Fe,Mn)CO3
AhS 91/91A
AhS 671
CI (Kerridge & Fredriksson 1988)
CI (Endress & Bischoff 1996)
CM (De Leuw et al. 2010)

Fig. 9

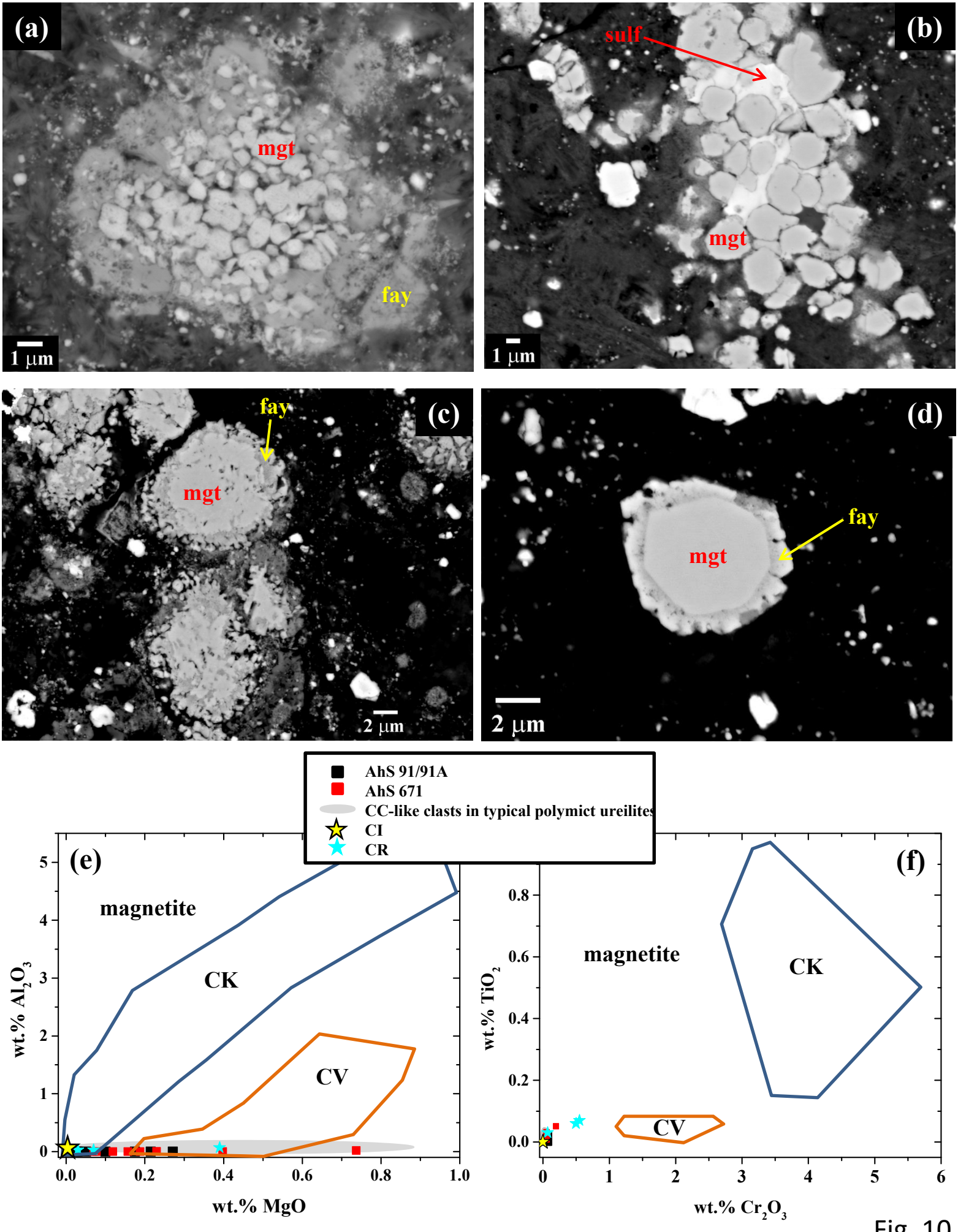
(a)
mgt
fay
1 μm
(b)
sulf
mgt
1 μm
(c)
fay
mgt
2 μm
(d)
fay
mgt
2 μm
AhS 91/91A
AhS 671
CC-like clasts in typical polymict ureilites
CI
CR
(e)
magnetite
CK
CV
wt.% Al2O3
wt.% MgO
(f)
magnetite
CK
CV
wt.% TiO2
wt.% Cr2O3

Fig. 10

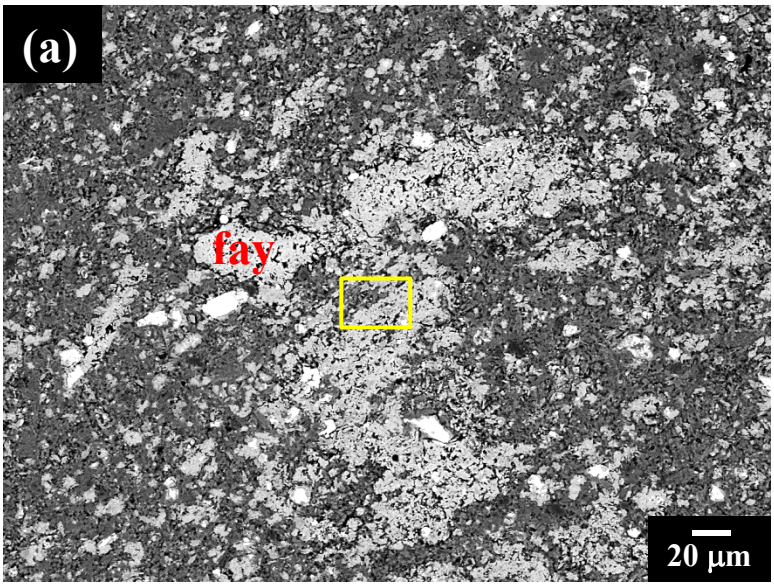

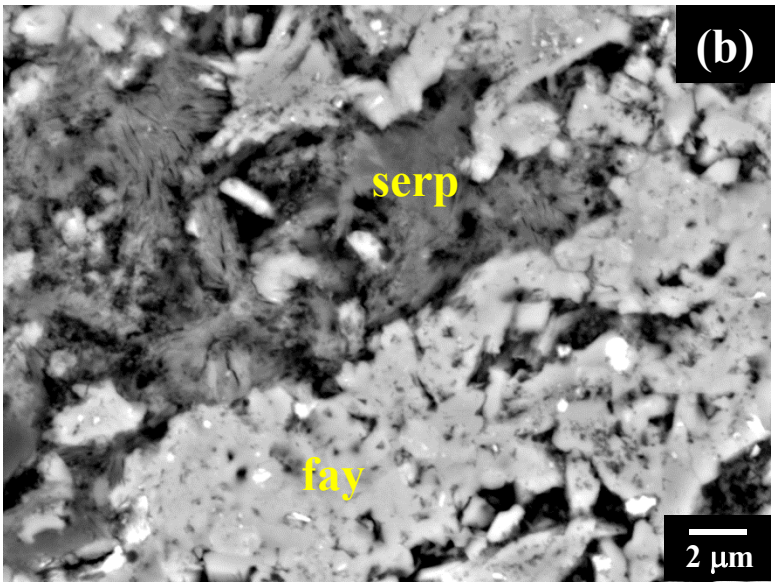

Fig. 11

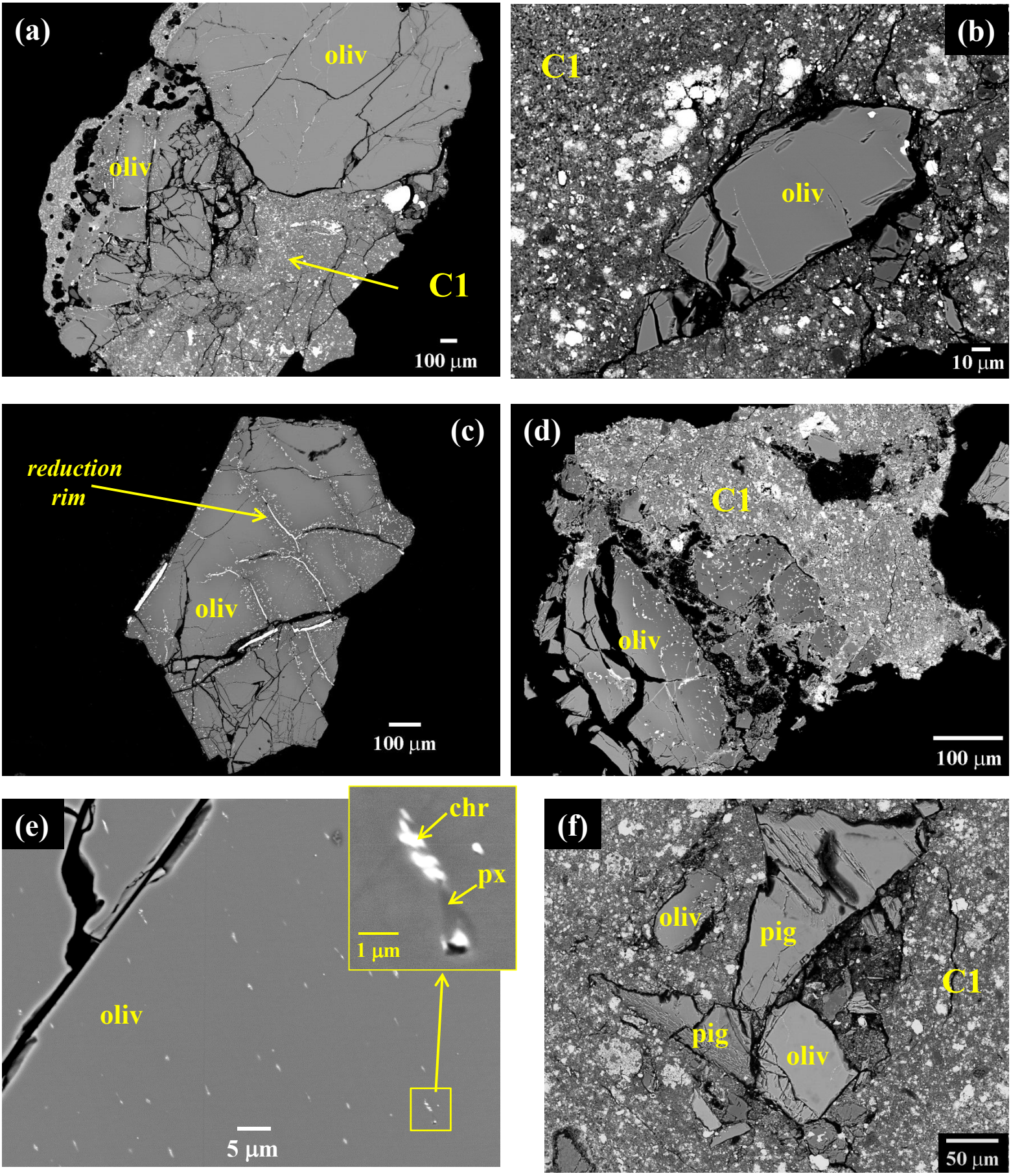
(a)
oliv
oliv
C1
100 μm
(b)
C1
oliv
10 μm
(c)
reduction rim
oliv
100 μm
(d)
C1
oliv
100 μm
(e)
chr
px
1 μm
oliv
5 μm
(f)
oliv
pig
C1
pig
oliv
50 μm

Fig. 12

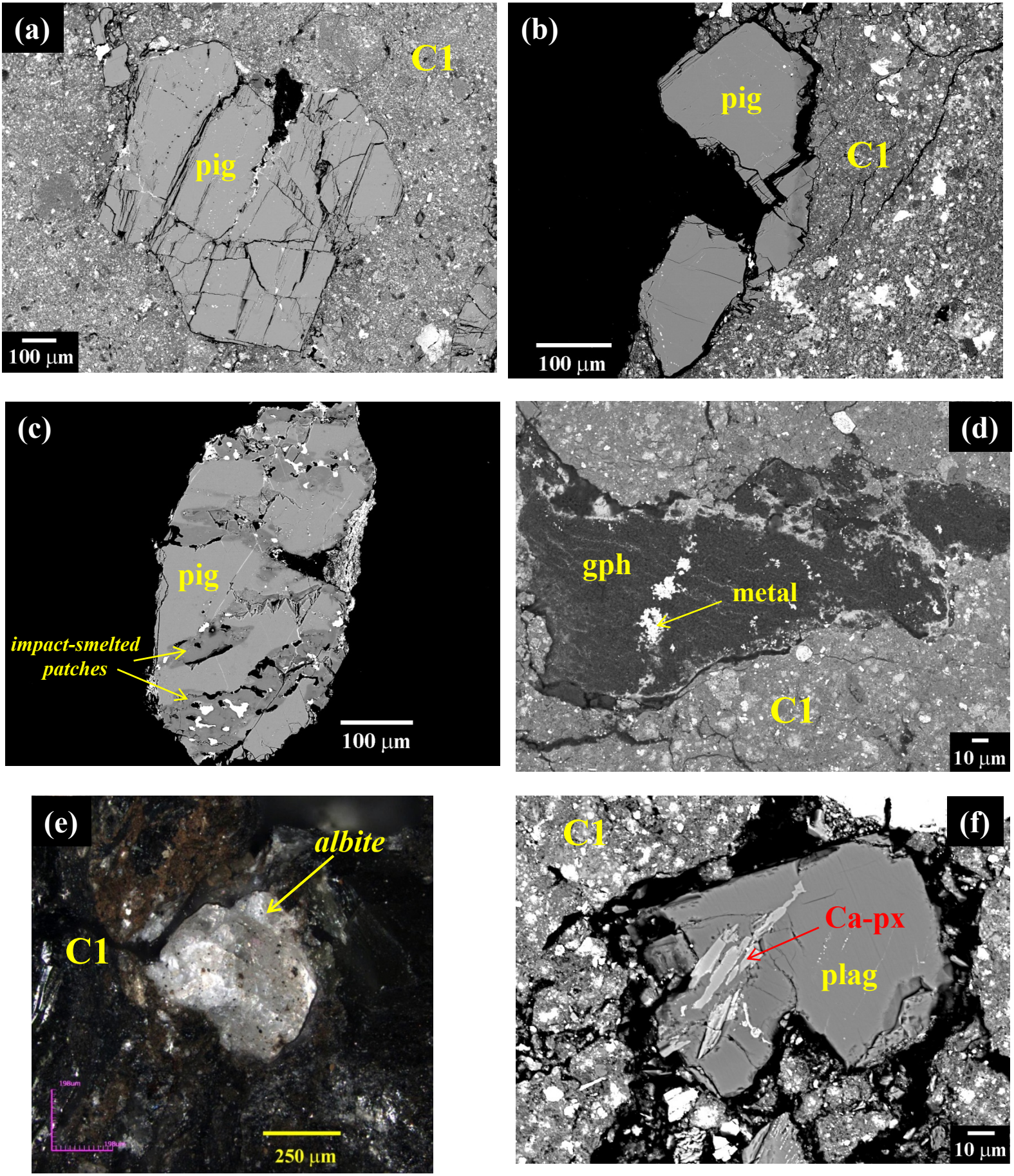
(a)
C1
pig
100 μm
(b)
pig
C1
100 μm
(c)
pig
impact-smelted
patches
100 μm
(d)
gph
metal
C1
10 μm
(e)
albite
C1
250 μm
(f)
C1
Ca-px
plag
10 μm

Fig. 13

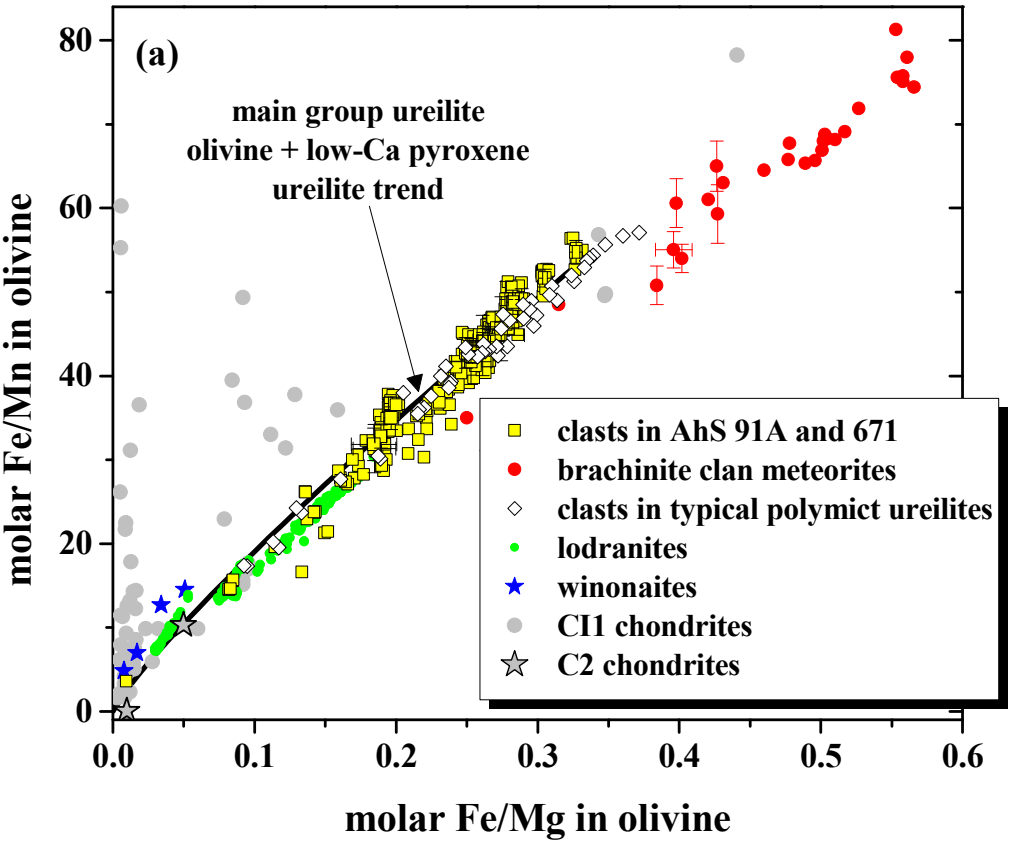
(a)
main group ureilite
olivine + low-Ca pyroxene
ureilite trend
clasts in AhS 91A and 671
brachinite clan meteorites
clasts in typical polymict ureilites
lodranites
winonaites
CI1 chondrites
C2 chondrites
molar Fe/Mn in olivine
molar Fe/Mg in olivine
0
20
40
60
80
0.0
0.1
0.2
0.3
0.4
0.5
0.6

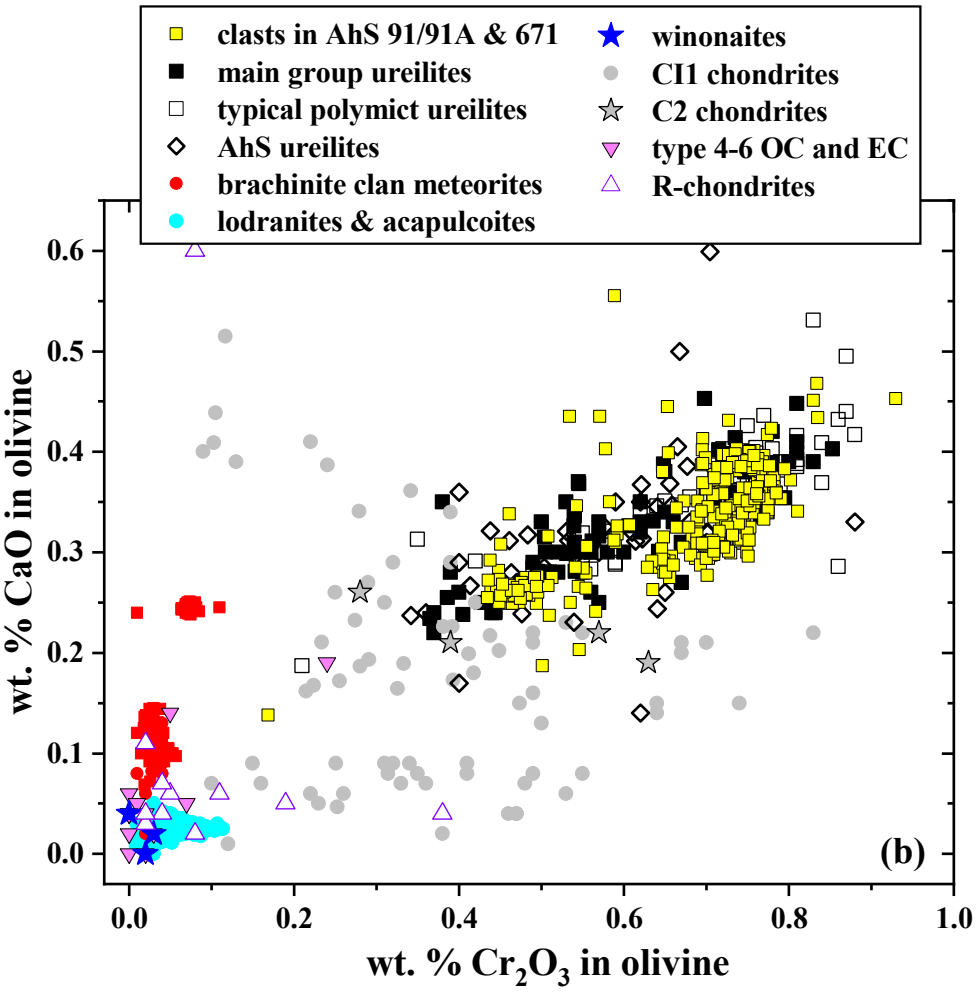
clasts in AhS 91/91A & 671
main group ureilites
typical polymict ureilites
AhS ureilites
brachinite clan meteorites
lodranites & acapulcoites
winonaites
CI1 chondrites
C2 chondrites
type 4-6 OC and EC
R-chondrites
(b)
wt. % CaO in olivine
wt. % Cr2O3 in olivine
0.0
0.1
0.2
0.3
0.4
0.5
0.6
0.0
0.2
0.4
0.6
0.8
1.0

Fig. 14

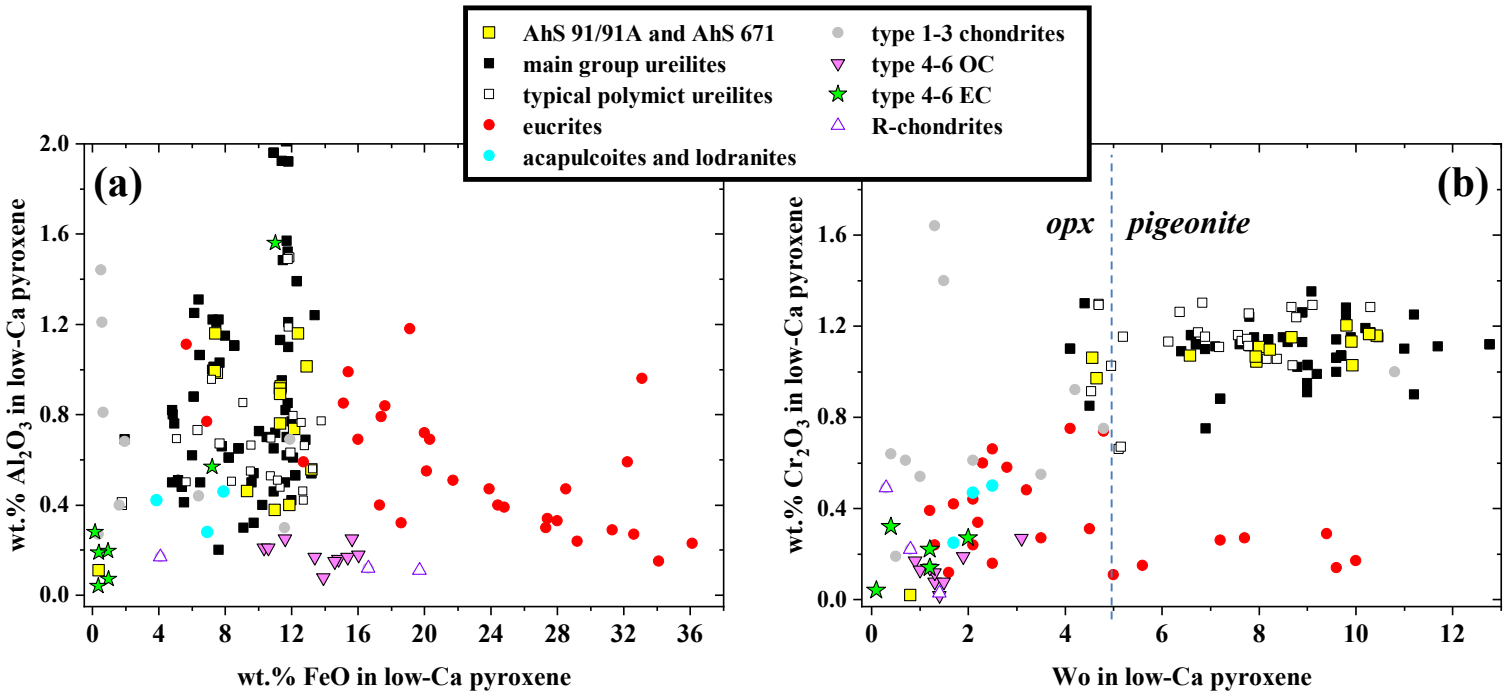
AhS 91/91A and AhS 671
main group ureilites
typical polymict ureilites
eucrites
acapulcoites and lodranites
type 1-3 chondrites
type 4-6 OC
type 4-6 EC
R-chondrites
(a)
wt.% Al_2O_3 in low-Ca pyroxene
wt.% FeO in low-Ca pyroxene
(b)
opx
pigeonite
wt.% Cr_2O_3 in low-Ca pyroxene
Wo in low-Ca pyroxene

Fig. 15

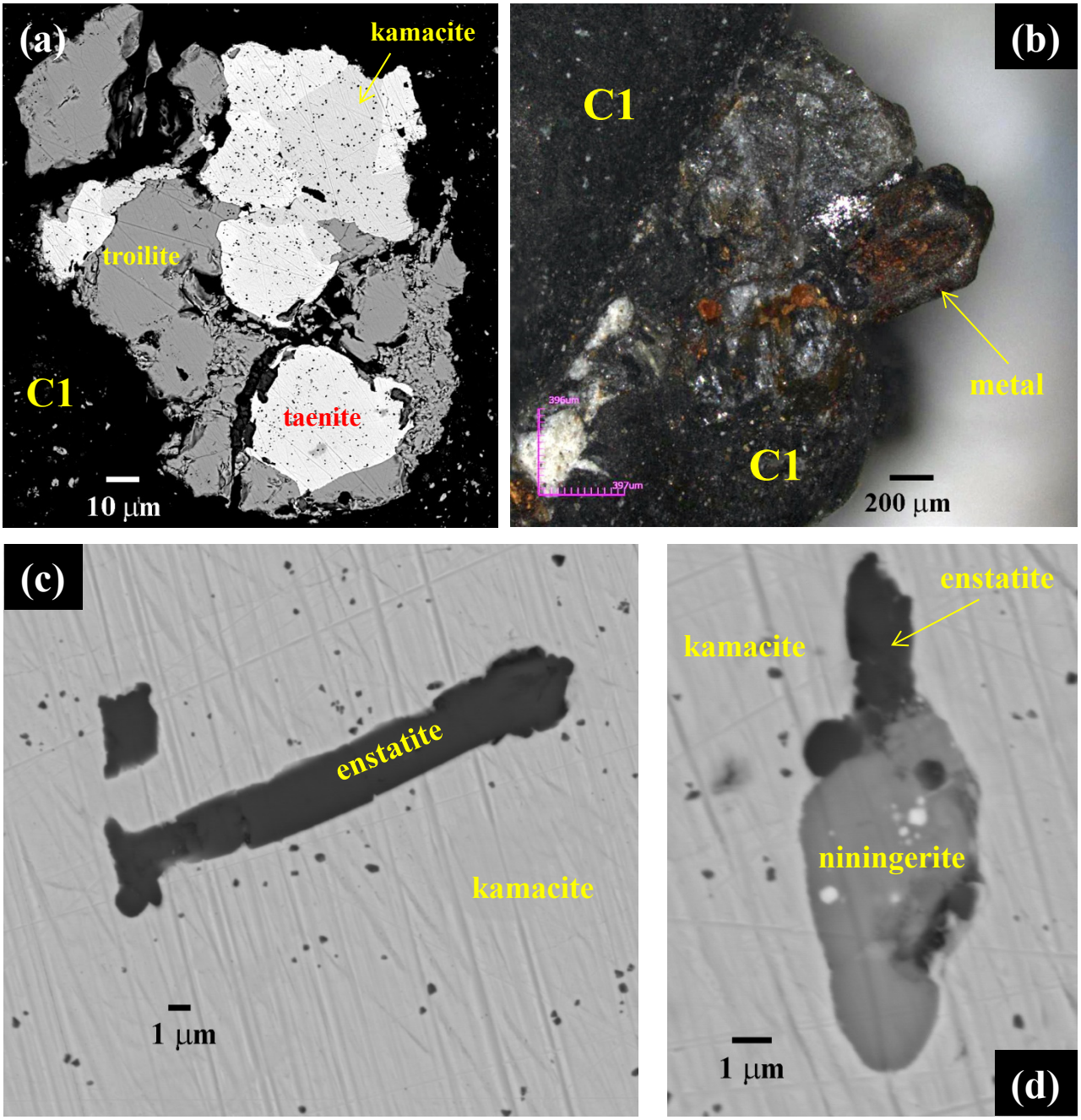
(a)
kamacite
troilite
C1
taenite
10 μm
(b)
C1
metal
C1
200 μm
(c)
enstatite
kamacite
1 μm
enstatite
kamacite
niningerite
1 μm
(d)

Fig. 16

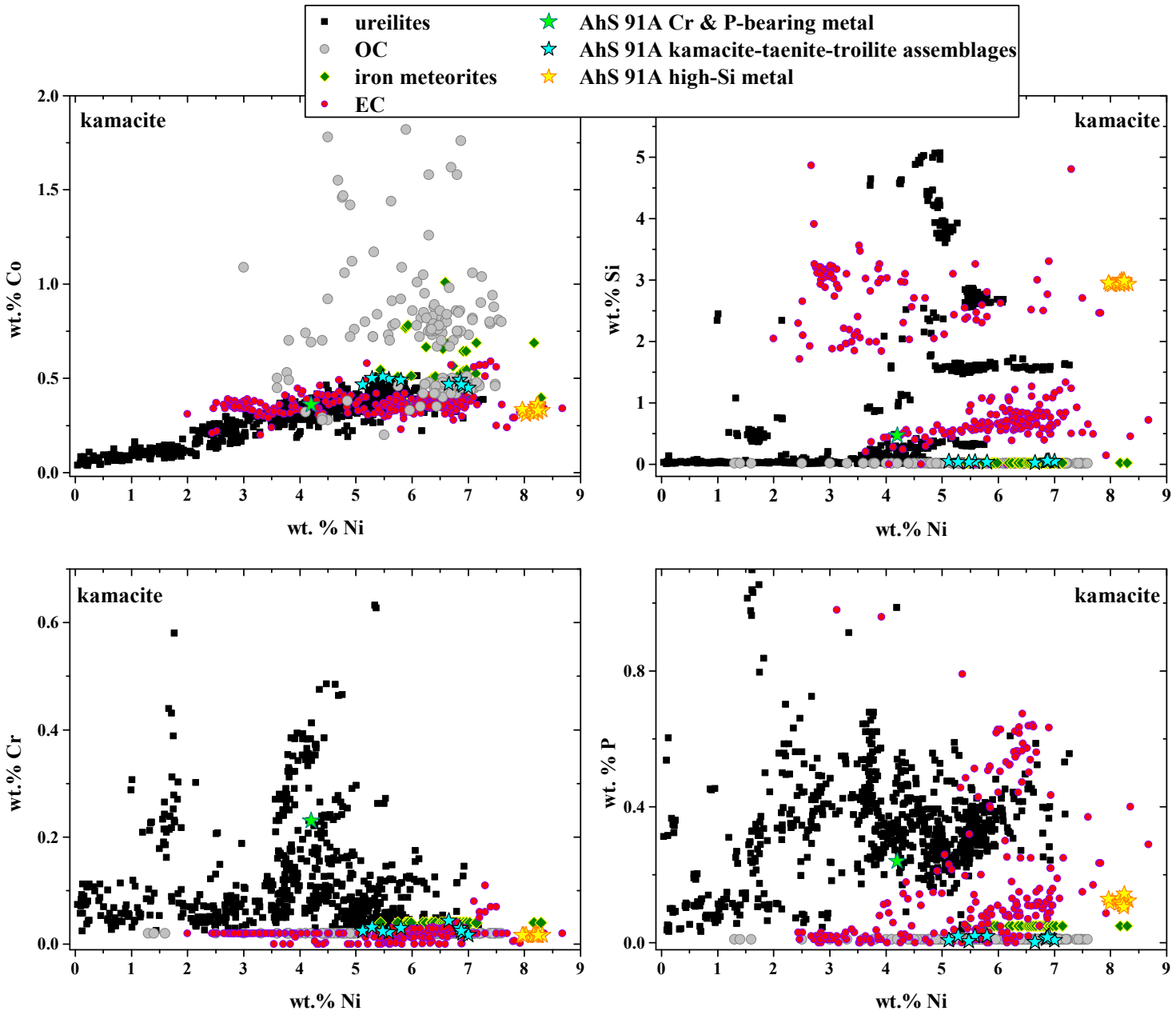
ureilites
OC
iron meteorites
EC
AhS 91A Cr & P-bearing metal
AhS 91A kamacite-taenite-troilite assemblages
AhS 91A high-Si metal
kamacite
wt.% Co
wt. % Ni
kamacite
wt.% Si
wt.% Ni
kamacite
wt.% Cr
wt.% Ni
kamacite
wt. % P
wt.% Ni

Fig. 17

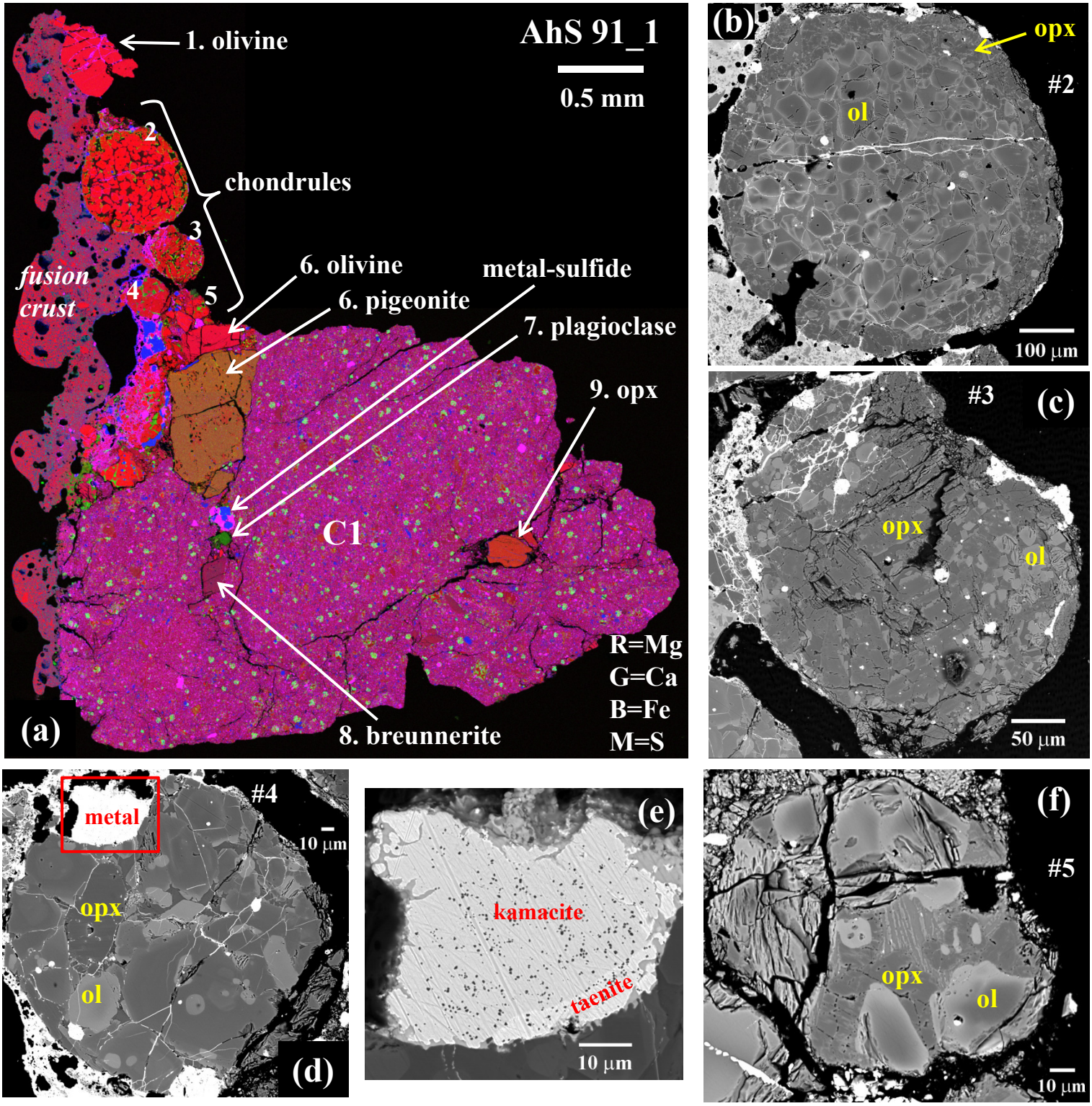
AhS 91_1
0.5 mm
1. olivine
2
chondrules
3
fusion crust
4
5
6. olivine
6. pigeonite
metal-sulfide
7. plagioclase
9. opx
C1
8. breunnerite
R=Mg
G=Ca
B=Fe
M=S
(a)
(b)
opx
#2
ol
100 μm
(c)
#3
opx
ol
50 μm
(d)
#4
metal
10 μm
opx
ol
(e)
kamacite
taenite
10 μm
(f)
#5
opx
ol
10 μm

Fig. 18

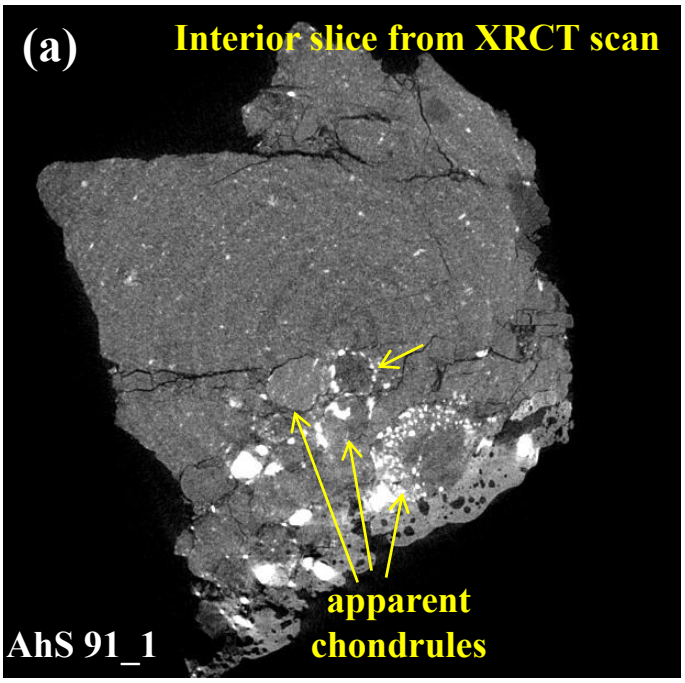
(a)
Interior slice from XRCT scan
apparent
chondrules
AhS 91_1

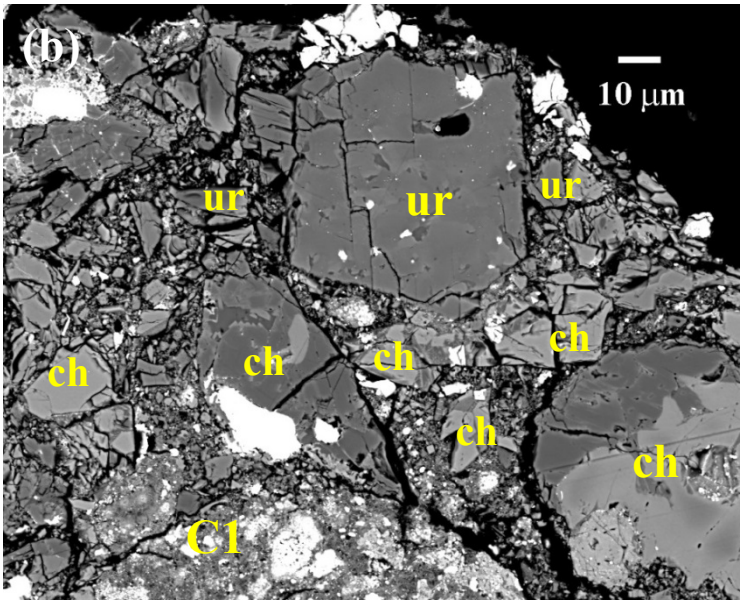
(b)
10 μm
ur
ur
ur
ch
ch
ch
ch
ch
ch
C1

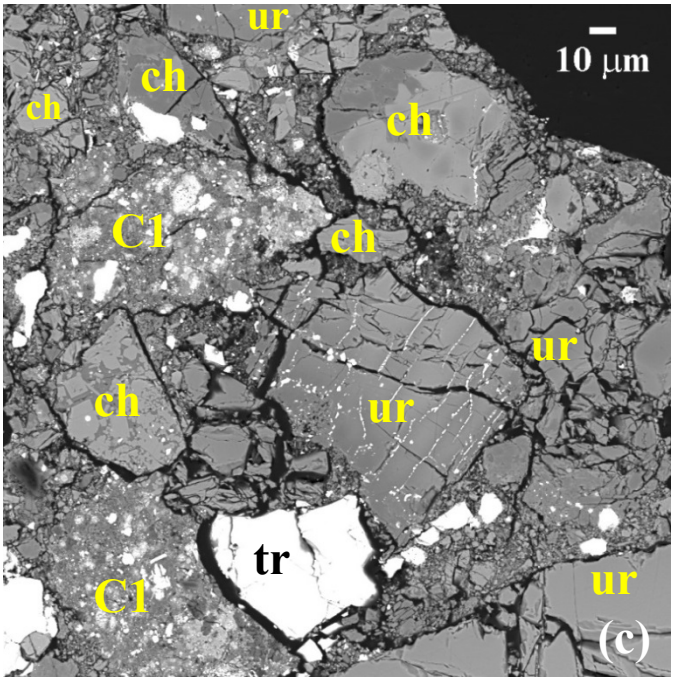
ur
10 μm
ch
ch
ch
C1
ch
ur
ch
ur
tr
C1
ur
(c)

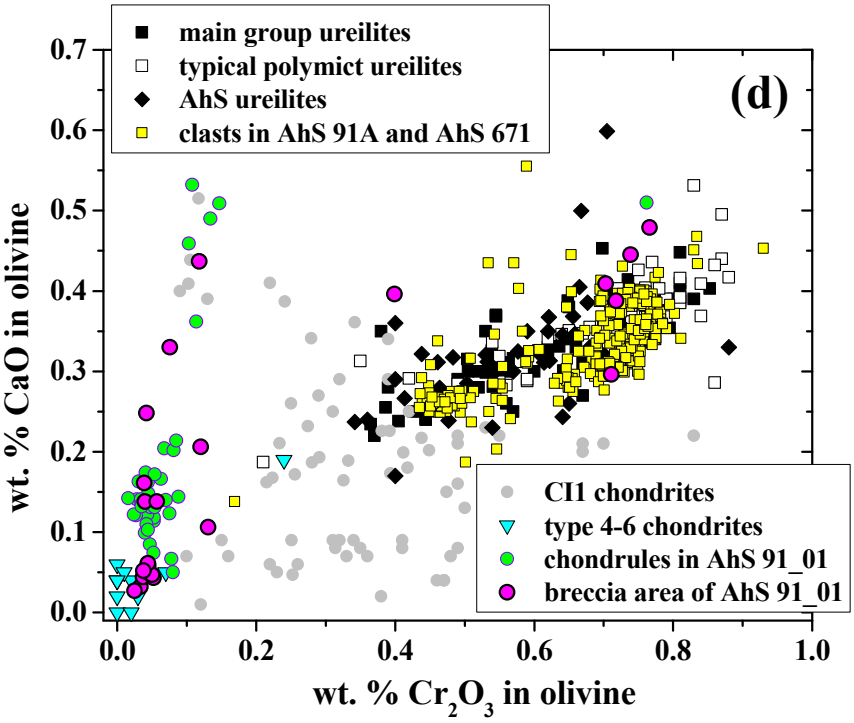
main group ureilites
typical polymict ureilites
AhS ureilites
clasts in AhS 91A and AhS 671
(d)
CI1 chondrites
type 4-6 chondrites
chondrules in AhS 91_01
breccia area of AhS 91_01
wt. % CaO in olivine
wt. % Cr2O3 in olivine
0.0
0.1
0.2
0.3
0.4
0.5
0.6
0.7
0.0
0.2
0.4
0.6
0.8
1.0

Fig. 19

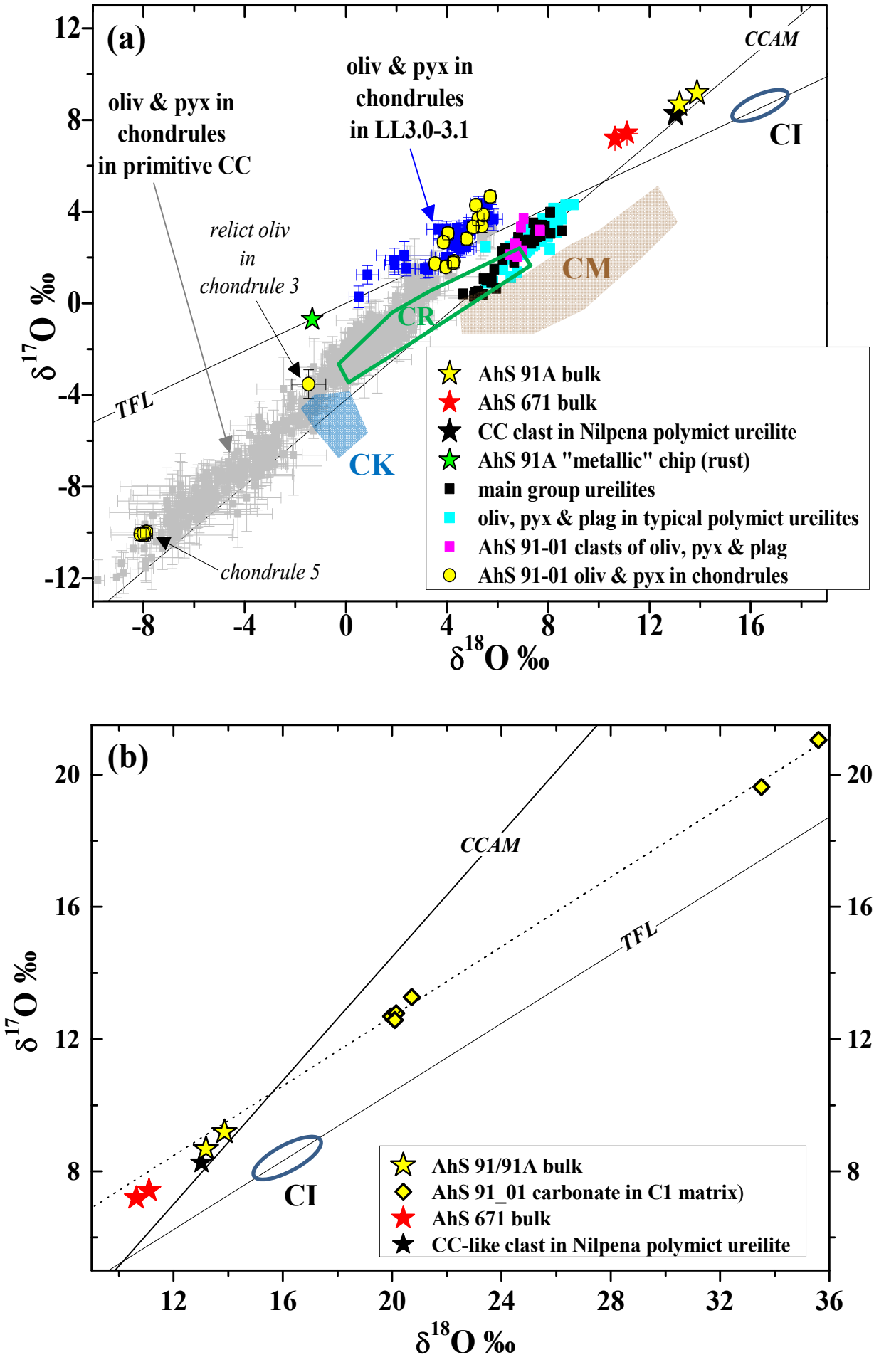
(a)
oliv & pyx in chondrules in primitive CC
oliv & pyx in chondrules in LL3.0-3.1
relict oliv in chondrule 3
chondrule 5
CCAM
CI
CM
CR
CK
TFL
AhS 91A bulk
AhS 671 bulk
CC clast in Nilpena polymict ureilite
AhS 91A "metallic" chip (rust)
main group ureilites
oliv, pyx & plag in typical polymict ureilites
AhS 91-01 clasts of oliv, pyx & plag
AhS 91-01 oliv & pyx in chondrules
δ17O ‰
δ18O ‰
(b)
CCAM
TFL
CI
AhS 91/91A bulk
AhS 91_01 carbonate in C1 matrix)
AhS 671 bulk
CC-like clast in Nilpena polymict ureilite
δ17O ‰
δ18O ‰

Fig. 20

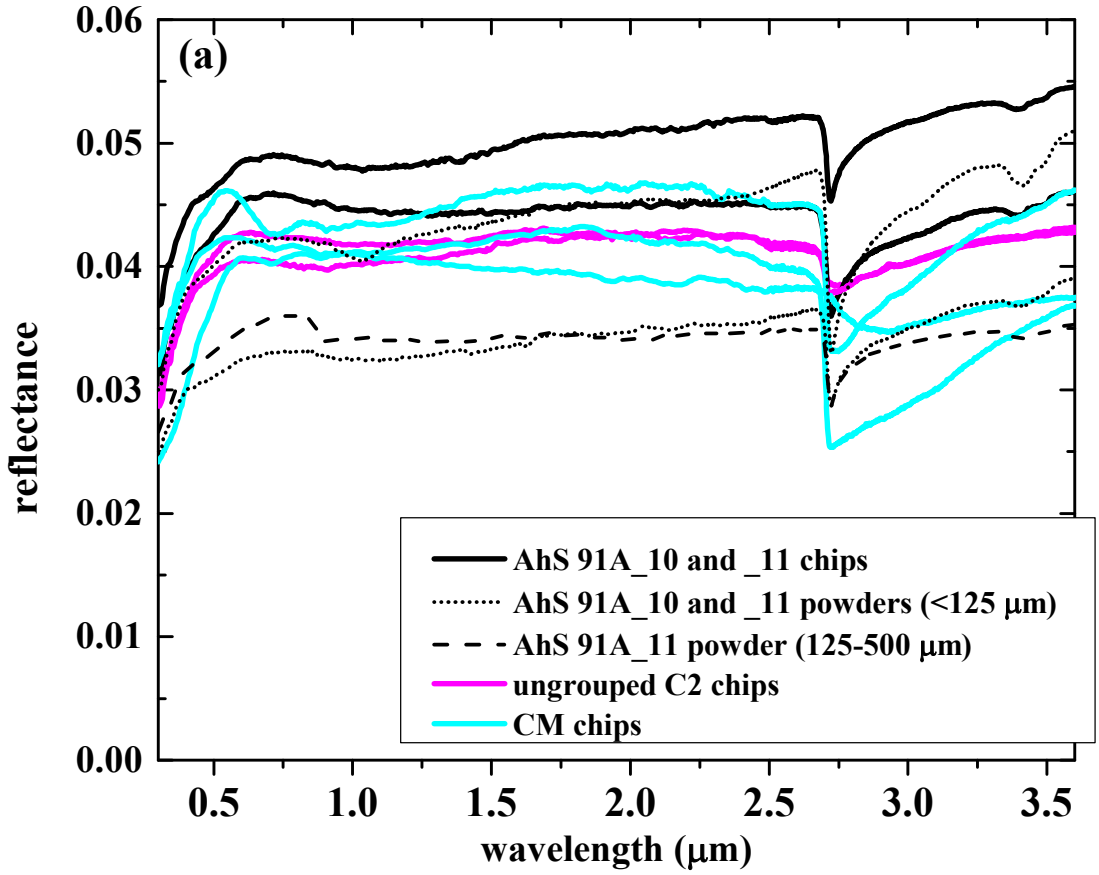
(a)
reflectance
wavelength (μm)
AhS 91A_10 and _11 chips
AhS 91A_10 and _11 powders (<125 μm)
AhS 91A_11 powder (125-500 μm)
ungrouped C2 chips
CM chips

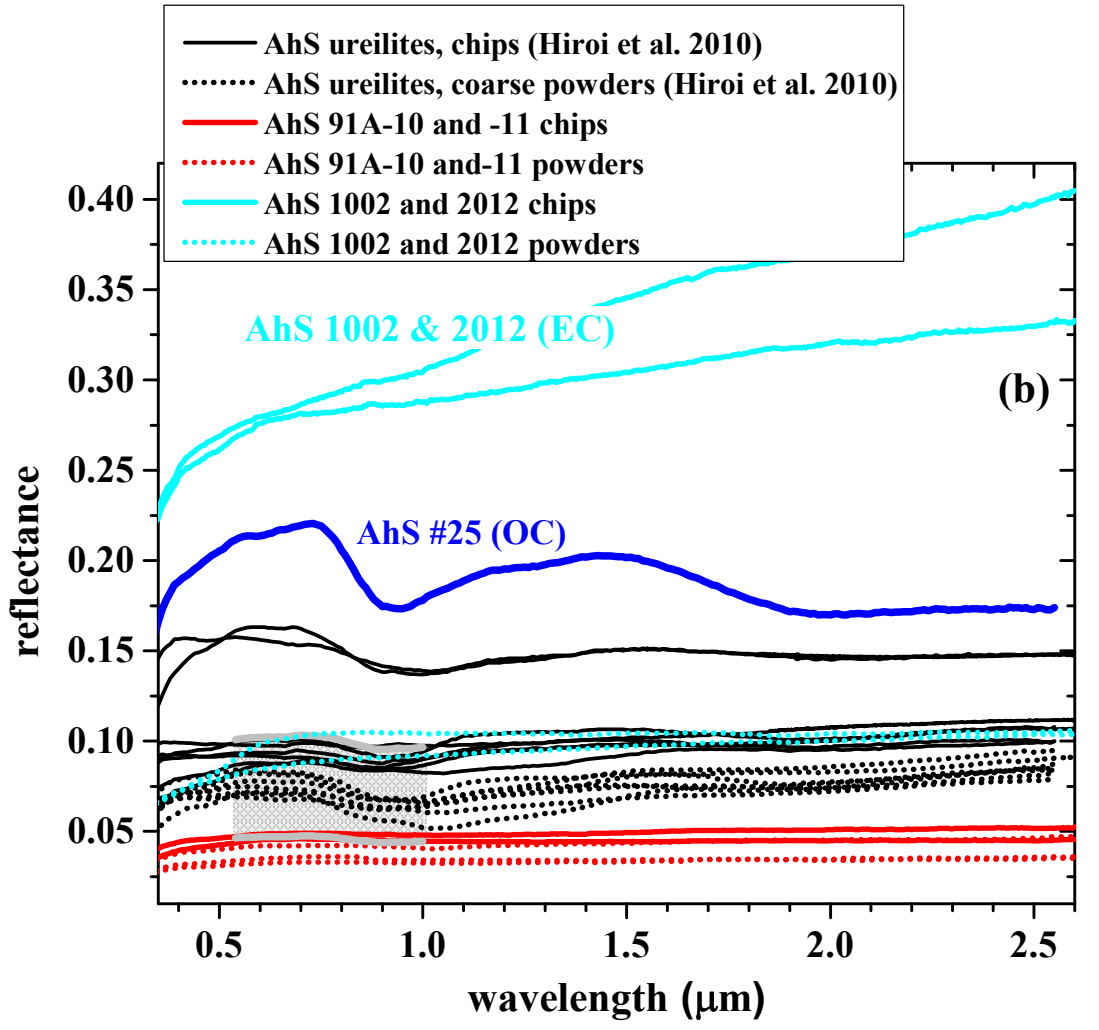
AhS ureilites, chips (Hiroi et al. 2010)
AhS ureilites, coarse powders (Hiroi et al. 2010)
AhS 91A-10 and -11 chips
AhS 91A-10 and-11 powders
AhS 1002 and 2012 chips
AhS 1002 and 2012 powders
AhS 1002 & 2012 (EC)
(b)
AhS #25 (OC)
reflectance
wavelength (μm)

Fig. 21

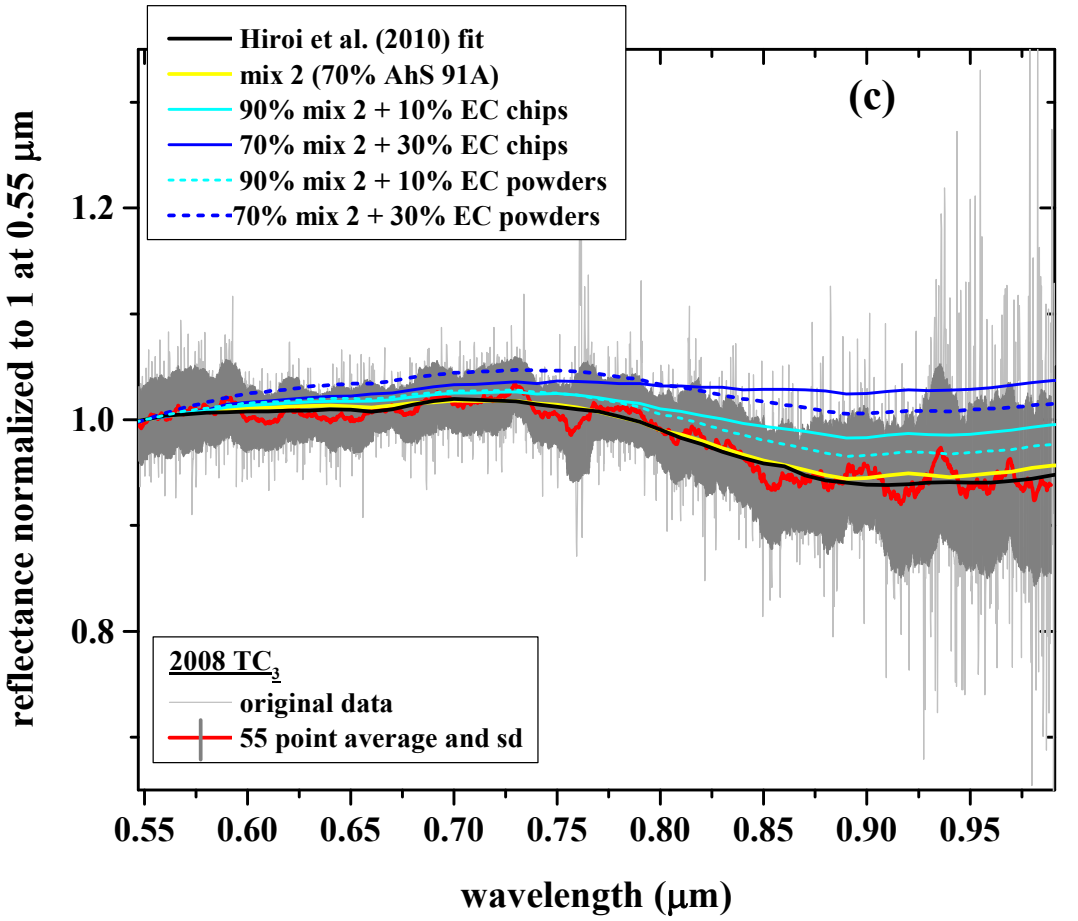
Hiroi et al. (2010) fit
mix 2 (70% AhS 91A)
90% mix 2 + 10% EC chips
70% mix 2 + 30% EC chips
90% mix 2 + 10% EC powders
70% mix 2 + 30% EC powders
(c)
2008 TC3
original data
55 point average and sd
reflectance normalized to 1 at 0.55 µm
wavelength (µm)

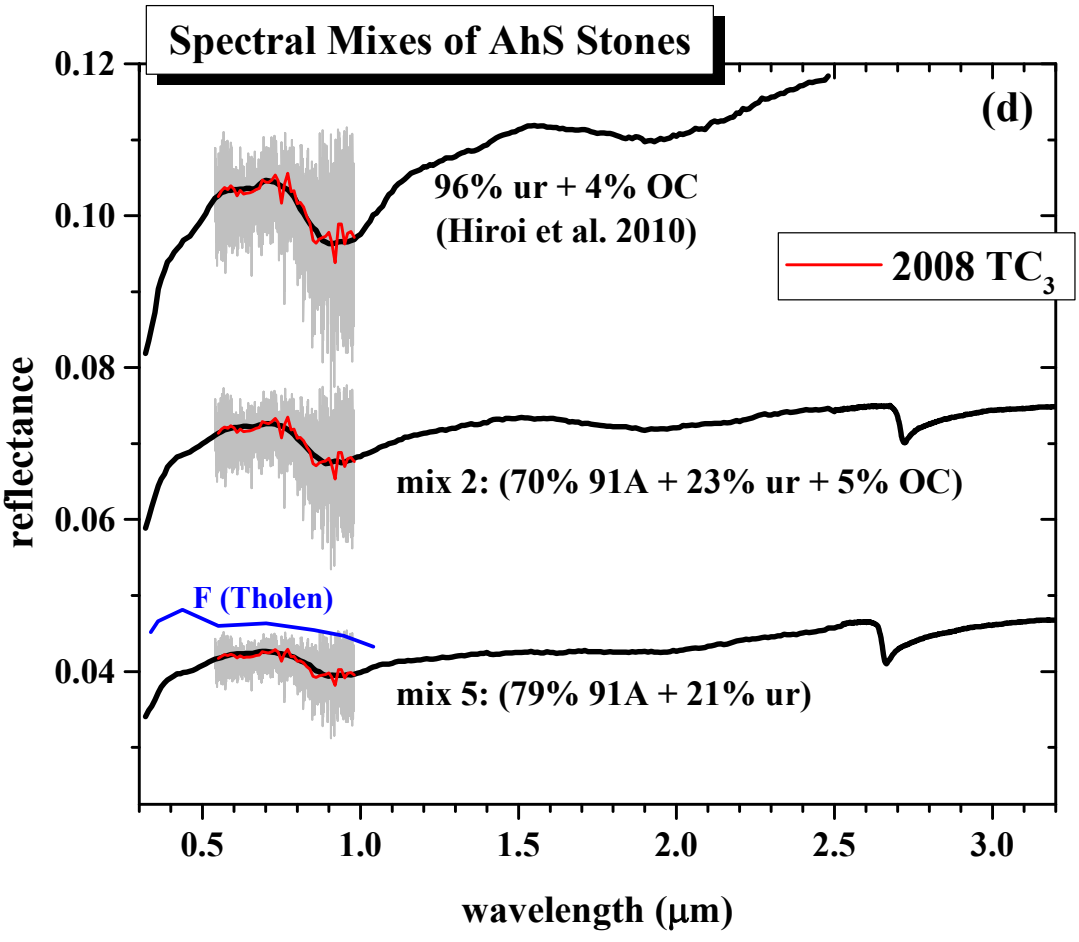
Spectral Mixes of AhS Stones
(d)
96% ur + 4% OC
(Hiroi et al. 2010)
2008 TC3
mix 2: (70% 91A + 23% ur + 5% OC)
F (Tholen)
mix 5: (79% 91A + 21% ur)
reflectance
wavelength (µm)

Fig. 21

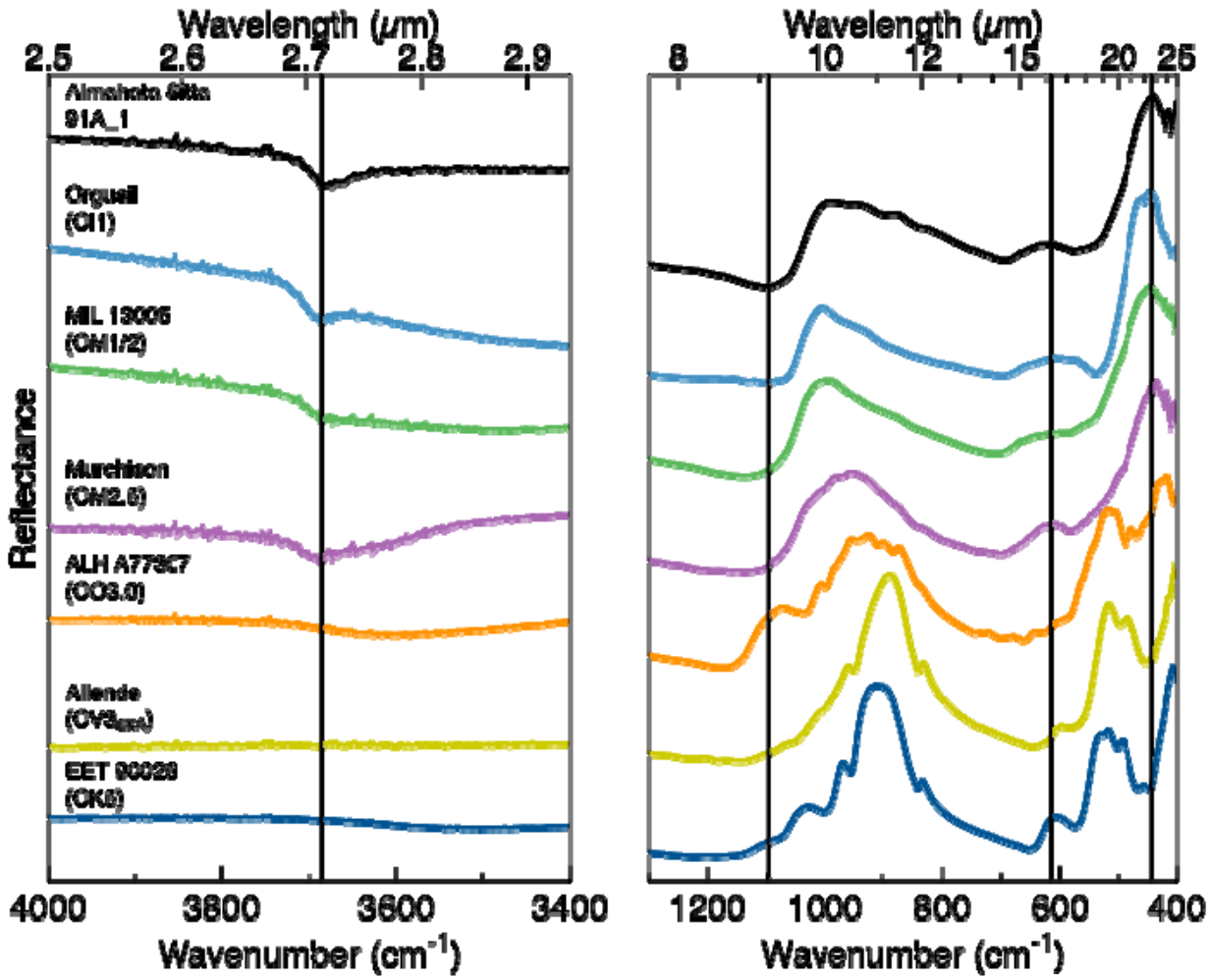
Wavelength (μm)
2.5
2.6
2.7
2.8
2.9
Almahata Sitta
91A_1
Orgueil
(CI1)
MIL 13005
(CM1/2)
Murchison
(CM2.6)
ALH A77307
(CO3.0)
Allende
(CV3oxA)
EET 92029
(CK5)
Reflectance
4000
3800
3600
3400
Wavenumber (cm-1)
Wavelength (μm)
8
10
12
15
20
25
1200
1000
800
600
400
Wavenumber (cm-1)

Fig. 22

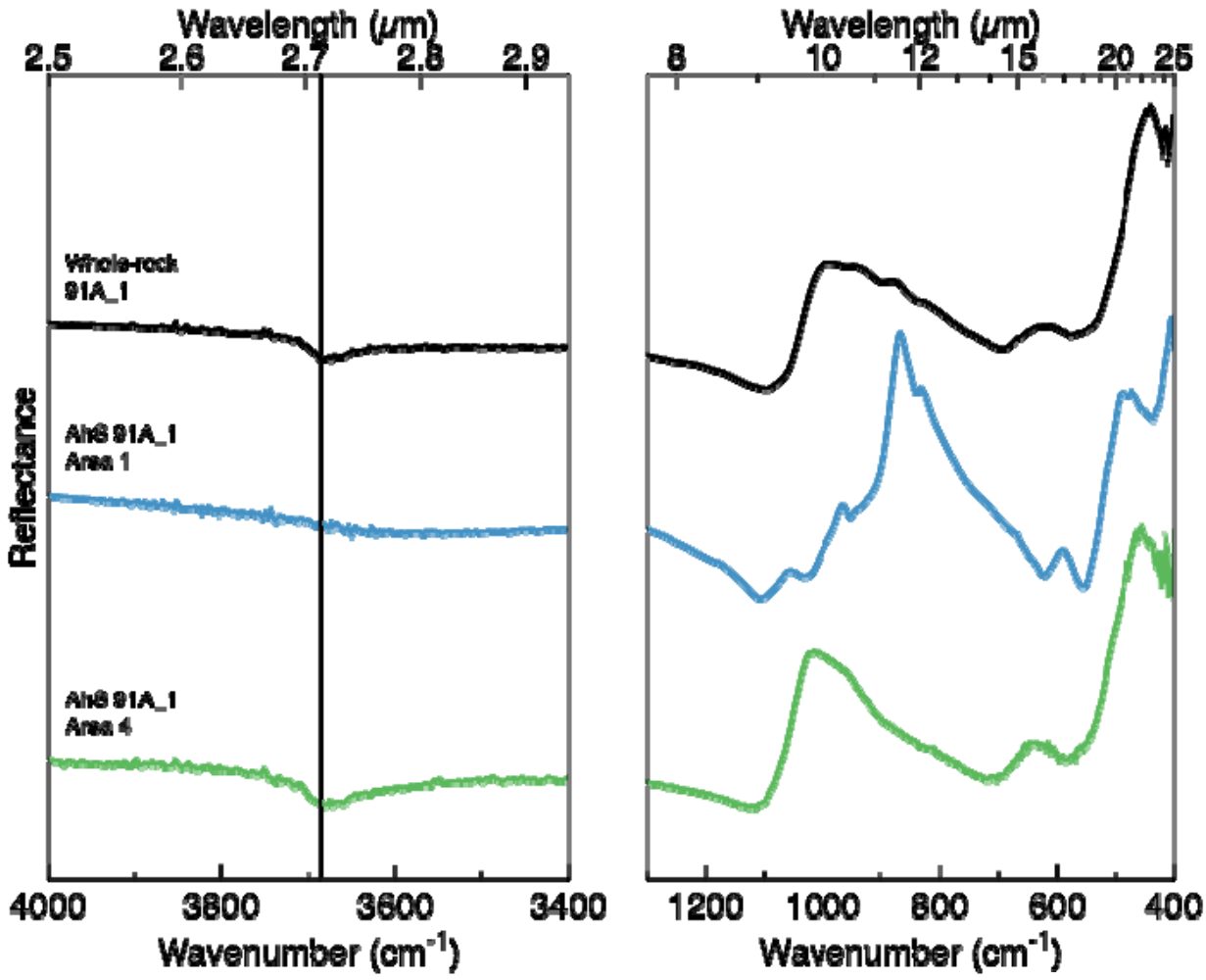
Wavelength (μm)
2.5
2.6
2.7
2.8
2.9
Whole-rock
91A_1
AhS 91A_1
Area 1
AhS 91A_1
Area 4
Reflectance
4000
3800
3600
3400
Wavenumber (cm-1)
Wavelength (μm)
8
10
12
15
20
25
1200
1000
800
600
400
Wavenumber (cm-1)

Fig. 23

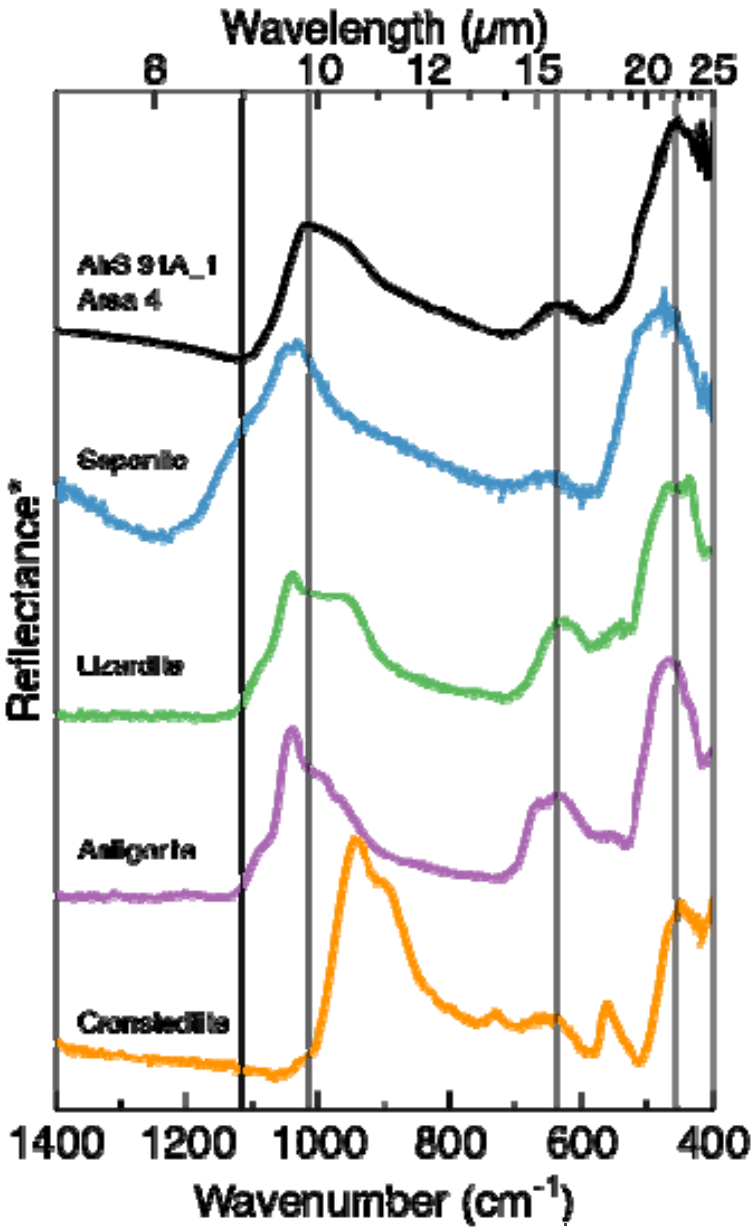
Wavelength (μm)
6
10
12
15
20
25
AlS 91A_1
Area 4
Saponite
Lizardite
Antigorite
Crondedite
Reflectance*
1400
1200
1000
800
600
400
Wavenumber (cm-1)

Fig. 24

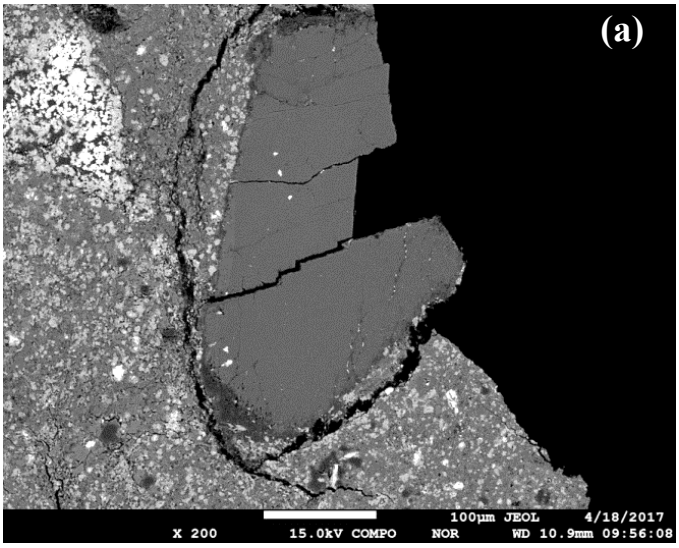
(a)
100µm JEOL 4/18/2017
X 200 15.0kV COMPO NOR WD 10.9mm 09:56:08

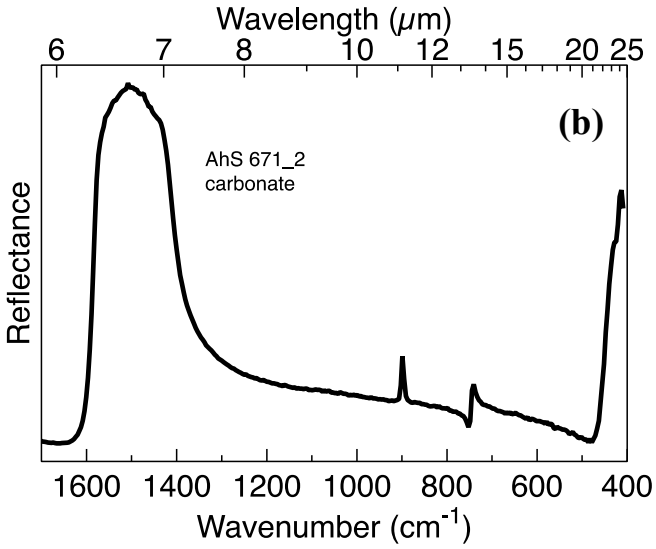
Wavelength (µm)
6 7 8 10 12 15 20 25
(b)
AhS 671_2
carbonate
Reflectance
1600 1400 1200 1000 800 600 400
Wavenumber (cm-1)

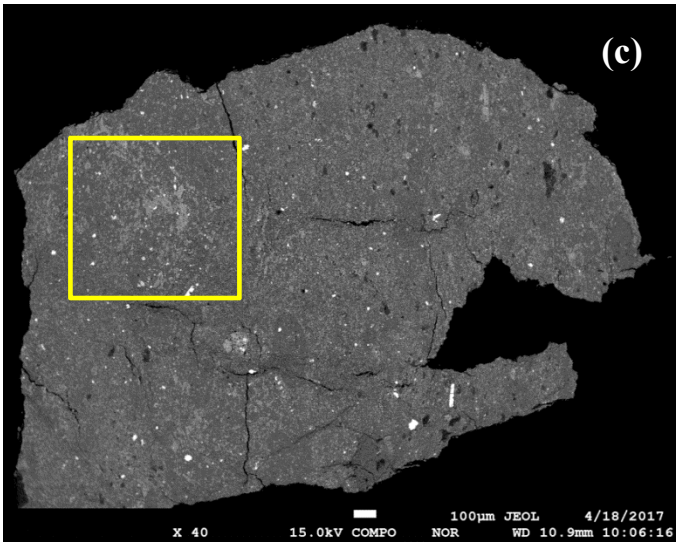
(c)
100µm JEOL 4/18/2017
X 40 15.0kV COMPO NOR WD 10.9mm 10:06:16

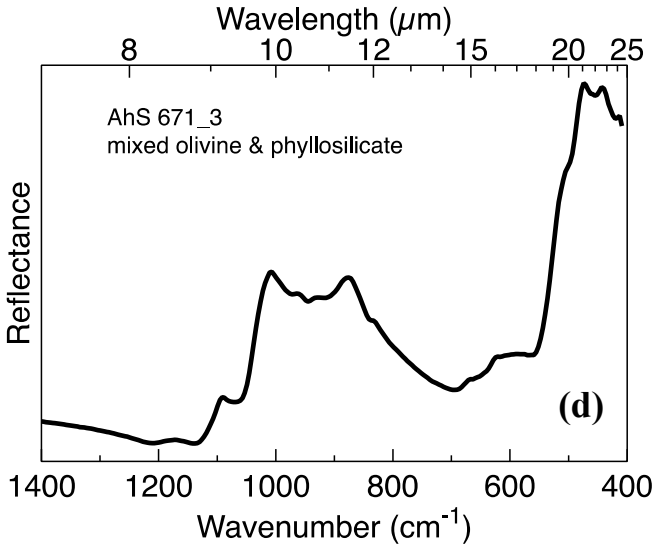
Wavelength (µm)
8 10 12 15 20 25
AhS 671_3
mixed olivine & phyllosilicate
Reflectance
(d)
1400 1200 1000 800 600 400
Wavenumber (cm-1)

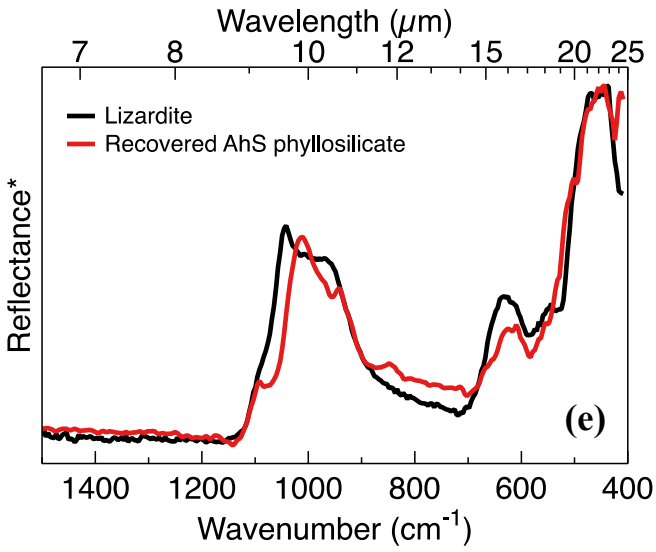
Wavelength (µm)
7 8 10 12 15 20 25
Lizardite
Recovered AhS phyllosilicate
Reflectance*
(e)
1400 1200 1000 800 600 400
Wavenumber (cm-1)

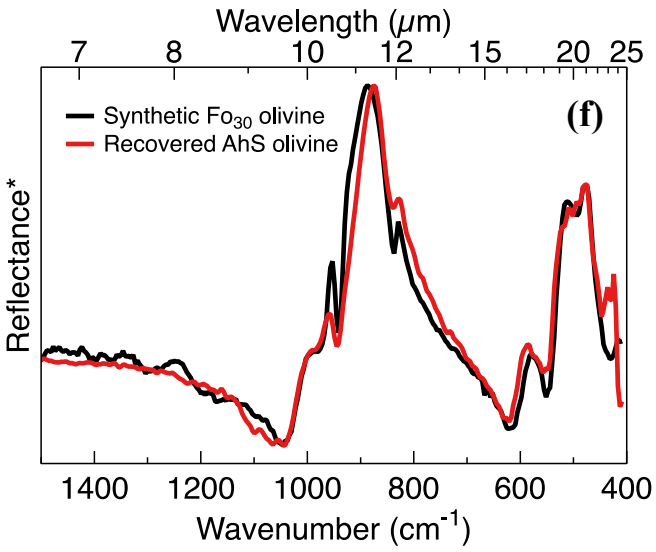
Wavelength (µm)
7 8 10 12 15 20 25
Synthetic Fo30 olivine
Recovered AhS olivine
(f)
Reflectance*
1400 1200 1000 800 600 400
Wavenumber (cm-1)

Fig. 25

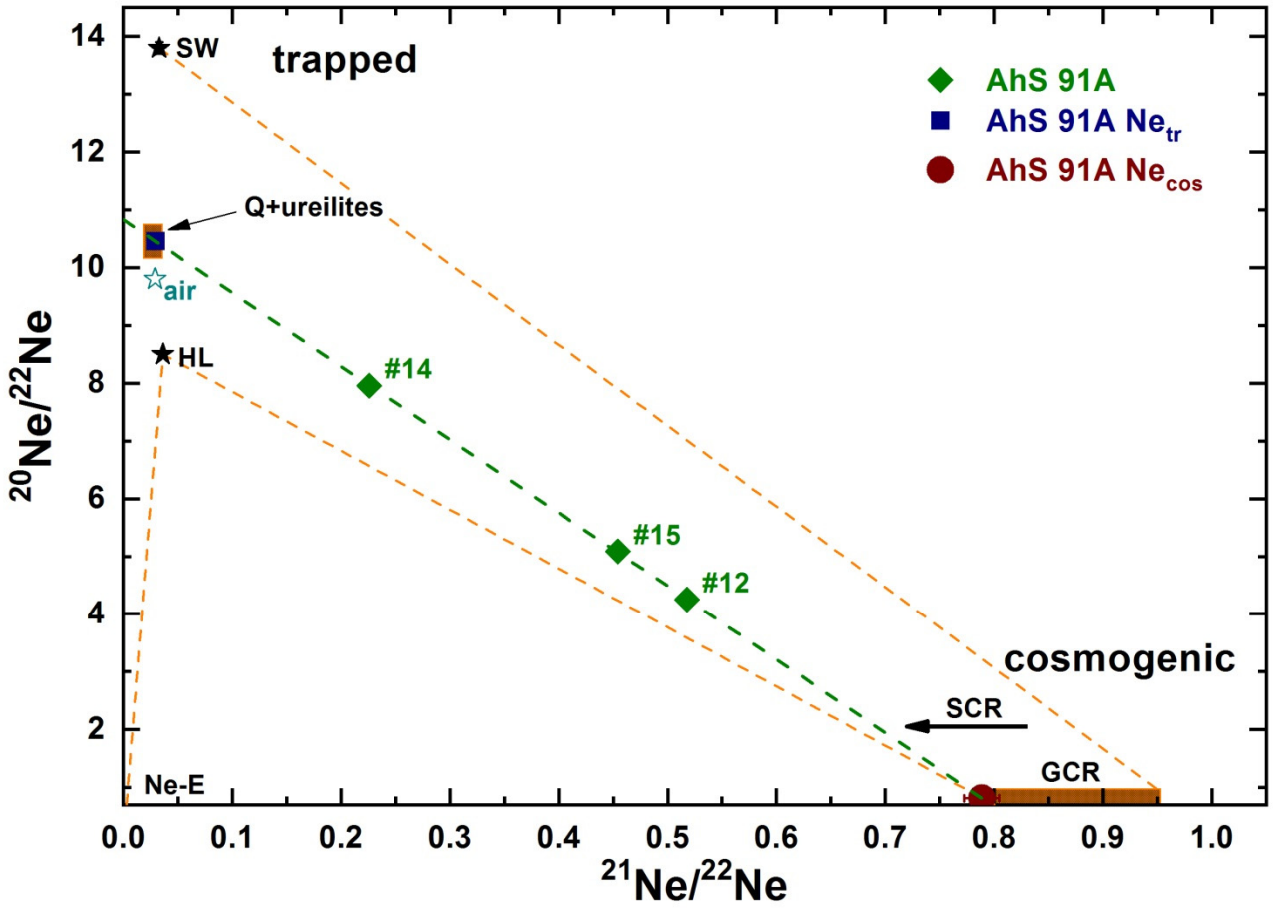
trapped
SW
AhS 91A
AhS 91A Ne$_{tr}$
AhS 91A Ne$_{cos}$
Q+ureilites
air
HL
#14
#15
#12
cosmogenic
SCR
GCR
Ne-E
^{20}Ne/^{22}Ne
^{21}Ne/^{22}Ne
0.0
0.1
0.2
0.3
0.4
0.5
0.6
0.7
0.8
0.9
1.0
2
4
6
8
10
12
14

Fig. 26

Table 1. Compositions of phases in C1 matrix of AhS 91A and AhS 671 from EMPA.

	phyllosilicate(s)*							Ca-rich silicate phase	fayalitic olivine**
	AhS 91A_01		AhS 91A_01		AhS 671_03	AhS 671_03		AhS 91A_01	AhS 671_03
	avg. (23)	*sd*	avg. (47)	*sd*	(1)	avg. (5)	*sd*	(1)	avg. (4)
SiO_2	39.7	*2.4*	39.3	*2.1*	36.2	37.7	*3.5*	48.9	30.4
TiO_2	bdl		0.04	*0.04*	0.03	bdl		bdl	0.07
Al_2O_3	3.8	*0.5*	2.6	*1.0*	4.7	4.1	*0.3*	4.1	0.10
Cr_2O_3	1.3	*0.1*	0.90	*0.37*	1.1	0.72	*0.23*	0.39	0.20
FeO	11.8	*0.7*	13.2	*2.0*	14.6	17.9	*1.3*	7.4	50.5
MgO	31.7	*2.2*	29.8	*2.3*	30.8	24.2	*2.7*	17.7	17.6
MnO	0.14	*0.02*	0.16	*0.03*	0.07	0.19	*0.04*	0.33	0.23
CaO	0.18	*0.06*	0.25	*0.22*	0.04	0.40	*0.12*	15.0	0.13
Na_2O	0.44	*0.18*	0.51	*0.27*	0.13	0.15	*0.04*	2.7	0.05
K_2O	0.07	*0.05*	0.07	*0.03*	bdl	0.05	*0.06*	bdl	bdl
P_2O_5	0.08	*0.03*	0.07	*0.04*	bdl	0.56	*0.20*	na	0.73
NiO	0.04	*0.02*	0.12	*0.10*	1.3	1.2	*0.3*	0.10	0.51
Total	89.2	*1.8*	87.0	*1.4*	89.0	87.2	*5.1*	96.6	100.5
FeS[§]	0.05	*0.05*	0.26	*0.31*	2.4	0.3	*0.1*	1.2	0.50

*Analyses of phyllosilicates are broad beam (2 μm) analyses obtained in profiles across matrix areas, and were filtered to remove analyses with high CaO (assumed to include the Ca-rich phase), FeO (assumed to include magnetite and/or fayalite). They appear to be dominantly mixtures of serpentine and saponite but may include minor phases.

**Olivine is porous and has many tiny inclusions of unidentified phases, hence stoichiometry is not perfect for olivine.

§S was measured as SO_3; analyses were re-calculated assuming all S was in FeS and adjusting FeO accordingly.

bdl = below detection limit; na = not analyzed.

Table 2. Compositions of carbonates in AhS 91A and AhS 671 from EMPA.

	large breunnerite AhS 91A		large dolomite AhS 91A		large breunnerite AhS 671		rim on breunnerite	small breunnerite
	avg. (111)	*sd*	avg. (49)	*sd*	avg. (87)	*sd*		
FeO	19.3	*0.9*	4.8	*0.6*	18.1	*1.6*	9.1	9.2
MgO	27.1	*1.1*	18.3	*1.2*	28.8	*1.0*	40.0	39.7
MnO	6.4	*1.5*	2.0	*0.5*	5.5	*1.9*	0.8	1.2
CaO	1.0	*0.3*	28.4	*1.6*	0.9	*0.5*	0.22	0.19
CO_2^*	46.2	*0.3*	46.5	*0.2*	46.7	*0.3*	49.9	49.8
Total	100.0		100.0		100.0		100.0	100.0
magnesite	0.64	*0.02*	0.43	*0.03*	0.67	*0.02*	0.88	0.87
siderite	0.26	*0.01*	0.06	*0.01*	0.24	*0.02*	0.11	0.11
rhodochrosite	0.09	*0.02*	0.03	*0.01*	0.07	*0.03*	0.01	0.02
calcite	0.01	*0.01*	0.48	*0.03*	0.02	*0.01*	0.00	0.00

*CO_2 was not analyzed. Analyses were re-calculated assuming that CO_2 = 100% - analytical total, and then checked for carbonate stoichiometry. Concentrations of Si, Al, Cr, Ti and Na were near or below detection limit.

Table 3. Compositions of magnetite in AhS 91A and AhS 671 from EMPA.

	AhS 671_02		AhS 91A_02	
	avg (6)	*sd*	avg (5)	*sd*
SiO_2	0.11	*0.07*	0.08	*0.04*
TiO_2	0.02	*0.02*	0.02	*0.00*
Al_2O_3	bdl		bdl	
Cr_2O_3	0.08	*0.06*	0.08	*0.01*
FeO	30.9	*0.2*	30.8	*0.1*
Fe_2O_3	68.8	*0.4*	68.5	*0.2*
MgO	0.22	*0.26*	0.04	*0.04*
MnO	0.27	*0.25*	0.02	*0.02*
CaO	bdl		bdl	
NiO	0.06	*0.04*	0.06	*0.03*
Total	100.5		99.6	

Analyses re-calculated assuming molar $Fe^{2+}/Fe^{3+} = 2/3$.

Table 4. Representative compositions of ureilitic mineral clasts in AhS 91A and AhS 671 from EMPA

	1	2	3	4	5	6	7	8	9	10	11	12	13	14	15	16	17	18
	ol core avg. (4)	ol core avg. (11)	ol core avg. (49)	ol core avg. (11)	ol core (1)	ol reduc. rim	ol reduc. rim	pyx avg. (12)	pyx avg. (8)	pyx avg. (7)	pyx avg. (6)	pyx avg. (27)	pyx avg. (1)	pyx avg. (5)	pyx avg. (7)	plag avg. (7)	plag avg. (3)	plag avg. (4)
SiO_2	38.6	38.7	39.0	39.7	40.3	40.4	42.2	54.1	54.9	54.3	55.9	55.8	56.1	55.8	60.0	67.5	68.2	59.5
TiO_2	bdl	bdl	bdl	bdl	bdl	bdl	bdl	0.07	0.05	0.10	0.05	0.07	0.15	0.16	0.06	bdl	0.10	bdl
Al_2O_3	bdl	bdl	bdl	bdl	bdl	bdl	bdl	1.01	0.56	0.92	0.38	0.46	0.99	1.16	0.11	20.2	21.4	25.8
Cr_2O_3	0.71	0.47	0.76	0.74	0.57	0.44	0.17	1.20	1.07	1.17	1.07	1.10	1.03	0.97	0.02	bdl	bdl	bdl
FeO	22.6	20.1	19.5	15.0	12.0	9.8	0.93	12.9	13.2	11.3	11.0	9.3	7.5	7.4	0.39	0.05	0.06	0.39
MgO	38.7	39.8	41.2	44.6	47.4	47.9	55.2	24.9	26.2	25.5	28.4	28.6	29.4	31.2	39.5	0.01	0.01	0.11
MnO	0.41	0.41	0.44	0.45	0.5	0.49	0.26	0.39	0.39	0.42	0.42	0.46	0.53	0.56	0.10	bdl	bdl	0.02
CaO	0.38	0.26	0.40	0.32	0.44	0.26	0.14	4.9	4.0	5.1	3.4	4.2	5.2	2.4	0.45	0.62	1.1	7.2
Na_2O	bdl	bdl	bdl	bdl	bdl	bdl	bdl	0.05	0.04	0.06	0.05	0.02	0.04	0.04	0.02	11.1	10.6	7.3
NiO	bdl	bdl	bdl	bdl	bdl	bdl	bdl	bdl	bdl	bdl	bdl	bdl	bdl	bdl	bdl	na	bdl	bdl
K_2O	na	na	na	na	na	na	na	na	na	na	na	na	na	na	100.7	0.56	0.72	0.06
Total	101.4	99.7	101.3	100.8	101.2	99.3	98.9	99.5	100.4	98.9	100.7	100.0	100.9	99.7	0.01	100.0	102.0	100.4
Mg#	75.3	78.0	79.0	84.1	87.5	89.7	99.1	77.5	77.9	80.0	82.2	84.5	87.5	88.3	99.5			
Wo								9.8	7.9	10.3	6.6	8.2	9.9	4.6	0.8			
An																2.9	5.2	35.2
Or																3.2	4.1	0.4

Numbers in parentheses are number of analyses in the average.

Mg# = 100×molar MgO/(MgO+FeO); Wo = 100×molar CaO/(CaO+FeO+MgO); An = 100×molar CaO/(CaO+Na_2O+K_2O); Or = 100×molar K_2O /(CaO+Na_2O+K_2O).

ol = olivine; pyx = pyroxene; red = reduction; plag = plagioclase.

Table. 5. Compositions of metal and sulfide in metal-sulfide clasts in AhS 91A and AhS 671 from EMPA.

	clast[1]	chondrule #4[2]		clast[3]			metal grain with inclusions[4]		
	ureilitic kamacite	kamacite avg. (2)	troilite	kamacite avg. (6)	taenite avg. (3)	troilite	kamacite avg. (15)	*sd*	niningerite inclusions avg. (2)
Mg	bdl	bdl	bdl	bdl	bdl	bdl	bdl		12.0
Si	0.47	0.05	0.04	0.03	0.03	0.03	3.0	*0.1*	0.27
P	0.24	bdl	bdl	bdl	bdl	bdl	0.12	*0.01*	bdl
S	bdl	bdl	36.1	bdl	bdl	37.0	bdl		40.9
Ca	bdl	bdl	bdl	bdl	bdl	bdl	bdl		1.3
Ti	bdl	bdl	bdl	bdl	bdl	bdl	bdl		0.06
V	bdl	bdl	bdl	bdl	bdl	bdl	bdl		bdl
Cr	0.23	0.02	0.03	0.03	0.08	0.04	bdl		1.6
Mn	bdl	bdl	bdl	bdl	bdl	bdl	bdl		4.6
Fe	92.5	91.9	59.2	93.0	79.0	61.2	87.8	*0.9*	36.7
Co	0.36	0.46	0.19	0.49	0.20	bdl	0.33	*0.02*	0.02
Ni	4.2	6.9	2.5	5.8	19.8	0.24	8.2	*0.1*	0.26
Total	98.0	99.3	98.0	99.4	99.1	98.5	99.5	*1.0*	97.7

[1,4] AhS 91A_09

[2,3] AhS 91_01

Table 6. Compositions of phases in chondrules in AhS 91_01 from EMPA.

	chondrule 2						chondrule 3				chondrule 4				chondrule 5			
	xtal cores oliv avg. (24)	*sd*	xtal rim oliv	xtal rim oliv	opx avg. (8)	*sd*	oliv avg. (8)	*sd*	opx avg. (18)	*sd*	oliv avg. (10)	*sd*	opx avg. (28)	*sd*	oliv	oliv	opx avg. (3)	*sd*
SiO_2	41.6	*0.3*	39.5	39.8	58.7	*0.2*	39.0	*0.3*	58.0	*0.4*	39.0	*0.3*	56.9	*0.7*	42.1	40.5	58.4	*0.1*
TiO_2	bdl		bdl	bdl	0.10	*0.02*	bdl		0.04	*0.02*	bdl		0.04	*0.02*	bdl	bdl	0.24	*0.05*
Al_2O_3	bdl		bdl	bdl	0.59	*0.08*	bdl		0.34	*0.15*	0.04	*0.06*	0.38	*0.25*	0.16	0.08	1.41	*0.14*
Cr_2O_3	0.05	*0.02*	0.04	0.06	0.67	*0.05*	0.05	*0.01*	0.60	*0.14*	0.15	*0.18*	0.72	*0.16*	0.11	0.11	0.28	*0.01*
FeO	5.1	*1.4*	16.8	14.9	1.3	*0.2*	18.7	*1.5*	3.5	*0.7*	19.5	*1.7*	7.5	*0.7*	0.93	10.5	0.65	*0.04*
MgO	53.2	*1.2*	43.5	44.9	38.1	*0.2*	41.7	*1.2*	36.4	*0.7*	41.1	*1.5*	33.5	*1.0*	55.8	48.4	38.3	*0.1*
MnO	0.08	*0.02*	0.33	0.24	0.09	*0.01*	0.46	*0.03*	0.39	*0.09*	0.52	*0.09*	0.47	*0.18*	0.04	0.17	0.06	*0.01*
CaO	0.14	*0.04*	0.13	0.15	0.36	*0.05*	0.13	*0.01*	0.30	*0.10*	0.09	*0.03*	0.50	*0.28*	0.53	0.36	0.52	*0.03*
Na_2O	bdl		bdl	bdl	bdl		bdl		0.05	*0.07*	bdl		0.01	*0.01*	bdl	bdl	bdl	
NiO	bdl		bdl	0.05	bdl		0.06	*0.04*	0.04	*0.03*	bdl		0.04	*0.02*	bdl	bdl	bdl	
Total	100.2		100.3	100.1	99.9		100.1		99.7		100.4		100.0		99.7	100.1	99.9	
Mg#	94.9	*1.5*	82.2	84.3	98.2	*0.2*	79.9	*1.7*	94.9	*1.0*	78.9	*2.06*	88.9	*1.1*	99.1	89.2	99.1	*0.1*
Wo					0.7	*0.1*			0.6	*0.2*			1.0	*0.6*			1.0	*0.0*

Numbers in parentheses are number of analyses in the average.

Mg# = 100×molar MgO/(MgO+FeO); Wo = 100×molar CaO/(CaO+FeO+MgO); An = 100×molar CaO/(CaO+Na_2O+K_2O); Or = 100×molar K_2O /(CaO+Na_2O+K_2O).

xtal = crystal; oliv = olivine; opx = orthopyroxene.

Table 7. Bulk oxygen isotope compositions for AhS 91A and AhS 671

Sample		δ17O'	se	δ18O'	se	Δ^{17}O'	se	n=
AhS 91A_08	CC-like	9.185	0.008	13.872	0.016	1.872	0.004	6
AhS 91A_08	CC-like	8.676	0.004	13.189	0.006	1.712	0.005	6
average		8.931		13.531		1.792		
						0.113		
AhS 91A_08	metallic?	-0.671	0.005	-1.263	0.007	-0.004	0.005	6
AhS 91A_08	metallic?	-0.748	0.003	-1.399	0.006	-0.01	0.003	6
average		-0.710		-1.331		-0.007		
AhS 671 01_A.1	CC-like	7.42	0.007	11.105	0.009	1.556	0.009	10
AhS 671 01_A.2	CC-like	7.195	0.003	10.639	0.012	1.577	0.007	7
average		7.308		10.872		1.567		

se = standard error.

Table 8. Oxygen isotope compositions of phases in AhS 91_01 analyzed by SIMS.*

	N	$\delta^{18}O$	$\delta^{18}O$ unc.	$\delta^{17}O$	$\delta^{17}O$ unc.	$\Delta^{17}O$	$\Delta^{17}O$ unc.
Ureilitic							
AhS 91_1 Area 1 (olivine)	4	6.73	0.38	2.18	0.25	-1.32	0.19
AhS 91_1 Area 6 (olivine)	2	7.68	0.36	3.18	0.28	-0.81	0.23
AhS 91_1 Area 6 (pigeonite)	2	6.97	0.36	3.50	0.41	-0.12	0.33
AhS 91_1 Area 7 (plagioclase)	1	7.02	0.39	3.16	0.34	-0.49	0.28
AhS 91_1 Area 9 (orthopyroxene)	2	6.71	0.36	2.53	0.28	-0.96	0.23
Chondrules							
AhS 91_1 Area 2 chondrule Ol	4	4.92	0.69	3.35	0.33	0.80	0.23
AhS 91_1 Area 2 chondrule pyx	1	3.86	0.39	2.67	0.34	0.66	0.28
Mean AhS 91_1 Area 2 chondrule	5	4.71	0.71	3.22	0.40	0.77	0.21
AhS 91_1 Area 3 chondrule Ol	1	-1.47	0.75	-3.53	0.66	-2.76	0.41
AhS 91_1 Area 3 chondrule pyx	3	5.42	0.46	4.26	0.50	1.44	0.43
AhS 91_1 Area 4 chondrule Ol	2	4.16	1.30	2.27	1.11	0.10	0.45
AhS 91_1 Area 4 chondrule pyx	3	4.16	0.39	1.73	0.26	-0.44	0.20
Mean AhS 91_1 Area 4 chondrule	5	4.16	0.53	1.94	0.49	-0.22	0.33
AhS 91_1 Area 5 chondrule Ol	2	-8.04	0.37	10.09	0.28	-5.91	0.23
AhS 91_1 Area 5 chondrule pyx	1	-7.89	0.39	-9.98	0.34	-5.88	0.28
Mean AhS 91_1 Area 5 chondrule	3	-7.99	0.35	10.06	0.26	-5.90	0.20
Carbonate (breunnerite)							
AhS 91_1 Area 8 carbonate core	3	20.07	0.36	12.68	0.26	2.24	0.22
AhS 91_1 Area 8 carbonate intermediate	1	20.71	0.23	13.27	0.25	2.50	0.27
AhS 91_1 Area 8 carbonate rim 1	1	35.61	0.23	21.05	0.25	2.53	0.27
AhS 91_1 Area 8 carbonate rim 2	1	33.51	0.23	19.62	0.25	2.20	0.27
Mean AhS 91_1 Area 8 carbonate	6					2.33	0.21

*Analysis areas are marked in figure 18a.
unc. = uncertainty.

Table 9. Helium and Ne concentrations (in 10^{-8} cm^3/g) and isotopic ratios in three fragments of AhS 91A.

#	mass	^4He	$^3He/^4He$	^{20}Ne	$^{20}Ne/^{22}Ne$	$^{21}Ne/^{22}Ne$	$^{21}Ne_{cos}$
	mg		x 10000				
12	14.94±0.01	6505±50	11.42±0.10	21.62±0.15	4.25±0.03	0.518±0.003	2.579±0.019
14	7.79±0.01	8699±88	6.19±0.07	54.7±0.4	7.96±0.05	0.2258±0.0013	1.394±0.016
15	6.88±0.01	5922±48	9.01±0.08	21.83±0.20	5.08±0.05	0.454±0.003	1.887±0.017

Table 10. Argon concentrations (in 10^{-8} cm^3/g) and isotopic ratios in three fragments of AhS 91A.

#	^{36}Ar	$^{36}Ar/^{38}Ar$	$^{40}Ar/^{36}Ar$	$^{38}Ar_{cos}$	$^{40}Ar_{rad}$
12	83.3±1.0	5.204±0.023	27.6±0.4	0.45±0.09	2300±43
14	1064±18	5.302±0.022	1.59±0.03	1.4±1.1	1692±46
15	114.5±1.9	5.310±0.022	14.5±0.3	n.d.	1660±46

Table 11. Krypton concentrations and isotopic ratios in three fragments of AhS 91A.

#	^{84}Kr	$^{78}Kr/^{84}Kr$	$^{80}Kr/^{84}Kr$	$^{82}Kr/^{84}Kr$	$^{83}Kr/^{84}Kr$	$^{86}Kr/^{84}Kr$
	10^{-10} cm^3/g			$^{84}Kr = 100$		
12	88.0±0.7	0.608±0.005	3.994±0.026	20.22±0.11	20.08±0.18	31.23±0.17
14	272.3±2.3	0.599±0.005	3.873±0.027	19.97±0.12	19.90±0.09	30.33±0.15
15	99.6±0.9	0.593±0.006	4.04±0.03	20.12±0.14	20.05±0.18	30.73±0.22

Table 12. Xenon concentrations and isotopic ratios in three fragments of AhS 91A.

#	^{132}Xe	$^{124}Xe/^{132}Xe$	$^{126}Xe/^{132}Xe$	$^{128}Xe/^{132}Xe$	$^{129}Xe/^{132}Xe$	$^{130}Xe/^{132}Xe$	$^{131}Xe/^{132}Xe$	$^{134}Xe/^{132}Xe$	$^{136}Xe/^{132}Xe$
	10^{-10} cm^3/g				$^{132}Xe = 100$				
12	108.8±2.6	0.466±0.004	0.412±0.004	8.14±0.06	105.1±1.0	16.08±0.10	81.9±0.5	38.51±0.29	32.40±0.22
14	122.5±2.9	0.439±0.005	0.389±0.006	7.97±0.06	103.4±0.6	15.86±0.10	81.0±0.4	38.11±0.22	31.81±0.17
15	113.5±2.8	0.453±0.008	0.421±0.009	8.16±0.08	106.7±1.2	16.24±0.15	82.6±0.8	38.5±0.4	32.4±0.3

Table 13. Model production rates P_x (Leya & Masarik, 2009) for ^{3}He and ^{21}Ne assuming chemistry to be (i) ureilitic (Welten et al. 2010) and (ii) CI chondritic (Lodders and Fegley, 1998) and calculated as an average over the expected shielding depths in 2008 TC_3. Two production rate and CRE age (T_x) sets are given.

	P_3	P_{21}	P_3	P_{21}	
	ureilitic		CI chondritic		
	1.62	0.394	1.52	0.220	
	T_3	T_{21}	T_3	T_{21}	$\mathbf{T_{21,\,av}}$
	ureilitic		CI chondritic		
12	4.6	6.6	4.9	12.0	**9.3**
14	3.3	3.5	3.5	6.5	**5.0**
15	3.3	4.8	3.5	8.7	**6.8**

Production rates P_x in 10^{-8} $cm^3/(g \times Ma)$. Exposure ages T_x in Ma.

Table 14. Physical Properties of AhS 91A_18 and AhS 91A_19

	AhS 91A_18	AhS 91A_19	AhS 91A_(18+19)
mass	130 ± 2 mg	65.5 ± 2 mg (calculated)	195.5 ± 2 mg
bulk volume	0.0558 ± 0.0012 cm^3	0.0274 ± 0.0007 cm^3	0.0832 ± 0.0014 cm^3 (calculated)
bulk density = mass/bulk volume	2.330 ± 0.060 g/cm^3	2.391 ± 0.097 g/cm^3	2.350 ± 0.046 g/cm^3 (calculated)
grain volume			0.053 ± 0.0023 cm^3
grain density = mass/grain volume			3.686 ± 0.161 g/cm^3
porosity = [1-(bulk density/grain density)] x 100%			(36.2 ± 3.0) %

Table 15. Classification of Almahata Sitta Non-Ureilites (#s of stones).

	all UoK (16 stones)[1,2]		non UoK (48 stones)[3,4]	
E-meteorites	8		40	
EH		4		9
EL		3		29
unique E-achondrites		1		2
Ordinary Chondrites	5		6	
H		3		4
L		1		1
LL		1		1
Carbonaceous Chondrites	3		1	
C1-C2 hydrous		3		0
metal-rich		0		1
Rumuruti-type chondrites	0		1	1

1) Goodrich et al. 2018; 2) Zolensky et al. (2010); 3) Horstmann & Bischoff (2014); 4) Bischoff et al. (2015a, 2016, 2018b, 2019).

Table 16. Properties of model spectral mixtures shown in Figure 21c,d

	% 91A	% OC	% ureilites	RELAB files	AhS stone	type	state	incidence angle
mix 2	70.2			C1MT320	#91A	CC breccia	chip	19
		7		C1MT94	#25	OC	chip	30
			19.3	C1MT113	#27	ureilite	chip	30
			3.5	C1MT95	#7	ureilite	chip	30
mix 5	41.9			C1MT319B, BKR1MT319B	#91A	CC breccia	125-500 μm powder	19
	37.1			C1MT319A, BKR1MT319A	#91A	CC breccia	<125 μm powder	30
			21	C1MT113B, BKR1MT319B	#27	ureilite	125-500 μm powder	30